13203

92-0287
CR27-92

Development of Methods for Modelling Structural Response and Predicting Failure of Structures Subjected to Blast Loading - Phase V

(Final Report for Contract No. W7702-1-R234/01-XSG)

by

[illegible]
[illegible]
22-[illegible]
2145

M.D. Olson

Department of Civil Engineering
University of British Columbia
Vancouver, B.C., Canada

859

December 1991

TABLE OF CONTENTS

Page

1. INTRODUCTION 4

2. WORK PROGRESS 4

   2.1. Extension of FENTAB, NFSACSS and NAPSSE for non-zero boundary displacement 4

   2.2. Progress in extending the failure criteria for isotropic materials 5

   2.3. Design of experiments for verification of failure modelling 6

   2.4. Development of procedures for iso-response curve construction for selected programs 6

   2.5. Progress on the extension of NAPSSE for box structures 7

   2.6. Implementation of time step control in various programs 8

   2.7. Report on feasibility for extension of super-elements to curved shells 9

   2.8. Report on the extension of the rigid-plastic method to box structures 9

   2.9. Report on the feasibility of extending super-elements for both global and detailed modelling 10

3. DELIVERABLES 10

4. REFERENCES 10

APPENDICES

   I. Contract Work Statement

   II. Failure Prediction of Blast Loaded Ductile Beams using Approximate Deflection Profiles by J.R. Fagnan.

III. Progress in Developing a Procedure for Constructing Iso-response Curves for Selected Programs by J. Jiang and M.D. Olson.

IV. Nonlinear Static and Dynamic Analysis of Stiffened Box Structures using Super Elements by J. Jiang and M.D. Olson.

V. Documentation for the program NASBSSE - Nonlinear Analysis of Stiffened Box Structures using Super Elements by J. Jiang and M.D. Olson.

VI. User's Manual for RIPTASP - Rigid-Plastic Transient Analysis of Beams, Grillages and Stiffened Plates by R.B. Schubak and M.D. Olson.

1. INTRODUCTION

The work statement specifications for the present contract are attached as Appendix I. The performance period for the contract was April 1/91 to October 31/91.

During the time of this contract one Ph.D. graduate student and one full time research associate have been working on the contract research topics. These were respectively, Mr. Julien Fagnan and Dr. Jianping Jiang. Mr. Fagnan was partially supported by the contract through a standard graduate research assistantship, whereas Dr. Jiang's salary was funded entirely by the contract.

All the topics listed in the work statement (Appendix I) have been considered. The progress made on these topics is outlined briefly in the following. Full details have been provided in the Appendices.

2. WORK PROGRESS

Much of the work discussed in the following is a continuation of that of the previous contract as reported in Ref. 1.

2.1. Extension of FENTAB, NFSACSS and NAPSSE for non-zero boundary displacement

The preliminary planning for this topic has been carried out but due to lack of time and resources the actual task has not been completed. Modifications to FENTAB (Ref. 2) to include support motions have been made in connection with the failure analysis development as discussed in Section 2.2.

2.2. Progress in extending the failure criteria for isotropic materials

Mr. Julien Fagnan is carrying out the work on this project as part of his Ph.D. thesis research. He first considered dynamically loaded beams, since suitable experimental results were available in the literature for comparison. The experimental observations showed that for ductile materials such as steel or aluminium, failure could be classified into three types or modes:

I - large deformations rendering the structure unserviceable
II - tensile tearing failure, generally at a support
III - shear failure

Mode I is already included in all our nonlinear elastic-plastic or rigid-plastic programs. Mr. Fagnan has formulated an analytical model to predict modes II and III in beam problems. The model uses the computed results from FENTAB (Ref. 2) as input to the analytical model to calculate maximum tensile strains and shear stresses at the boundaries. The program then tells the user that the beam structure has failed when these values exceed the user specified tolerance values of rupture strain or ultimate shear stress, whichever occurs first. This work has been documented in preliminary draft form and is attached as Appendix II.

The FENTAB program has been modified to include this analysis for beams with general loading and general boundary conditions including elastically restrained ones. However at this time, not all these changes have been fully tested and hence the modified program has not been forwarded to DRES. Some modifications have also been made to the rigid-plastic program RIPTASP (Ref. 3) to include this failure analysis but again these have not been fully tested.

The next phase of the work to extend the theory for the one-dimensional models to two-dimensions for incorporation into programs such as NFSACSS (Ref.4) and NAPSSE (Ref. 5) is currently underway.

2.3. Design of experiments for verification of failure modelling

This design work is only now being addressed as part of the current work on the extension of the failure criterion to two-dimensions, as discussed in Section 2.2.

2.4. Development of procedures for iso-response curve construction for selected programs

The concept of iso-response analysis is one in which the response of a structure to pressure pulses of a specific shape is conveniently represented by a set of iso-response curves. Each of these curves is essentially a plot of the peak pressure versus total impulse that produce the same magnitude of certain control damage parameters. The objective of this work was to explore the possibility of implementing this concept and, if possible, to develop a numerical procedure for efficiently constructing iso-response curves for some selected programs. A report of the progress made to date on this subject has been prepared and is attached as Appendix III. A brief summary of it is given in the following.

The first program selected for implementation of this analysis was the rigid plastic stiffened plate program, RIPTASP (Ref. 3). For this program, an appropriate control damage parameter is the permanent midspan displacement W_f. The bisection search technique was adopted here to construct the iso-response curves. Modification of the program RIPTASP to accommodate the iso-response analysis as an additional option has been finished. In terms of optimal programming, care has been taken to ensure that no change to the input file specifications is required. That is, all the additional input data required for running this new version are read in directly from the keyboard rather than from a file. The user just simply follows the instructions prompted on the console screen. By this way, the same input file can be used to perform time history or iso-response analysis, depending on the users choice.

To develop a similar procedure for other models such as the finite strip and finite element programs will be possible but is not a trivial task. Firstly, the choice of an appropriate damage parameter for these programs requires some substantial research because the permanent displacement is no longer a direct output of these programs. That is, the transient response usually exhibits a peak displacement followed by a continuous elastic oscillation about some permanent displacement. Secondly, from previous computational experience with these programs, it is expected that the computing cost for using these programs to perform iso-response calculations will be too high to be practical. For this reason, this work has not been pursued any further for the time being.

2.5. Progress on the extension of NAPSSE for box structures

Dr. Jiang spent the past several months working on the extension of the super element stiffened plate analysis to rectangular box structures. The work of developing this analysis and testing it on many static and dynamic examples is now finished (Ref. 6). The details are included in Appendix IV. A brief summary of the work follows.

The objective of this work was to extend the applicability of the super plate elements to more complex and larger structures such as stiffened box structures. The new developments made through the course of this work include modification of the displacement functions for both plate and beam elements to provide complete C^1 continuity and compatibility on the interface between the various elements and the introduction of suitable transformations to correctly model folded plate and stiffened box structures. The new formulation has been applied to the static, vibration and transient analysis of various structures such as flat plates, folded plates and rectangular boxes. Both isotropic and beam stiffened structures were considered and the results obtained were compared with experimental results or other available solutions. In general, the numerical results obtained indicate that the new super element formulation can provide reasonable solutions for both linear and nonlinear problems of stiffened box structures.

The computer program with all the various analysis options has been organised into one package called NASBSSE, and the documentation for it has now been completed (Ref. 7). The details are included in Appendix V.

Several tasks listed in the work statement under item (5) have not been included due to lack of time and resources. These include automatic time stepping, interfacing NAPSSE with the code BRT, and preparation of pre- and post-processors. The addition of a failure criterion is part of ongoing work as discussed in Sec. 2.2.

2.6. Implementation of time step control in various programs.

The contract work statement (Appendix I) called for modifications to the beam bending program FENTAB (Ref. 2), the finite strip cylindrical shell program NFSACSS (Ref. 4) and the super element stiffened plate program NAPSSE (Ref. 5) to add user ports for time step variation during the solution phase. These modifications have now been completed for NFSACSS, NAPSSE as well as NASBSSE but not yet for FENTAB.

It would be advantageous to have these time step changes made automatically within the program according to some accuracy criterion. Unfortunately this is quite difficult to accomplish for general analyses which may at some time be mainly elastic while at others may involve large plastic deformation. It is anticipated that the option will be developed as part of future contract work. The present option in these programs requires the user to specify the number of time steps to be performed for each specified time step size.

2.7. Report on feasibility of extension of super elements to curved shells

A study to determine the feasibility of extending the super element stiffened plate analysis to curved shells has been carried out. It was determined that an extension to cylindrical shells would be quite easy. The experience gained in the extension of the finite strip analysis from plates to cylindrical shells (Ref. 1) indicated that the super element for plates could easily be extended to cylindrical shells. However it was also determined that the extension of the straight plate stiffener to a curved one for the cylindrical shell would be more complicated. Hence it was decided to proceed with the extension to cylindrical shells and to test the efficiency of the analysis before pursuing the extension to doubly curved shells. Dr. Jiang has now begun this development work.

2.8. Report on the extension of the rigid-plastic method to box structures

The development work for the rigid-plastic analysis of orthogonally stiffened plates was completed by Dr. R. Schubak during the time of the previous contract (Ref. 1). In this approach the stiffened plate is modelled as an orthogonal grillage of asymmetrical beams. A rigid-plastic analysis of this grillage was formulated via an assumed mode mechanism with travelling hinges and an energy analysis. The analysis proceeds in a time stepping manner and at each time step, the hinge locations are determined by Lee's functional minimization. A PC program called RIPTASP has been coded to carry out this analysis. This program includes in an approximate manner the effects due to end slippage and strain rate sensitivity. The documentation for this program has now been completed (Ref. 3) and is included as Appendix VI.

The extension of this rigid-plastic analysis to box structures has not been carried any further due to lack of time and resources.

2.9. Report on the feasibility of extending super-elements for both global and detailed modelling

There is no progress to report on this project again due to lack of time and resources.

3. DELIVERABLES

Several computer programs and their corresponding documentation manuals have been completed during the time of this contract. A list of these programs is given below along with the documentation references. The documentation manuals have also been included herein in the appendices. All these programs and documentation manuals are considered to be deliverables under the terms of the contract.

Computer programs transmitted to DRES

i) RIPTASP - Rigid-Plastic Transient Analysis of Beams, Grillages and Stiffened Plates, (Ref. 3)

ii) NASBSSE - Nonlinear Analysis of Stiffened Box Structures using Super Elements, (Ref. 7)

4. REFERENCES

1. M.D. Olson, "Development of Methods for Modelling Structural Response and Predicting Failure of Structures to Blast Loading-Phase IV", Final Report for Contract No. 01SG. W7702-8-R038, Department of Civil Engineering, University of British Columbia, Vancouver, B.C., June 1991.

2. J. Jiang and M.D. Olson, "Documentation for the Program FENTAB-Finite Element Nonlinear Transient Analysis of Beams, Version 2.0, Dept of Civil Engineering, U.B.C., Vancouver, B.C., August 1990.

3. R.B. Schubak and M.D. Olson, "User's Manual for RIPTASP - Rigid Plastic Transient Analysis of Beams, Grillages and Stiffened Plates", Dept of Civil Engineering, U.B.C., Vancouver, B.C., June 1991.

4. J. Jiang and M.D. Olson, "Documentation for the Program NFSACSS - Nonlinear Finite Strip Analysis of Cylindrical Shell Structures", Dept of Civil Engineering, University of B.C., Vancouver, June 1990.

5. J. Jiang and M.D. Olson, "Documentation for the Program NAPSSE - Nonlinear Analysis of Plate Structures Using Super Elements", Dept of Civil Engineering, U.B.C., Vancouver, B.C., December 1990.

6. J.Jiang and M.D. Olson, "Nonlinear Static and Dynamic Analysis of Stiffened Box Structures Using Super Elements", Dept of Civil Engineering, Structural Res. Series Report No. 36, U.B.C., Vancouver, B.C., June 1991.

7. J. Jiang and M.D. Olson, "Documentation for the Program NASBSSE - Nonlinear Analysis of Stiffened Box Structures using Super Elements", Dept of Civil Engineering, U.B.C., Vancouver, B.C., June 1991.

Appendix I

Contract Work Statement

The work will consist of the following extensions to the work completed in previous contracts:

1. **Update the program FENTAB, NFSACSS and NAPSSE to allow boundary stiffness coefficients and non-zero boundary displacements to be specified by the user.**
2. **Continue the development of a failure criterion for isotropic materials (see Phase I, Item 2 in Ref.7). Extend the programs RIPTASP, NFSACSS and NAPSSE to include the prediction of failure. This will require numerical testing of the extended programs and comparison of predictions with experimental results.**
3. **Design experiments on simple panels for verification of the above failure modelling.**
4. **Develop a procedure for efficiently constructing an iso-response curve for selected programs.**
5. **Continue the development of the program NAPSSE for box structures based on the super element (see Phase III, Item 6 in Ref.7). This will include:**
   - **Automatic time stepping.**
   - **Addition of a failure criterion.**
   - **Interfacing NAPSSE with the code BRT.**
   - **Preparation of a pre-processor and post-processor. The pre-processor should include a mesh generator for complete box structures and subsets.**
   - **Numerical testing and comparison of displacements, accelerations and strains with experimental data where possible.**
6. **Add a user port for time step variation during the solution phase for the computer programs FENTAB, NFSACSS and NAPSSE.**
7. **Continue the feasibility study begun under Item 7 of Phase III in Ref.7 to update the code NAPSSE to model both singly and doubly curved shells. This extension may be based on shallow shell theory. However, an investigation should be carried out to determine the feasibility of extending the approach to deep shells.**

Note: This extension combined with the extension to box structures (Item 5 above) should allow many possible configurations to be considered. Plates, one- and two-way stiffened panels, and various re-entrant corner configurations can be considered as subsets of the general box structure. By appropriate choice of curvature for the sides, both open and closed ended cylinders (optionally stiffened axially and/or circumferentially) and stiffened or unstiffened spheres should be considered special cases.

8. Investigate the feasibility of extending RIPTAB for intersection of one-way stiffened panels and RIPTASP for 3D box structures composed of intersecting one- and two-way stiffened panels.

9. Investigate the feasibility of modifying the interpolation functions within super finite elements (SFE) to obtain interpolations suitable for either global or local modelling.

   For example, it may be possible to convert a SFE to a finite strip or a standard finite element by a direct modification of the interpolation functions. The development of transition elements will be required in order to provide compatible interpolations along element boundaries. This capability would thus allow connection of super elements with finite strips or standard finite elements so that local areas may be modelled accurately.

Appendix II

FAILURE PREDICTION OF BLAST LOADED DUCTILE BEAMS USING APPROXIMATE DEFLECTION PROFILES

J.R.FAGNAN

September 18, 1990

Abstract

Approximate models are developed to predict the Mode II or III failure of blast loaded beams. These models are incorporated into a finite element program (FENTAB) which then allows results to be obtained for a full range of blast intensities and the prediction of the failure mode. Comparison of the results of the program with the experimental tests of Menkes and Opat[3] on aluminum 6061 T6 beams yields encouraging results.

1 Introduction

Extensive work has been done on the modelling of the response of structures subjected to large dynamic loads. Various methods have extended this analysis into the range where large permanent deformations occur. In particular, Folz[1,2] has developed a finite element program called FENTAB (Finite Element Nonlinear Transient Analysis of Beams) which can numerically simulate the transient response of slender ductile beams with geometric and/or material nonlinearities. Virtually no work has included failure or rupture predictions.

Menkes and Opat[3] conducted a series of experiments on clamped aluminum 6061 T6 beams subjected to large dynamic loads. These loads where applied by using sheet explosives attached to the beams with neoprene buffers. As the intensity of the impulse was increased three distinct modes of failure were identified.

Mode I: Large inelastic deformation.

Mode II: Tearing (tensile failure) in outer fibres, at or over the support.

Mode III: Transverse shear failure at the support.

Jones[4,5] introduced simple rigid-plastic models to predict the failure thresholds for Mode II and Mode III response. FENTAB already has the capability of predicting Mode I response. The purpose of this paper is to develop a solution procedure similar to Jones' which can be added to the FENTAB program to enable it to predict Mode II and Mode III response. This updated program would then be able to provide solutions to beam problems subjected to the full range of load intensities and predict the failure mode.

2 Formulation of Failure Criteria

The assumptions used to derive the failure criteria developed in this study are consistant with those used to derive the FENTAB program. This program used the strain displacement relationship for a Euler-Bernouilli beam, undergoing large deformations. The lateral deflection is large relative to the beam depth but still small in comparison to the beam length. The following assumptions are made[1]:

1. In the undeformed configuration the centroidal axis of the beam is straight and coincident with the x-axis. Furthermore, (x–z) is a plane of symmetry for the beam cross-section and the applied loads.
2. The Bernouilli-Euler Hypothesis is valid. That is, normal sections remain plane, undistorted, and normal to the axis of the beam in its deformed configuration.
3. The Green strain measure is everywhere small, i.e. $|\epsilon_{ij}| \ll 1$ Also, the midsurface strain and the square of the slope of the beam axis are small, i.e. $|\partial u/\partial x| \ll 1$ and $(\partial w/\partial x)^2 \ll 1$.
4. The beam is slender so that terms of order h^2 can be neglected in the strain-displacement relationship, (h is a parameter representative of the cross-sectional depth of the beam).

2.1 Mode II Failure Criteria

The estimate of the Mode II threshold herein is based on the approach taken by Jones[4]. Jones has attempted to predict Mode II failure using rigid plastic theory. The model consists of plastic hinges at the supports and at midspan joined by rigid links. In the present application the model consists of plastic hinges at the supports only, while the beam is modelled by FENTAB which takes into account geometric and material non-linearities. Approximations are then made to the deflected shape to calculate the maximum total strain at the supports.

The maximum total strain (ϵ_m) at the supports of a fully clamped beam is expressed as

$$\epsilon_m = \epsilon_a + \epsilon_b \tag{1}$$

where ϵ_a is the axial strain at the neutral axis and ϵ_b is the bending strain at the support.

2.1.1 Bending Strain

The bending strain of a slender beam may be expressed as

$$\epsilon_b = h\kappa/2 \tag{2}$$

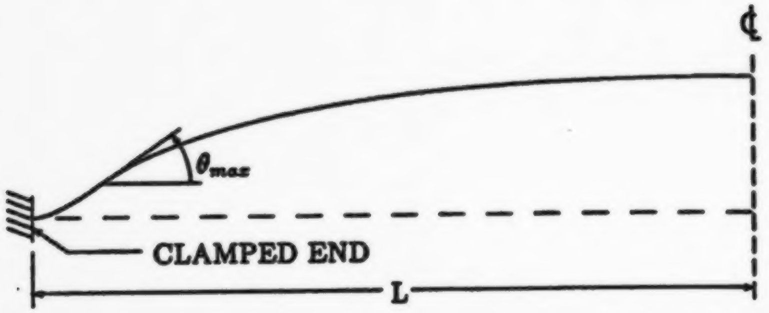

Figure 1: Typical Deflection Profile as Determined by FENTAB

where h is the beam depth and κ is the curvature of the plastic hinge. The curvature κ is defined as

$$\kappa = \theta/\ell \tag{3}$$

where θ is the rotation of the plastic hinge and ℓ is the plastic hinge length.

The typical deformed profile of a beam with clamped ends subjected to a lateral load as determined by FENTAB is shown in fiqure 1. The program is not able to model a plastic hinge at the support. An approximate mode shape was therefore used to determine the bending strain. The rotation of the plastic hinge was assumed to be equal to the maximum rotation of the beam as shown in Figure 1. This maximum rotation usually occurs a short distance from the clamped end.

Two methods were used to evaluate the maximum rotation of the beam. The generalized nodal coordinates for a given finite element as developed in FENTAB is given by

$$\mathbf{d}_e = \lfloor u_1, w_1, \frac{\partial w_1}{\partial \eta}, u_2, w_2, \frac{\partial w_2}{\partial \eta} \rfloor^T \tag{4}$$

As shown in Figure 2. The first method simply examined all the finite element nodes and selected the maximum rotation $\partial w/\partial \eta$ occuring along the length of the beam.

The second method interpolated along the length of each finite element using the shape functions of the finite element program. The lateral displacement w may be expressed in terms of the generalized nodal coordinates and the shape functions as

$$w = \lfloor 0, N_3, N_4, 0, N_5, N_6 \rfloor \, \mathbf{d}_e, \tag{5}$$

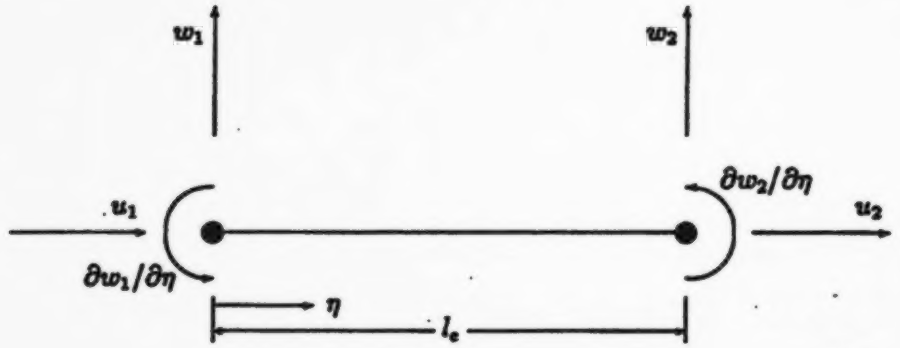

Figure 2: Generalized Degrees of Freedom

where the shape functions $N_{i=3,4,5,6}$ are given by

$$N_3 = 1 - 3\left(\frac{\eta}{l_e}\right)^2 + 2\left(\frac{\eta}{l_e}\right)^3 \tag{6}$$

$$N_4 = \eta\left[1 - 2\left(\frac{\eta}{l_e}\right) + \left(\frac{\eta}{l_e}\right)^2\right] \tag{7}$$

$$N_5 = 3\left(\frac{\eta}{l_e}\right)^2 - 2\left(\frac{\eta}{l_e}\right)^3 \tag{8}$$

$$N_6 = \eta\left[-\left(\frac{\eta}{l_e}\right) + \left(\frac{\eta}{l_e}\right)^2\right], \tag{9}$$

with η representing the local axial coordinate and l_e representing the undeformed length of the element.

The first derivative of w represents the slope or rotation of the beam. Taking the second derivative of w, setting it equal to zero and solving for η gives

$$\eta\,\bigg|_{\theta_{max}} = \frac{3w_1 + 2\theta_1 l_e - 3w_2 + \theta_2 l_e}{6w_1 + 3\theta_1 l_e - 6w_2 + 3\theta_2 l_e} \tag{10}$$

where $\theta_1 = \partial w_1/\partial\eta$ and $\theta_2 = \partial w_2/\partial\eta$. Substituting this value of η into the equation for the first derivative of w provides the maximum rotation in that

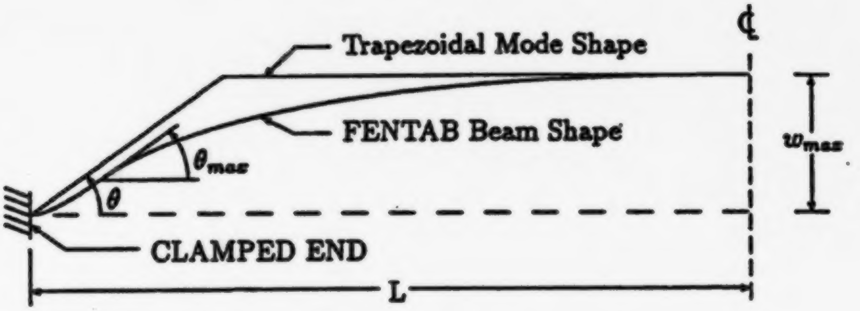

Figure 3: Trapezoidal Mode Shape

element. Each element is examined to determine the maximum rotation in the beam.

An approximation for the hinge length ℓ was also made because of the finite element program's inability to model a plastic hinge. The hinge length was assumed to be a function of the beam depth h given by

$$\ell = \alpha h \tag{11}$$

where the value of α is input by the user. Based on a study by Nonaka[] on the hinge length of rigid plastic beams of rectangular cross-section, a value of $\alpha = 2$ is recommended. This assumes that the elastic response of the beam is negligible compared to the plastic response. Equation 2 now gives the bending strain as

$$\epsilon_b = \theta / 2\alpha \tag{12}$$

2.1.2 Axial Strain

Two methods were also considered to evaluate the axial strain. The first consisted simply of approximating the deflected shape of the beam by a trapezoidal mode. The shape of the trapezoid was established as shown in Figure 3. The height of the trapeziod was set equal to the maximum deflection of the beam and the angle θ was set equal to the maximum rotation θ_{max} as determined for the bending strain. By calculating the length of this assumed shape the axial strain can be calculated. The length is expressed as

$$2L' = 2\left[\frac{w_{max}}{\sin\theta} + \left(L - \frac{w_{max}}{\tan\theta}\right)\right] \tag{13}$$

and the axial strain is therefore

$$\epsilon_a = \frac{w_{max}}{L \sin\theta}(1 - \cos\theta) \tag{14}$$

The second method used to evaluate the axial strain was to integrate directly the deformed profile of the beam as determined by FENTAB. The arc length of the deformed shape is given by

$$L' = \int_0^L \sqrt{1 + [w'(x)]^2} dx \tag{15}$$

From assumption 3 above this is rewritten as

$$L' = L + \frac{1}{2}\int_0^L (w')^2 \, dx \tag{16}$$

and the axial strain is therefore

$$\epsilon_a = \frac{1}{2L}\int_0^L (w')^2 \, dx \tag{17}$$

The lateral deflection w has been expressed in equation(5) in terms of the shape functions. By substituting equation(5) into equation(17) the axial strain for an element may be expressed as

$$\epsilon_{a_e} = \frac{1}{2l_e}\int_0^{l_e} \mathbf{d}_e^T \mathbf{B}_2^T \mathbf{B}_2 \mathbf{d}_e \, dx \tag{18}$$

where,

$$\mathbf{B}_2 \equiv \lfloor 0, \frac{\partial N_3}{\partial \eta}, \frac{\partial N_4}{\partial \eta}, 0, \frac{\partial N_5}{\partial \eta}, \frac{\partial N_6}{\partial \eta} \rfloor \tag{19}$$

By using Guass integration over each element and summing over all the elements, the axial strain is determined.

The total strain as determined by equation(1) is then compared to a strain criteria for failure. This user supplied value for the rupture strain depends on the material being modelled.

2.2 Mode III Failure Criteria

The FENTAB program as developed by Folz[2] is based on Euler-Bernouilli theory. This theory is inadequate for the analyis of shear stress as a result of impact conditions, because it yields the nonphysical result that waves of infinitesimal wavelength (and therefore discontinuities) propogate with infinte velocity.[7] In addition, the philosophy of this research has been to develop simple approximate numerical and analytical tools to provide good engineering accuracy for design.

A simple analytical method is therefore developed to determine the shear stress at the support at each time step. The vertical forces, including inertial forces, are summed at each time step to determine the end reactions of the beam. Taking advantage of the symmetry of the problem only one half of the beam is considered. Summing the forces in the vertical direction gives

$$R + \int_0^L q \, dx - \int_0^L ma \, dx = 0 \tag{20}$$

where R is the end reaction, q is the external load, m is the mass of the beam and a is the acceleration of the beam. In the FENTAB program a lumped mass matrix is used, therefore q, m and a were evaluated for each node and summed over the beam length giving

$$R + \sum_{nodes} q_i - \sum_{nodes} m_i a_i = 0 \tag{21}$$

The maximum shear stress in a rectangular beam is $\tau_{max} = 1.5R/A$ where A is the cross-sectional area of the beam. As the central fibres yield, the stress distribution becomes more uniform. It is assumed that shear failure does not occur until all the fibres in the cross-section reach the ultimate shear stress. The shear stress is therefore treated as uniform across the depth with $\tau = R/A$ and compared to a maximum ultimate shear stress to determine if Mode III failure has occured.. This simple procedure was also used by Ratzlaff and Kennedy.[8]

3 Experiment

The experiment by Menkes and Opat[3] consisted of a series of 6061 T6 clamped aluminum beams subjected to a surface explosive charge. The charge was provided by sheet explosive which is cemented to a neoprene buffer which is bonded to the top surface of the beams. The configuration is shown schematically in Figure 4. The beam specimens had three thicknesses

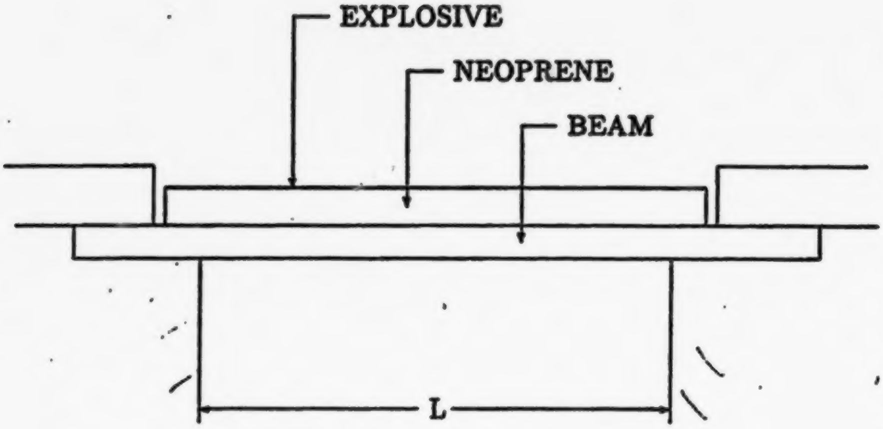

Figure 4: Schematic Drawing of Experimental Setup

(0.187″, 0.250″, and 0.375″) and two lengths (4.0″ and 8.0″) and where all 1.0″ wide. The intensity of the impulse was varied by using different thicknesses of sheet eplosive.

As the impulse was increased the response of the aluminum beams passed through the three failure modes. For Mode I failure, the maximum permanent deformation was measured. As the response passed into Mode II and III failures, the permanent deformation of the severed beam was no longer measured quantitatively. A set of photographs of one series of beams (0.250″ x 1.0″ x 8.0″) does show qualitatively the variation of deformation with impulse. As the impulse intensity was increased, the permanent deformation of the severed central section appears to be reduced.

Menkes and Opat point out that the selection of the thresholds for Modes II and III are highly subjective. The threshold for Mode II is taken as the impulse intensity which first causes tearing at the supports. The threshold intensity for Mode III is taken as the impulse intensity which first causes no significant deformation of the severed central section. Between these two thresholds, failure mechanisms overlap and some of the beams exhibited failures which involve both the tearing and shearing modes.

Unfortunately the paper by Menkes and Opat does not contain a detailed

DEPTH	LENGTH	FENTAB				MENKES AND OPAT
		$\alpha = 2$		$\alpha = 5$		
		TRAP.	INT.	TRAP.	INT.	
0.375″	8.0″	33.4	33.4	42.9	46.0	46.0
	4.0″	39.6	39.6	46.0	50.7	46.0
0.250″	8.0″	25.6	25.6	28.7	28.7	28.7
	4.0″	25.6	25.6	28.7	28.7	33.4
0.187″	8.0″	17.8	17.8	25.6	25.6	28.7
	4.0″	17.8	17.8	25.6	25.6	28.7

Table 1: Comparison of Mode II Threshold Impulses(ktaps)

description of the experimental configuration and the method used to clamp the beam ends. The schematic drawing of Figure 4 is the only resource at our disposal. It shows the clamps on the top surface of the beam to be set back from those on the bottom surface. If this was indeed the case then the beam ends at A and B would not be fully restrained against rotation and horizontal translation. Possible consequences of this will be dicussed in the following section.

4 Comparison With Experimental Results

The modified FENTAB program as described was used to simulate the experiment conducted by Menkes and Opat.[3] The beam was modelled with 10 equal length elements to represent, using symmetry, half the span of the beam. The blast load was modelled by a rectangular pressure pulse with the same impulse as the experimental test, because the pressure-time history of the explosive charge was not known. A parameter study was done to determine the optimum duration of the pressure pulse and a time of 60 μsec was chosen and used for all the FENTAB runs. Further information is required to determine if this modelling was valid.

A value for the maximum allowable strain at the support must be chosen in order to predict the Mode II failure threshold. A value of 0.17 was used in this analysis, which corresponds to the static uniaxial rupture strain for 6061 T6 aluminum.[9] Aluminum is considered to be a strain rate insensitive material and in the absence of adequate information this value was adopted for the dynamic rupture strain.

In order to predict the Mode III threshold an estimate of the maximum ultimate shear stress is required. A value may be obtained by considering an extension of the von Mises yield criterion to ultimate strength conditions[8], $\tau_u = \sigma_u/\sqrt{3}$. For 6061 T6 aluminum, σ_u = 45,100 psi.[9], and therefore τ_u = 26,000 psi. Popov[10] suggests a value of τ_u = 30,000 psi. In addition, Menkes and Opat[3] note that the dynamic shear strength appears to be much higher than the static shear strength. The results of this analysis are based on a value of τ_u = 30,000 psi.

The beam material was modelled as rigid plastic with no strain hardening. The properties of the 6061 T6 aluminum used by Menkes and Opat as quoted by Jones[4] are ρ= 2.56 x 10^{-4} lb s^2/in.^{4} and σ_0= 41,600 psi., and from Jones et. al.[9] E = 10.5 x 10^6 psi.

The results from the two methods used to calculate θ_{max} for the bending strain (element end rotation and element interpolation) were virtually identical. The shape functions used in FENTAB were C^1 continous. Thus, although the displacement and the rotation at the end of each element at a node were continuous, the curvature was discontinous. Therefore the maximum rotation of each element generally occured at the nodes.

Table 1 summarizes the Mode II thresholds as predicted by FENTAB. Results are presented for both the trapezoidal and direct integration failure models for the membrane strain. The results for $\alpha = 2$ provide a conservative estimate of the threshold. An arbitrary value of $\alpha = 5$ was also examined. These results were also generally conservative in estimating the threshold but much closer to the experimental results. A possible explanation for this result is that the beam ends were not fully clamped. By examining the schematic drawing it is evident that the beam may have rotated at points A and B. This would have the effect of lengthening the hinge and reducing the bending strain. This would have delayed the Mode II threshold. Further testing must be done to determine the appropriate value for the hinge length.

The Mode III thresholds predicted by FENTAB are summarized in Table 2. These results agree closely with the experimental values, given the value chosen for the ultimate shear strength τ_u of the beam. The choice of α and the membrane strain model (trapezoidal vs. integration) does not directly affect the shear stress calculation. However, delaying the Mode II threshold by chosing a larger α for example, may cause the beam model to fail

DEPTH	LENGTH	FENTAB				MENKES AND OPAT
		$\alpha = 2$		$\alpha = 5$		
		TRAP.	INT.	TRAP.	INT.	
0.375″	8.0″	64.0	64.0	64.0	64.0	66.0
	4.0″	66.0	66.0	66.0	66.0	64.0
0.250″	8.0″	46.0	46.0	46.0	42.9	46.0
	4.0″	50.7	50.7	50.7	50.7	46.0
0.187″	8.0″	39.6	39.6	35.1	35.1	42.9
	4.0″	39.6	39.6	39.6	35.1	42.9

Table 2: Comparison of Mode III Threshold Impulses(ktaps)

in shear prior to failing in tension and result in a lower Mode III threshold.

The Mode III threshold was also affected by the modelling of the blast load. The shear stress is a function of the initial velocity, which in turn is a function of the initial pressure. For a given impulse, varying the initial pressure did not significantly affect the Mode I or Mode II results. The Mode III threshold, however, was sensitive to the value chosen for the initial pressure. Further investigation is required into this relationship.

An examination of the shear stress at the support as a function of time is shown for one particular beam in Figure 5. The general trend of the stress is typical for all the beams. The shear stress generally increases during the loading time and then suddenly drops as the load is removed. The stress then generally increases again to its maximum value and remains relatively constant until the maximum deflection is reached, after which the stress decreases. In Figure 5, the beam failed in Mode II prior to Mode III. Failure occurred at 144 μsec for the trapezoidal method and at 172 μsec for the integration method. The prediction of Mode III failure does not occur until 217 μsec. At the next highest impulse of 64.0 ktaps, the peak stress at the end of the loading phase exceeds the maximum shear stress of 30,000 psi and Mode III failure occurs prior to Mode II failure at a time of 58 μsec. Mode III failure generally occurs during the loading phase.

As the impulse was increased from Mode II to Mode III Menkes and Opat noted that the deformation of the severed central section was reduced. Figure 6 shows the predicted failure profile of the 0.375" x 8.0" beam at several

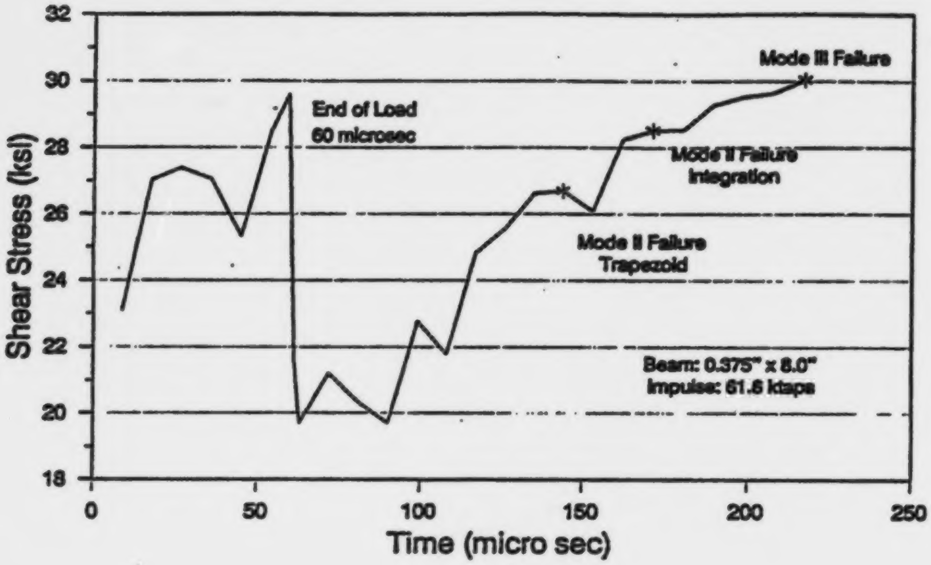

Figure 5: Typical Shear Stress History at Support

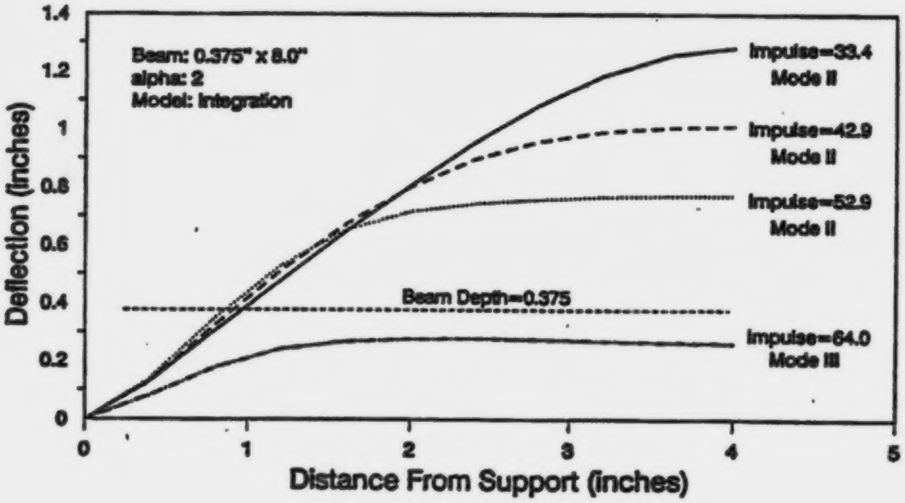

Figure 6: Beam Profiles at Failure

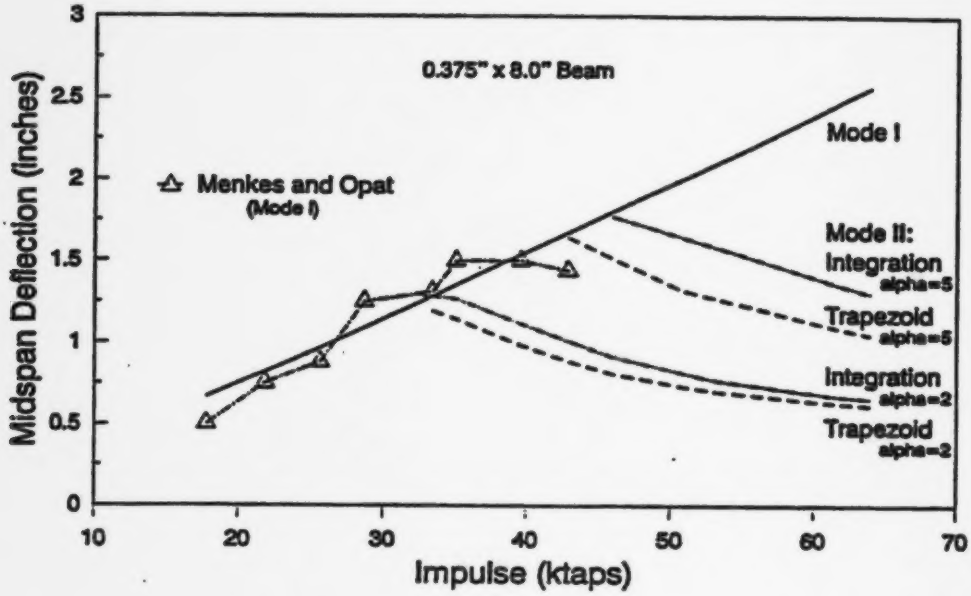

Figure 7: Comparison of FENTAB with Menkes and Opat Results

impulses. The trend of the results agree with the experimental observations as noted. Menkes and Opat characterize a pure shear failure as one with no significant distortion in the severed central section. Figure 6 shows that the deformation of the beam at the Mode III threshold is less than the beam depth, and therefore no significant distortion has taken place.

Teeling-Smith and Nurick[11] performed an investigation into the failure of circular plates subjected to blast loading. They produced a graph of dimensionless deflection versus dimensionless impulse which included measurements of the deflection of the severed plates. The graph had an upward slope for Mode I deflections until the Mode II threshold was reached. Then the graph had a downward slope until the Mode III threshold was reached and the deformations were small. Figure 7 shows the deflection versus impulse for the 0.375" x 8.0" beam. The solid line shows the Mode I results and the dashed lines show the various Mode II responses. This graph has the same trend as the Teeling-Smith and Nurick graph.

5 Conclusions

5.1 Summary

The objective of this investigation was to determine if a simple failure model could be incorporated into the FENTAB finite element program to predict the onset of Mode II failure. This appears to have been successfully accomplished. Further investigation is needed to determine if the modelling of the hinge length and bending strain is adequate.

A prediction of the Mode III threshold was also incorporated into the program. Although a very simple procedure was used, the prediction was very close to the experimental results.

5.2 Areas Requiring Further Investigation

In the course of this study several areas were identified as requiring further investigation. Several of these are listed here to point out possible refinements to the procedure as well as potential sources of error when modelling different problems.

One of the basic assumptions on which the FENTAB program is based is that the square of the slope of the beam axis is small., i.e.$(\partial w/\partial x)^2 \ll 1$. As the Mode III threshold is approached the maximum rotation of the beam in some cases approaches 0.60 radians. This translates to a square of the slope of the order of 0.30 which is no longer much smaller than 1.

Another assumption which FENTAB makes is to neglect the effect of shear deformation and rotatory inertia. Shear deformation may be important in the plastic hinge region at large rotations. Rotatory inertia may also become significant.

No interaction was considered between the Mode II and III failures. Menkes and Opat[3] note that there is some overlap of Mode II and III failures between the threshold values. A shear-moment interaction relationship may help model this phenomenon.

The value choosen for the dynamic rupture strain is not well defined. Limited tests suggests that the rupture strain for aluminum alloys is not influenced by strain rates up to 830 sec^{-1}. In general however the dynamic rupture strain may be higher or lower than the corresponding static value.[12]

These results will be extended to two dimensional problems such as those tested by Teeling-Smith and Nurick, and to problems involving stiffened plates. This will require knowledge of the biaxial values of the material properties discussed in this paper.

References

[1] Folz, B.R., *Numerical Simulation of the Non-Linear Transient Response of Slender Beams.* M.A.Sc. thesis, University of British Columbia, Vancouver, Canada, April 1986.

[2] Jiang, J., and Olson, M.D., *FENTAB*, Department of Civil Engineering, University of British Columbia, Vancouver, 1990.

[3] Menkes, S.B. and Opat, H.J., "Broken Beams", *Experimental Mechanics*, Vol. 13, 1973, pp. 480-486.

[4] Jones, N., "Plastic Failure of Ductile Beams Loaded Dynamically." *Journal of Engineering for Industry*, Vol. 98, 1976, pp.131-136.

[5] Jones, N., "On the Dynamic Inelastic Failure of Beams", *Structural Failure*, T. Wierzbicki and N. Jones, eds., Wiley, 1989, pp. 133-159.

[6] Nonaka, T., "Some Interaction Effects in a Problem of Plastic Beam Dynamics, Parts 1-3", *Journal of Applied Mechanics*, Vol. 34, 1967, pp. 623-643.

[7] Volterra, E., and Zachmanoglou, E.C., *Dynamics of Vibrations*, Charles E. Merrill, Columbus, OH, 1965, pp. 528-529.

[8] Ratzlaff, K.P., and Kennedy, D.J.L., "Behaviour and Ultimate Strength of Continous Steel Plates Subjected to Uniform Transverse Loads",*CJCE*, Vol. 13, No. 1, 1986, pp. 76-85.

[9] Jones, N., Dumas, J.W., Giannotti, J.G., and Grassit, K.E., "The Dynamic Plastic Behavior of Shells", *Dynamic Response of Strucrures*, G. Herrmann and N. Perrone, eds., Pergamon Press, 1972, pp. 1-29.

[10] Popov, E.P., *Mechanics of Materials*, Prentice-Hall, 1978, pp.

[11] Teeling-Smith, R.G. and Nurick, G.N., "The Deformation and Tearing of Thin Circular Plates Subjected to Impulsive Loads", *International Journal of Impact Engineering*,

[12] Jones, N., "Some Comments on the Modelling of Material Properties for Dynamic Structural Plasticity", *Int. Conf. Mech. Prop. Materials at High Rates of Strain*, Oxford, 1989, pp. 435-445.

Appendix III

PROGRESS IN DEVELOPING A PROCEDURE FOR CONSTRUCTING ISO-RESPONSE CURVES FOR SELECTED PROGRAMS

by

J. Jiang and M.D. Olson

Department of Civil Engineering
University of British Columbia
Vancouver, B. C., Canada

October 1991

1 Introduction

The dynamic response of stiffened plates to lateral pressure pulse loading depends on the dimensions, material properties and boundary conditions of the structure, as well as the loading parameters. To predict the response characteristics, various simplified numerical methods have been developed. These include rigid-plastic analysis, and finite strip and finite element formulations. Based on these methods, several design-analysis codes, e.g. RIPTASP, NFSACSS, NAPSSE, etc. have been developed(Refs.1-3). To effectively use these programs for preliminary engineering design purpose, the iso-response analysis as suggested by a number of researchers seems to be a very useful concept. By this concept, the response of a structure to pressure pulses of a specific shape is conveniently represented by a set of iso-response curves. Each of these curves is essentially a plot of the peak pressure versus total impulse that produce the same magnitude of certain control damage parameters. The objective of this work is to explore the possibility of implementing this concept and, if possible, to develop a numerical procedure for efficiently constructing iso-response curves for some selected programs. The following is a brief report of the progress made to date on this subject.

2 Iso-Response Analysis by Rigid-Plastic Modelling (RIPTASP)

This is the first program selected for implementation of the iso-response calculation. For this program, an appropriate control damage parameter is the permanent midspan displacement W_f. Similar to what was used to construct iso-response curves by program RIPTAB(Ref.4), the bisection search technique is adopted here again. Modification of the program RIPTASP(Ref.1) to accommodate the iso-response analysis as an additional option has been finished. In terms of optimal programing, the care has been taken to ensure that no change will be made to the input file specifications. That is, all the additional input data required for running this new version are read in directly from the keyboard rather than from a file. The users just simply follow the instructions prompted on the console screen. By this way, the same input file can be repeatedly used to perform time history or iso-response analysis, depending on the users choice. It is also noted that for the option of iso-response analysis the input values for peak pressure p_m and duration of loading t_p now implicitly constitutes the searching domain within which a set of iso-response curves will be constructed.

The new version has now been successfully tested on a number of examples including DRES and DRES1B panels, as well as a two-way stiffened square plate. The results obtained are discussed below. In these examples, the effect of pulse shape on the iso-response curves is investigated and the feasibility of using an *equivalent* rectangular pulse to replace the original shape in the iso-response analysis is also studied. It is shown that this equivalent method works very well for the cases considered. This method, therefore, is of practical value in preliminary design-analysis of blast loaded orthogonally stiffened plate structures.

2.1 DRES panel

2.1.1 Rectangular Pulses

The first example considered here is the DRES panel subjected to rectangular pressure pulses. This example is chosen to verify the program. The dimensions and material properties are the same as that used by R. Schubak in his Ph.D. thesis (Ref.5, p.31). Iso-response curves are plotted in Fig. 1 for three prescribed values of W_f, where the nominal impulse is $I = p_m t_p$. These curves are very similar to those obtained from RIPTAB (Ref.5). As observed by Schubak, in each of these curves, three distinct realms of response are revealed: quasi-static response, impulsive response, and intermediate dynamic response. It is also seen that the spacing of these curves is not linearly dependent on the magnitude of the damage parameter W_f.

To investigate sensitivity of the iso-response curves to the asymmetry parameter λ in linear yield curve approximation, three different values of plate thickness of the DRES panel are considered. The results are presented in Fig. 2. As the thickness reduces from 0.25*in* ($\lambda = 0.538$) to 0.15*in* ($\lambda = 0.374$), the curve is shifted to the lower-left corner. This means that when keeping the same level of peak pressure p_m less impulse I is needed to cause the same amount of damage (W_f) for thinner plates and vice versa. On the other hand, the curve is shifted to the upper-right corner for the thicker plate ($\lambda = 0.6339$ for $h = 0.35in$). As can be seen, the spacing of these curves is also not linearly dependent on the value of λ. This implies that it is impossible to have unified iso-response curves for different plates subjected to the same type of pulses.

2.1.2 Trianguler Pulses

In this example, it is assumed that the DRES panel is subjected to more realistic blast type of pressure pulses, i.e., triangular pulses. Iso-response curves are plotted in Fig. 3 for the DRES panel under triangular pulses as well as their equivalent rectangular pulses. In comparing the earlier results obtained by RIPTAB (Ref.5, p.51), a similar trend is exhibited by the present program RIPTASP. It is clear from Fig. 3 that there are no discernible differences between the responses in the impulsive realm, and only small differences in the dynamic and quasi-static realms. Overall, they compare very well.

2.1.3 HOB #315

To further investigate the applicability of the equivalent pulse method for more complicated pressure distributions, the response of the DRES panel subjected to the HOB #315 pulse is repeated here. Before carrying out the iso-response calculation, a time history analysis is performed. Fig. 4 shows the time histories of midspan displacement due to two pulse representations. Here, to simplify the analysis, a trilinear approximation of the HOB #315 pulse is made (see Ref.5) and its equivalent rectangular pulse is obtained from the trilinear pulse rather than from the original pulse. The two response curves are almost identical and they show that this method can be extended to cases involving more complicated loading histories.

The iso-response curves for the two pulse representations are plotted in Fig. 5. Although these curves do not collapse identically, they are very close to each other. It is seen that the differences increase with the increase of the damage parameter W_f. In veiw of the approximate nature of the rigid-plastic model, these differences are considered to be small and they are indeed within engineering tolerance.

2.2 DRES1B Panel

This two-way stiffened plate has the same overall dimensions and material properties as the DRES panel and is also fully clamped at the boundaries. In addition to the four transverse stiffeners, the DRES1B panel has one centrally located longitudinal stiffener (Ref.5, p.95). The panel is assumed to be subjected to the pressure pulse from the HOB #315 test. Again, a time history analysis is carried out first for two pulse representations and the results obtained are presented in Fig. 6. As can be seen, good agreement is obtained. Next, an iso-response analysis is performed for three prescribed values of damage parameter W_f. The curves obtained using the trilinear pulse represention are compared with those by the equivalent rectangular pulse in Fig. 7. Again, the trend is very similar to that of the DRES panel.

2.3 Square Stiffened Plate

This is a four meters square plate stiffened by three identical and evenly spaced T-beams in both directions (Ref.5, p.101). The boundaries of the structure are fully clamped.

For this example, two simple pulses are considered. That is, the plate is subjected to rectangular and triangular pressure pulses. The iso-response curves for the two pulses are plotted in Fig. 8. Generally speaking, the curves obtained from rectangular pulses are similar to those for triangular pulses. However, the response to rectangular pulses shows non-monotonic decrease of the nominal impulse during transition from impulsive to intermerdiate dynamic response for large values of W_f.

To illustrate the capability of the equivalent pulse method for this fully coulped structure, the iso-response analysis is repeated by modelling the triangular pulse in its equivalent rectangular form. The time histories of mid-span displacement and iso-response curves under the two pulses are compared in Figs. 9 and 10, respectively. It can be seen that they are in very good agreement to each other and it appears that the equivalent method works just as well as for the previous examples.

3 Iso-Response Analysis by other Models (NFSACSS, NAPSSE)

To develop a similar procedure for other models such as the finite strip and finite element programs will be possible but not a trivial task. Firstly, the choice of an appropriate damage parameter for these pograms requires some substantial research because the permanent displacement is no longer a direct output of these programs. That is, the transient response usually exhibits a peak displacement followed by a continuous elastic oscillation about some permanent displacement. Secondly, from previous computational experience with these programs, it is expected that the computing cost for using these programs to perform iso-response calculations will be so high that they are not practical for this type of calculations. Finally, iso-response curves are only useful for initial design of structures at which stage the key concerns are not how accurate the answers are but rather the speed of the solution process. It is from this point of view that the rigid-plastic model is both sufficient and effective.

4 Acknowledgement

This work was supported by the Canadian National Defence Department throught a contract from the Defence Research Establishment Suffield, Alberta, Canada.

5 References

1. R.B. Schubak and M.D. Olson, *A User's Manual for RIPTASP: Rigid-Plastic Transient Analysis of Beams, Grillages and Stiffened Plates*, Version 1.0, Department of Civil Engineering, University of British Columbia, Vancouver, Canada, June 1991.
2. J. Jiang and M.D. Olson, *Documentation for the Program NFSACSS: Nonlinear Finite Strip Analysis of Cylindrical Shell Structures*, Version 1.0, Department of Civil Engineering, University of British Columbia, Vancouver, Canada, October 1990.

3. J. Jiang and M.D. Olson, *Documentation for the Program NAPSSE: Nonlinear Analysis of Plate Structures Using Super Elements*, Version 1.0, Department of Civil Engineering, University of British Columbia, Vancouver, Canada, December 1990.

4. R.B. Schubak, M.D. Olson and D.L. Anderson, *A User's Manual for RIPTAB: Rigid-Plastic Transient Analysis of Beams and One-Way Stiffened Plates*, Version 1.0, Department of Civil Engineering, University of British Columbia, Vancouver, Canada, March 1989.

5. R.B. Schubak, *Nonlinear Rigid-Plastic Analysis of Stiffened Plates Under Blast Loads*, Ph.D. Thesis, Department of Civil Engineering, University of British Columbia, Vancouver, Canada, April 1991.

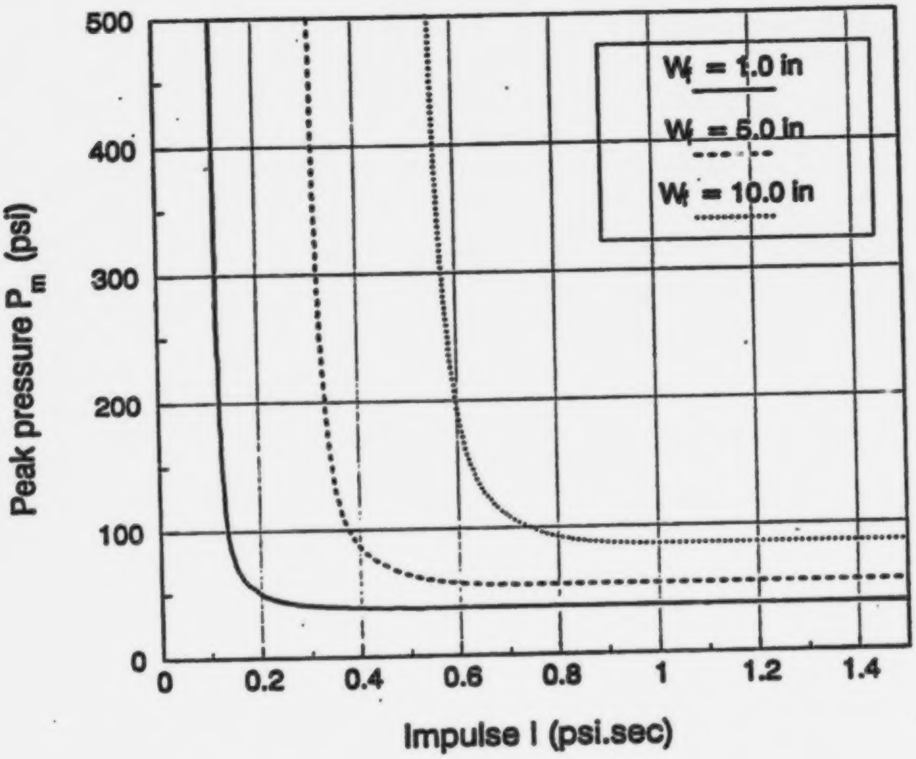

Fig. 1: Isoresponse curves for the DRES panel subjected to rectangular pressure pulses (h=0.25in)

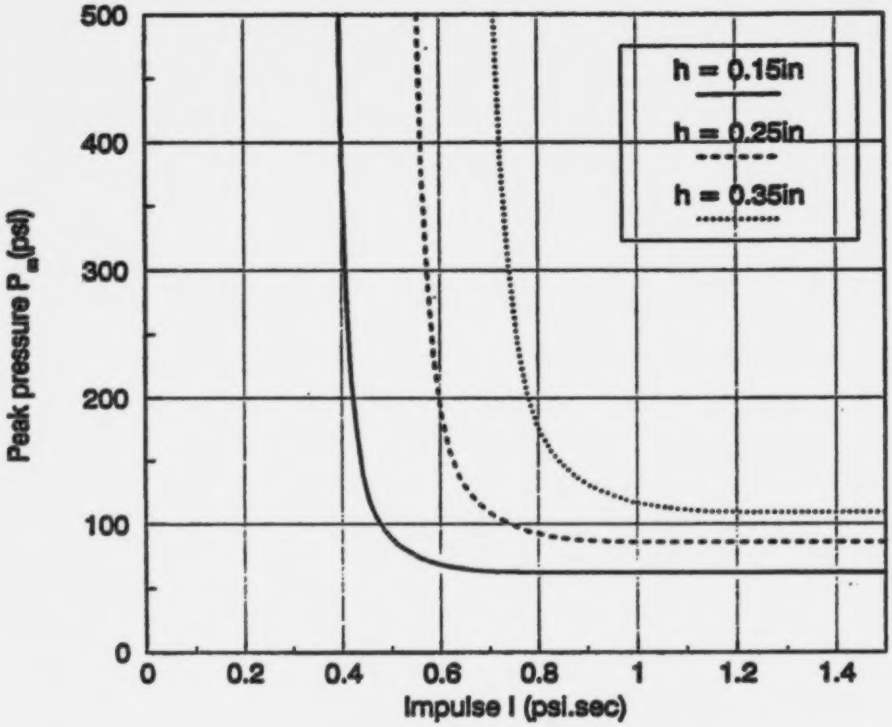

Fig. 2: Isoresponse curves for the DRES panel subjected to rectangular pressure pulses (W_f =10.0in)

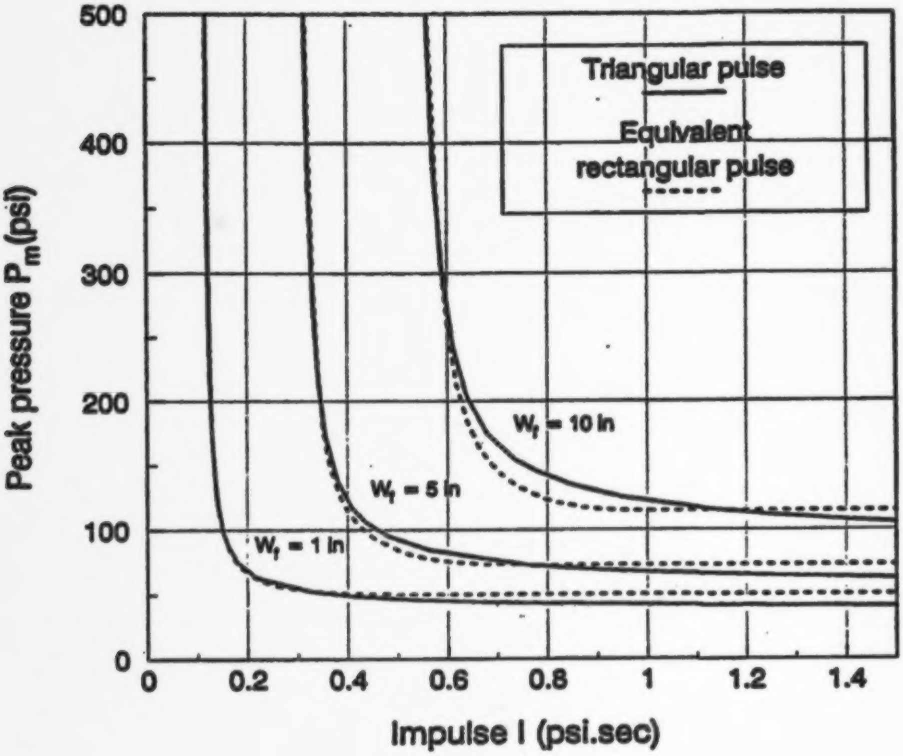

Fig. 3: Isoresponse curves for the DRES panel subjected to triangular and equivalent rectangular pressure pulses (h=0.25in)

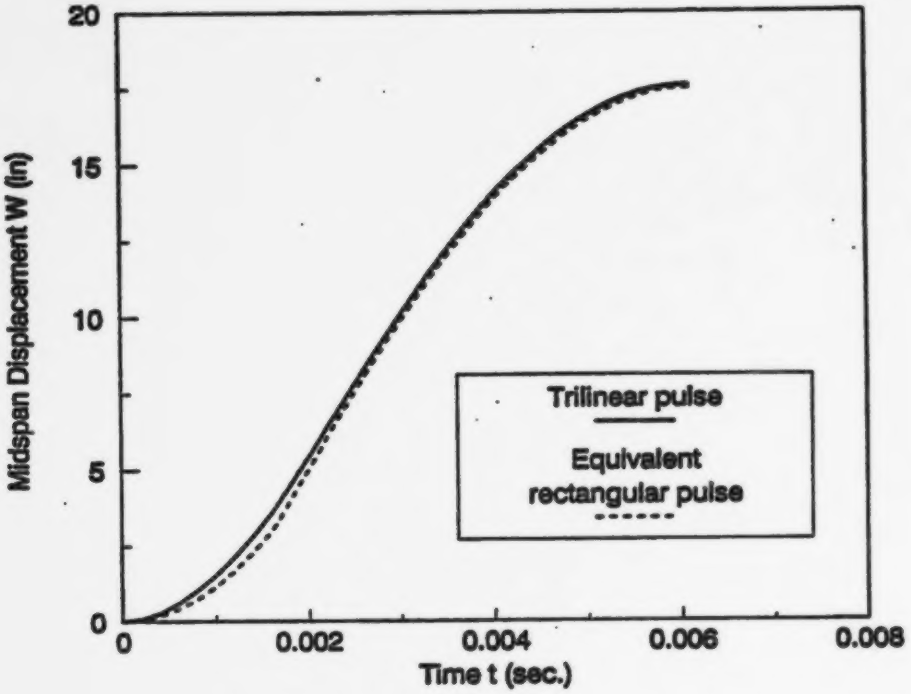

Fig. 4: Midspan displacement response of the DRES panel to trilinear and equivalent rectangular pulses(h=0.25in)

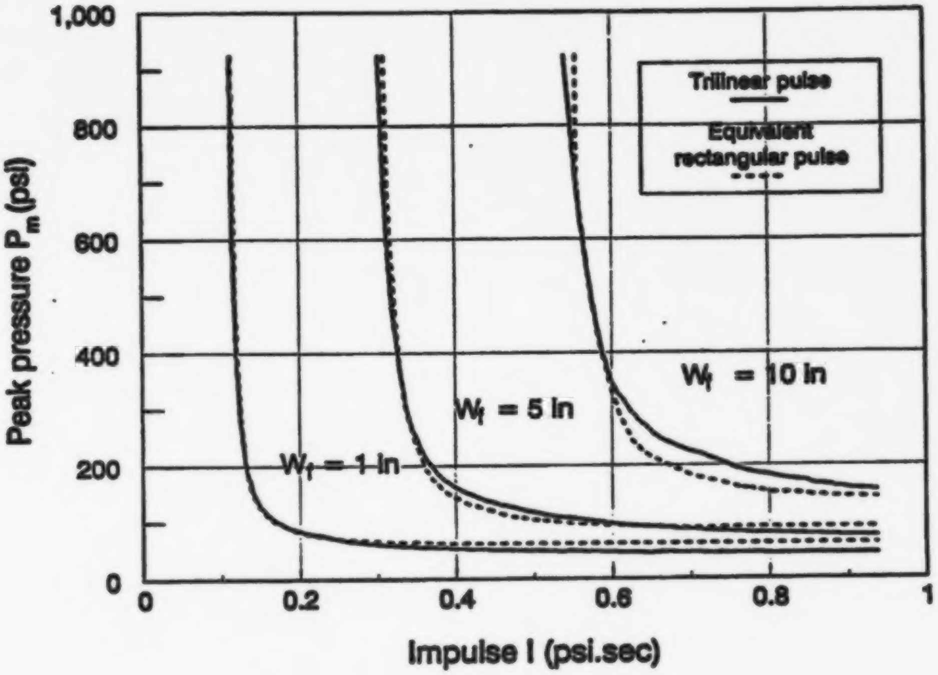

Fig. 5: Isoresponse curves for the DRES panel subjected to trilinear and equivalent rectangular representations of the HOB #315 pulse (h=0.25in)

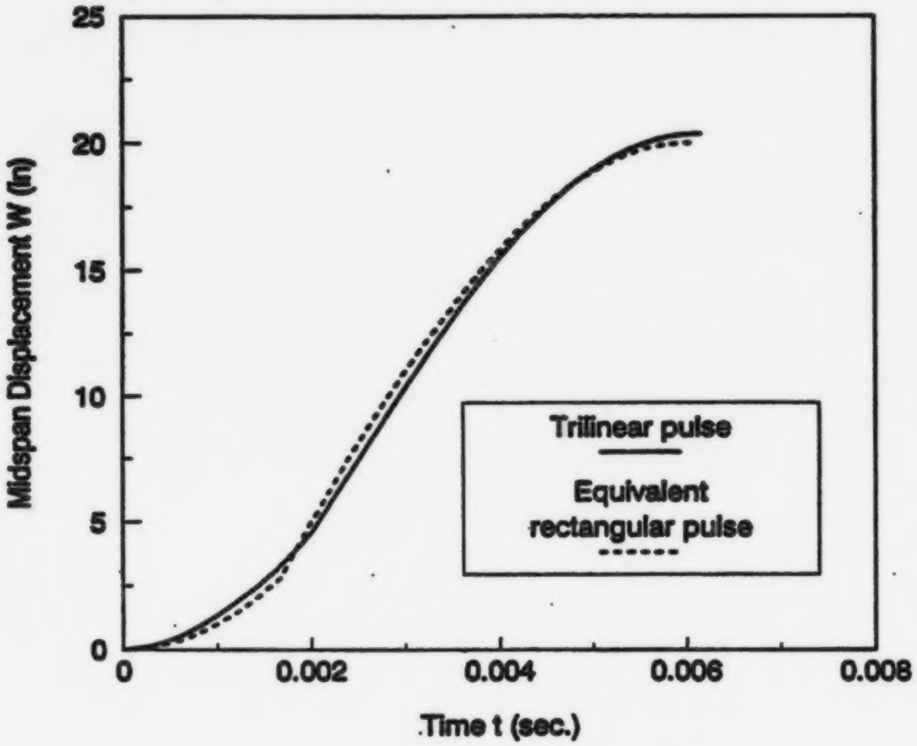

Fig. 6: Midspan displacement response of the DRES1B panel subjected to trilinear and equivalent rectangular representations of the HOB#315 pulse

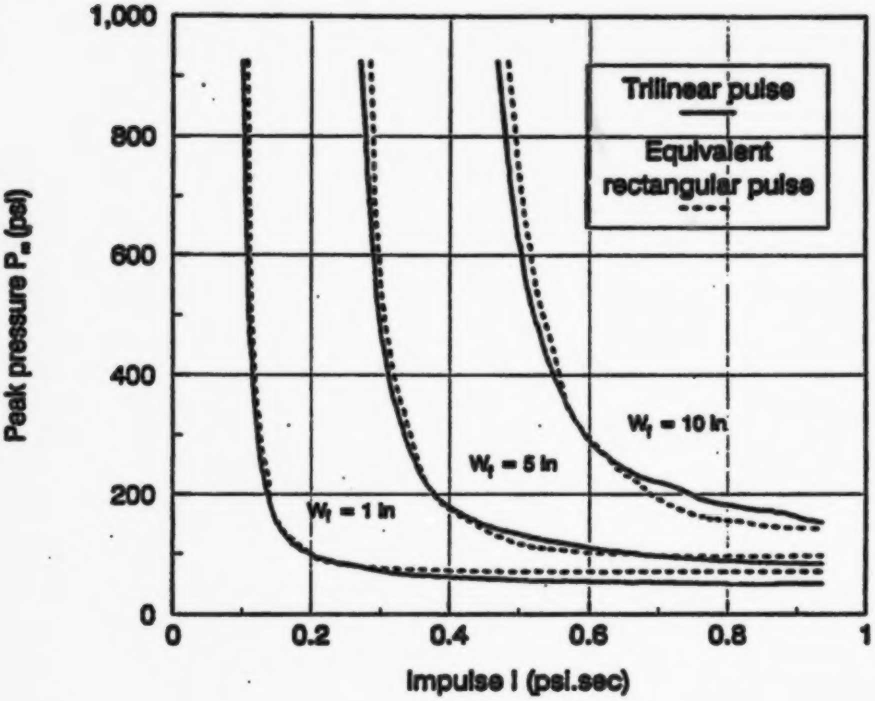

Fig. 7: Isoresponse curves for the DRES1B panel subjected to trilinear and equivalent rectangular representations of HOB #315 pulse (h=0.25in)

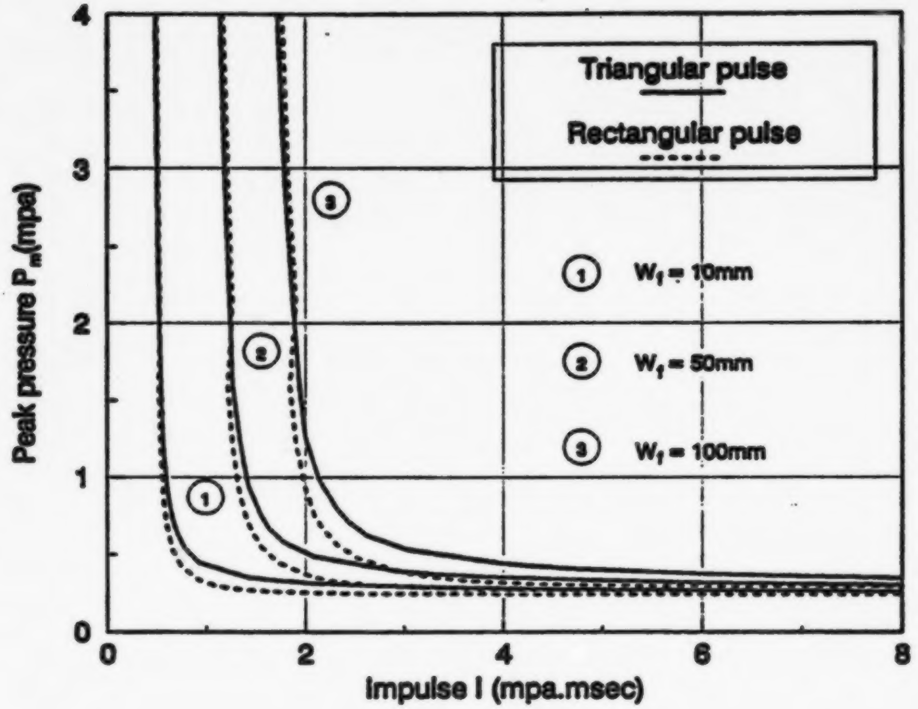

Fig. 8: Isoresponse curves for the square stiffened panel subjected to triangular and rectangular pressure pulses (h=7mm)

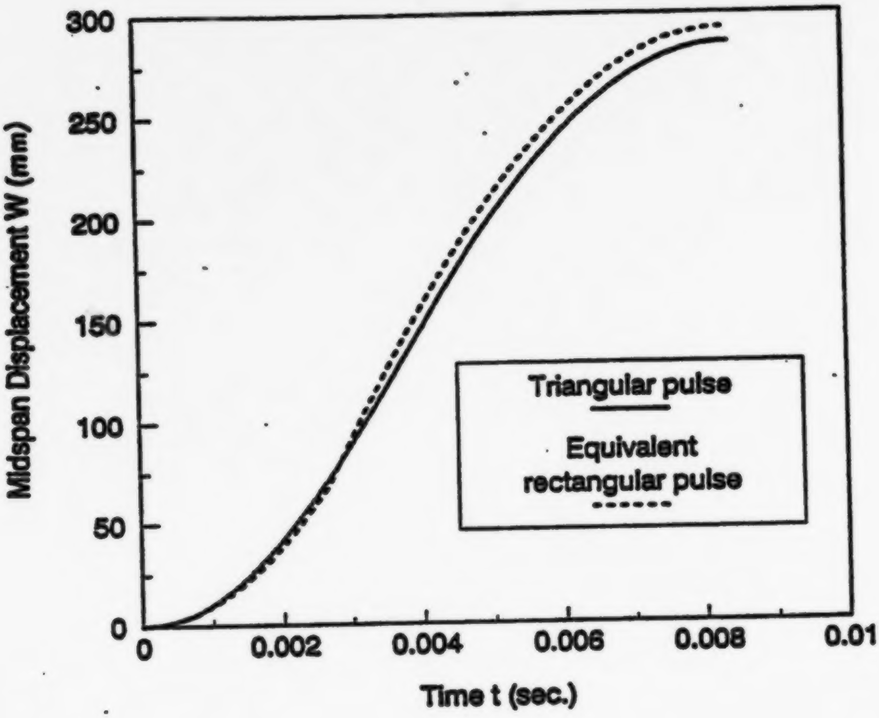

Fig. 9: Midspan displacement response of the square stiffened panel subjected to triangular and equivalent rectangular pulses (h=7mm)

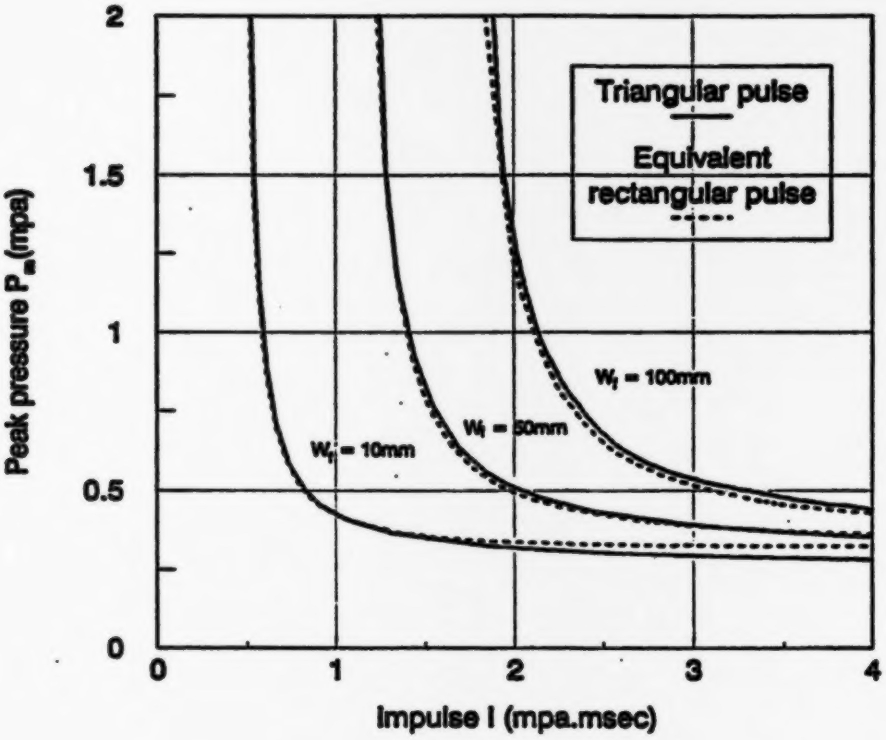

Fig. 10: Isoresponse curves for the square stiffened plate subjected to triangular and equivalent rectangular pulses (h=7mm).

Appendix IV

NONLINEAR STATIC AND DYNAMIC ANALYSIS OF STIFFENED BOX STRUCTURES USING SUPER FINITE ELEMENTS

by

J. Jiang and M.D. Olson

Structural Research Series

Report No. 36

I.S.S. No. 0318-3378

Department of Civil Engineering
University of British Columbia
Vancouver, B.C.

June, 1991

ABSTRACT

A super finite element model for nonlinear static and dynamic analysis of stiffened box structures is presented. The model is based on a new analysis philosophy as introduced by Koko and Olson in a recent study on stiffened plates [3]. The essence of the philosophy is to formulate specialized elements (called super elements) for particular applications and to ensure that these elements are capable of representing the overall response of the complete structure with reasonable accuracy but with a sacrifice in local detailed accuracy. The present work is directly motivated by the satisfactory performance of the elements in nonlinear analysis of stiffened plates. The objective of this work is to extend their applicability to more complex and larger structures such as stiffened box structures. The new developments made through the course of this work include modification of the displacement functions for both plate and beam elements to provide complete C^1 continuity and compatibility on the interfaces between various elements and applications to stiffened box structures. The new formulation has been applied to the static, vibration and transient analysis of various structures such as flat plates, folded plates and rectangular boxes. Both isotropic and beam stiffened structures are considered and the results obtained are compared with experimental results or other available solutions. In general, the numerical results obtained indicate that the new super element formulation can provide reasonable solutions for both linear and nonlinear problems of stiffened box structures.

TABLE OF CONTENTS

Page

1. INTRODUCTION 1

2. SUPER FINITE ELEMENT FORMULATION 4

2.1 Definition of the Super Finite Elements 4
2.2 Basis Displacement Functions 6
2.2.1 Plate Elements 7
2.2.2 Beam Elements 7
2.2.3 Some Remarks on the Elements 13
2.3 Strain Displacement Relations 15
2.4 Constitutive Relations 17
2.5 Virtual Work Principle 17
2.6 Mass and Damping Matrices 19
2.7 Stiffness Matrices 22
2.8 Load Vectors 26
2.9 Numerical Integration 28
2.10 Time Integration 29
2.11 Iterative Solution Procedure 30

3. ANALYSIS OF FOLDED PLATE AND BOX STRUCTURES 32

3.1 Folded Plate Model 32
3.1.1 Compatibility Conditions 33
3.1.2 Transformation Matrices 33
3.2 Rectangular Box Model 40
3.2.1 Compatibility Conditions 40
3.2.2 Transformation Matrices 43

4. NUMERICAL VERIFICATIONS ....

4.1 Static Analysis Results 46
4.1.1 Beams 47
4.1.2 Flat Plates 48
4.1.3 Tube Structures 51
4.1.4 Box Structures 56
4.2 Vibration Analysis Results 60
4.2.1 Flat Plates 60
4.2.2 Box Structures 62
4.3 Transient Analysis Results 64
4.3.1 Flat Plates 64
4.3.2 Box Structures 65

5. CONCLUSIONS 68

6. ACKNOWLEDGEMENTS 69

7. REFERENCES 70

TABLE OF CONTENTS (Continued)

Page

TABLES 72

8. APPENDICES 85

APPENDIX A - SHAPE FUNCTIONS FOR SUPER PLATE ELEMENTS 85

APPENDIX B - SHAPE FUNCTIONS FOR SUPER BEAM ELEMENTS 88

APPENDIX C - STRAIN-DISPLACEMENT MATRICES 90

APPENDIX D - CONSTITUTIVE MATRICES 98

APPENDIX E - BEAM TORSIONAL MASS MATRIX 99

APPENDIX F - GEOMETRIC STIFFNESS MATRICES 101

APPENDIX G - BEAM TORSIONAL STIFFNESS MATRIX 103

APPENDIX H - DIRECTION COSINES 105

APPENDIX I - TRANSFORMATION MATRICES FOR FOLDED PLATE MODEL 106

APPENDIX J - TRANSFORMATION MATRICES FOR RECTANGULAR BOX MODEL .. 107

APPENDIX K - THEORETICAL CALCULATIONS FOR CUBIC TUBE STRUCTURE .. 109

FIGURES 115

LIST OF TABLES

Page

Table 1: Nodal Degrees of Freedom for Plate Element ($\{\delta_e\}$) 72

Table 2: Nodal Degrees of Freedom for Beam Element ($\{\bar{\delta}_e\}$) 72

Table 3: Number of Gauss Integration Points 73

Table 4: Nodal Degrees of Freedom for Plate Element in Folded Plate Model ($\{\delta^*_e\}$) 73

Table 5: Nodal Degrees of Freedom for Beam Element in Folded Plate Model ($\{\bar{\delta}^*_e\}$) 74

Table 6: Sign Convention for Global Twist, $\bar{w}_{,xy_i}$ 74

Table 7: Convergence of Tip Deflection for Cantilever Beam 75

Table 8: Stress σ_x Calculated for Totally Fixed Boundary Conditions (ksi) 75

Table 9: Linear Elastic Response of Simply Supported Beam 75

Table 10: Linear Elastic Response of Simply Supported Square Plate .. 76

Table 11: Large Deflection Responses of Simply Supported Square Plate 76

Table 12: Large Deflection Elastic Response of Simply Supported Square Plate Without In-Plane Boundary Constraints 77

Table 13: Linear Elastic Response of Clamped Square Plate 77

Table 14: Linear Elastic Response of Clamped 2-Bay Stiffened Plate .. 78

Table 15: Linear Elastic Response of Clamped DRES1B Stiffened Panel 78

Table 16: Nonlinear Elastic Response of Clamped DRES1B Stiffened Panel 79

Table 17: Linear Elastic Results of Cubic Tube 79

Table 18: Linear and Nonlinear Results for Cubic Container 80

Table 19: Nonlinear Results for Two Thinner Cubic Containers 80

Table 20: Linear Elastic Response of Unstiffened Cubic Box 80

Table 21: Linear Elastic Response of Stiffened Cubic Box 81

LIST OF TABLES (Continued)

Page

Table 22: Natural Frequencies of Square Plate with Various Edge Constraints 81

Table 23: Natural Frequencies of 3-Bay Continuous Plates 82

Table 24: Natural Frequencies of 2x4 Bay Stiffened Plate with Clamped Edges (Hz) 82

Table 25: Natural Frequencies of Cubic Tube Structure 83

Table 26: Comparison of Present Predictions with Approximate Solutions for Natural Frequencies of Cubic Tube Structure (Hz) 83

Table 27: Natural Frequencies of Cubic Box Structure 84

Table 28: Comparison of Present Predictions with Approximate Solutions for the First Three Frequencies of Cubic Box Structure (Hz) 84

LIST OF FIGURES

Page

Fig. 1: A Typical Open-Ended, Rib-Stiffened Box Structure 115

Fig. 2: Assemblage of Plate and Beam Elements 116

Fig. 3: Nodal Configuration of Super Elements 117

Fig. 4: Rectangular Conforming Plate Bending Element [4] 118

Fig. 5: Rectangular Plane Stress Element [5] 119

Fig. 6: Shapes of Typical Blast Loads 120

Fig. 7: Super Finite Element Discretization of a Folded Plate Structure 121

Fig. 8: Two Adjacent Plate Elements Along an Angular Junction 122

Fig. 9: A Rectangular Close-Ended Box Structure 123

Fig. 10: A Three-Plate Corner Junction in Box Structure 124

Fig. 11: Configuration and Boundary Conditions of Cantilever Beam .. 125

Fig. 12: Configuration of 2-Bay Stiffened Plate 126

Fig. 13: Configuration of DRES1B Panel 127

Fig. 14: Configuration of Unstiffened Cubic Tube 128

Fig. 15: Comparison of Strain Energies for Unstiffened Cubic Tube Under Internal and External Pressure Load, Respectively ... 129

Fig. 16: Comparison of In-Plane Displacements for Unstiffened Cubic Tube Under Internal and External Pressure Load, Respectively 130

Fig. 17: Comparison of Bending Displacements for Unstiffened Cubic Tube Under Internal and External Pressure Load, Respectively 131

Fig. 18: Comparison of Strain Energies Obtained from Three Grid Discretizations for Unstiffened Cubic Tube 132

Fig. 19: Comparison of Panel Center Deflections Obtained from Three Grid Discretizations for Unstiffened Cubic Tube 133

Fig. 20: Configuration of Stiffened Cubic Tube 134

LIST OF FIGURES (Continued)

Page

Fig. 21: Bending Displacements at Points A and C of Interior-Beam-Stiffened Cubic Tube Under Internal Pressure Load 135

Fig. 22: Bending Displacements at Points A and C of Exterior-Beam-Stiffened Cubic Tube Under Internal Pressure Load 136

Fig. 23: Configuration of Cubic Container 137

Fig. 24: Configuration of Unstiffened Cubic Box 138

Fig. 25: Comparison of Strain Energies Obtained from Three Grid Discretizations for Unstiffened Cubic Box Under Internal and External Pressure Load, Respectively 139

Fig. 26: Comparison of In-Plane Displacements at Junction Mid-Point Obtained from Three Grid Discretizations for Unstiffened Cubic Box Under Internal and External Pressure Load, Respectively 140

Fig. 27: Comparison of Panel Center Deflections Obtained from Three Grid Discretizations for Unstiffened Cubic Box Under Internal and External Pressure Load, Respectively 141

Fig. 28: Nonlinear Panel Center Displacements for Unstiffened Cubic Box Under Internal and External Pressure Load, Respectively 142

Fig. 29: Large Deflection, Elastic-Plastic Displacement Profiles in Unstiffened Cubic Tube Due to Internal Pressure Load 143

Fig. 30: Large Deflection, Elastic-Plastic Displacement Profiles in Unstiffened Cubic Tube Due to External Pressure Load 144

Fig. 31: Configuration of Stiffened Cubic Box 145

Fig. 32: Bending Displacements at Points A and C in Interior-Beam-Stiffened Cubic Box Due to Internal Pressure Load 146

Fig. 33: Bending Displacements at Points A and C in Exterior-Beam-Stiffened Cubic Box Due to Internal Pressure Load 147

Fig. 34: Large Deflection, Elastic-Plastic Displacement Profiles in Interior-Beam-Stiffened Cubic Box Due to Internal Pressure Load 148

Fig. 35: Large Deflection, Elastic-Plastic Displacement Profiles in Exterior-Beam-Stiffened Cubic Box Due to Internal Pressure Load 149

LIST OF FIGURES (Continued)

Page

Fig. 36: Configuration of 3-Bay Continuous Plate 150

Fig. 37: Configuration and Discretization of 2x4 Bay Stiffened Plate 151

Fig. 38: Fundamental Mode Shape for Unstiffened Cubic Tube 152

Fig. 39: Transient Elastic Response of Simply Supported Square Plate Under Step Load 153

Fig. 40: Nonlinear Transient Elastic-Plastic Response of Clamped 2-Bay Stiffened Plate Under Blast Load 154

Fig. 41: Transient Elastic Response of Unstiffened Cubic Tube Under Step Internal Pressure Load 155

Fig. 42: Transient Elastic Response of Unstiffened Cubic Tube Under Step External Pressure Load 156

Fig. 43: Transient Elastic Response of Unstiffened Cubic Box Under Step Pressure Loads 157

Fig. 44: Nonlinear Transient Elastic-Plastic Response of Unstiffened Cubic Box Under Step Pressure Loads 158

1. INTRODUCTION

A stiffened box is an efficient structural component in supporting and transmitting pressure loads which are usually encountered in ship structures. This type of structure has also been used extensively in the construction of aircraft, bridges, offshore platforms and the cores of tall buildings. They are often referred to as thin-walled box structures. During the past few decades, a large number of developments in the analysis and design of these structures has taken place. However, most of the developments for non-curved box structures appear to be restricted to the linear analysis of box beams or girders under static loads [1,2]. As far as the static or dynamic large-deflection, elastic-plastic analysis is concerned, little work has been reported in the literature. As a consequence, there is a need for the development of numerical models which are capable of representing nonlinear static and dynamic response of stiffened box structures under complex loading conditions. It is the objective of this work to develop an accurate and efficient numerical analysis capability for preliminary design purposes.

The mechanical behaviour of stiffened box structures is very complicated even for linear static problems. Although there are a few analytical methods available for solving simple problems, it is difficult to extend them to certain classes of box type or cellular structures. For these structures, it is usually more convenient to resort to numerical methods such as the finite element method. In theory, the finite element method can deal with all structural problems. In practice, however, to model real engineering structures, it generally requires many elements with a huge amount of data preparation and computational times, thus making the analysis impractical for preliminary engineering design.

To improve the situation, a new analysis philosophy was introduced into the finite element formulation in a recent study on stiffened plates by Koko and Olson [3]. The essence of the philosophy is to formulate specialized elements (called super elements) for particular applications and to ensure that these elements are capable of representing the overall response of the complete structure with reasonable accuracy but with a sacrifice in local detailed accuracy. It has been shown that the analysis based on the super elements requires much less input data as well as computational times in comparison with conventional finite element analysis. To investigate their applicability to more complex and larger structures a similar formulation has been adopted in the present work. The new developments made through the course of this work include modification of the displacement functions for both plate and beam elements to provide complete C^1 continuity and compatibility on the interfaces between various elements in order to make them applicable to stiffened box structures.

This report presents the mathematical formulation of the new super elements for nonlinear static and dynamic analysis of stiffened box structures. In the following, the basic super finite element formulation is described first, in which the super element discretization, displacement functions and numerical techniques involved are briefly discussed. The applications of the super elements to folded plate and box structures are then discussed with the emphasis placed on element compatibility conditions and their associated transformation matrices. Finally, numerical investigations are carried out to verify the proposed formulation. Various response calculations which include static, transient and free vibration analyses are investigated. Many examples are presented and the results obtained are compared with experimental data or other available solutions. In the cases where neither experimental nor numerical results are available, a convergence study is performed by using refined grids. In general, the numerical results obtained indicate that the new super element formulation can provide reasonable solutions for both linear and nonlinear problems of stiffened box structures.

2. SUPER FINITE ELEMENT FORMULATION

This section is concerned with the formulation of a basic super finite element model for structures consisting of stiffened plate panels. This new model provides complete C^1 continuity for both plate and beam elements and ensures compatibility between beam and plate displacements, and moreover it can be easily extended to stiffened box structures which are discussed in the next section. In this section, the mathematical development of the model involving geometrical and material nonlinearities is presented, and is followed by brief discussions on the numerical techniques employed in the derivation of equilibrium equations, time-stepping and solution procedures.

2.1 Definition of the Super Finite Elements

Figure 1 illustrates a typical open-ended, rib-stiffened box structure which represents a pontoon used in ship architecture. The structure is essentially an assemblage of spatial (stiffened) plates joined together at right angles and welded along straight edges parallel to the length. Under external pressure loading, the complete structure will deform in a manner similar to a shell structure. That is, each plate undergoes not only bending but also in-plane deformation. This coupled bending and membrane action is one of the basic mechanical characteristics exhibited by the box type of structure. To properly simulate this coupling phenomenon, it is necessary that both in-plane and out-of-plane displacements are included in the element formulation. In this work, the displacement fields for the plate and stiffener elements have been carefully chosen to include all possible linear and nonlinear deformation modes displayed in stiffened box structures. These elements have been termed super elements since only a single element is required to capture the basic response of a rectangular plate or a slender beam.

In the context of the above super element notion, the complete structure, as shown in Fig. 1, is first divided into a number of sub-structures (e.g. stiffened plates), and each of the sub-structures is then discretized by a few super plate and beam elements. Unlike conventional finite element models, the present one uses only a single plate element to represent each panel bay of a sub-structure and a single beam element for each of the stiffeners running along the edges of the panel. Consider an isolated panel bay with two adjacent beams as show in Fig. 2. The local rectangular coordinate system (x,y,z) is attached to the mid-surface of the plate element. The global coordinate system (X,Y,Z) can be selected differently from the local system to define the location of the complete structure. In the following discussions, all the displacement variables are referred to the local system unless otherwise indicated.

Figure 3 shows details of the nodal configuration associated with the plate (Fig. 3(a)) and beam (Fig. 3(b)) elements. It can be seen that the plate element has a total of nine actual nodes, numbered 1 to 9. In addition, twelve 'extra nodal variables' labelled u_8, $u_9,\ldots,u_{13}$, and v_8, $v_9,\ldots,v_{13}$ are introduced. Physically, these 'extra' degrees of freedom represent the amplitudes of the trigonometric functions used to describe the in-plane displacements and they are simply lumped at the mid-side and central nodes marked 5 to 9. The degrees of freedom associated with each node are summarized in Table 1. In this table, u and v represent the in-plane displacements in the x and y directions, respectively; $u_{,y} = \partial u/\partial y$ and $v_{,x} = \partial v/\partial x$ are the in-plane slopes; w is the out-of-plane displacement; $w_{,x} = \partial w/\partial x$ and $w_{,y} = \partial w/\partial y$ are the bending slopes; and $w_{,xy} = \partial^2 w/\partial x \partial y$ is the twist. The positive directions of u, v and w are defined as shown in Fig. 2. Overall, the plate element has 59 degrees of freedom.

The beam element has three actual nodes, numbered 1 to 3. In analogy to the plate element, the 'extra nodal variables' labelled u_4 and u_5 are nodal amplitudes and they are taken as nodal variables at the middle node, marked 3. The nodal degrees of freedom are listed in Table 2 for a beam element running along the x and y directions, respectively. It is noted that θ is the torsional angle, $\theta_{,x} = d\theta/dx$ and $\theta_{,y} = d\theta/dy$. Totally, there are 19 degrees of freedom for a beam element.

It should be noted that for simple beam problems the nodal variables are located along the beam centroidal axis whereas for stiffened plate problems all nodal variables are assumed to be located at the mid-surface of the plate. Thus, no additional degrees of freedom are introduced at a beam-plate connection. It is also noted that inter-element continuity of displacements between two adjacent plate elements or between a plate and a beam element is ensured all along the plate edge, while continuity between two adjacent beam elements is provided at the inter-element nodes.

2.2 Basis Displacement Functions

In the present approach, the displacement functions incorporated in the super elements are specially formulated so that the elements not only satisfy all the kinematic requirements for stiffened plate structures but also have the ability to simulate all possible deformation modes. In particular, the elements incorporate a set of analytical functions, which are usually trigonometric and hyperbolic functions, in addition to the usual finite element polynomial functions. These analytical functions provide the elements, on top of the conventional finite element capability, with some additional mathematical and physical merits exhibited by the finite strip method. Therefore, the super elements developed herein possess both the versatility of the conventional finite element method and the efficiency of the finite strip method. The details of these functions are given in the following for plate and beam elements, respectively.

2.2.1 Plate Elements

A typical super plate element of length a and width b is depicted in Fig. 3(a). The element has 9 actual nodes and 59 nodal variables. Table 1 summarizes the degrees of freedom defined at each node. The displacements within the element are described by the following functions.

$$u = \sum_{i=1}^{11} N_i^u \delta_i^u + \sin 2\pi\xi [L_1(\eta), L_2(\eta), L_3(\eta)] \begin{bmatrix} u_8 \\ u_9 \\ u_{10} \end{bmatrix}$$

$$+ \sin 4\pi\xi [L_1(\eta), L_2(\eta), L_3(\eta)] \begin{bmatrix} u_{11} \\ u_{12} \\ u_{13} \end{bmatrix} \qquad (1)$$

$$v = \sum_{i=1}^{11} N_i^v \delta_i^v + \sin 2\pi\eta [L_1(\xi), L_2(\xi), L_3(\xi)] \begin{bmatrix} v_8 \\ v_9 \\ v_{10} \end{bmatrix}$$

$$+ \sin 4\pi\eta [L_1(\xi), L_2(\xi), L_3(\xi)] \begin{bmatrix} v_{11} \\ v_{12} \\ v_{13} \end{bmatrix} \qquad (2)$$

$$w = \sum_{i=1}^{16} N_j^w \delta_j^w + \phi(\xi)[H_1(\eta), H_2(\eta), H_3(\eta), H_4(\eta)] \begin{bmatrix} w_5 \\ w_{,y^5} \\ w_7 \\ w_{,y^7} \end{bmatrix}$$

$$+ \phi(\eta)[H_1(\xi), H_2(\xi), H_3(\xi), H_4(\xi)] \begin{bmatrix} w_8 \\ w_{,x^8} \\ w_6 \\ w_{,x^6} \end{bmatrix} \quad (3)$$

$$+ \phi(\xi)\phi(\eta)w_9$$

where u, v are the two in-plane displacements in the x and y directions, respectively; w is the out-of-plane displacement in the z direction, and $\xi = x/a$ and $\eta = y/b$ are the two non-dimensional coordinates.

In Eqs. (1) to (3), N_i^u, N_i^v and N_j^w represent the shape functions for the u, v and w displacements, respectively; δ_i^u, δ_i^v and δ_j^w are the nodal variables associated with the u, v and w displacement fields, respectively; $L_i(\xi)$ (or $L_i(\eta)$) denotes the quadratic Lagrange interpolation polynomials and $H_j(\xi)$ (or $H_j(\eta)$) the cubic Hermitian polynomials. All of these functions and variables are given explicitly in Appendix A. The ϕ function used in Eq. (3) is the first symmetric vibration mode of a clamped beam and is given by,

$$\phi(\xi) = \frac{\alpha(\sinh\beta\xi - \sin\beta\xi) + (\cosh\beta\xi - \cos\beta\xi)}{A_\phi} \quad (4)$$

where

$$A_\phi = \alpha(\sinh 0.5\beta - \sin 0.5\beta) + (\cosh 0.5\beta - \cos 0.5\beta)$$

$$\alpha = \frac{\cos\beta - \cosh\beta}{\sinh\beta - \sin\beta} \quad \text{and} \quad \beta = 4.7300407448 \quad (5)$$

For convenience, Eqs. (1) to (3) can be written in the following matrix form,

$$\begin{bmatrix} u \\ v \\ w \end{bmatrix} = [N]\{\delta_e\} \qquad (6)$$

where [N] is the matrix of shape functions, and $\{\delta_e\}$ is the element nodal variable vector. Both are given explicitly in Appendix A.

It should be mentioned here that in the conventional finite element formulation, a shape function for any nodal variable has a unit value at that node and zero value at all other nodes. However this does not hold for all the shape functions used in the present formulation. For example, the functions $N^u_1,\ldots,N^u_{11}$, $N^v_1,\ldots,N^v_{11}$ and $N^w_1,\ldots,N^w_{16}$ do satisfy the requirement of having a unit value at one node and zero at all other nodes, and hence the nodal variables corresponding to these functions are the actual displacements at the respective nodes. On the other hand, the remaining functions $N^u_{12},\ldots,N^u_{17}$, $N^v_{12},\ldots,N^v_{17}$ and $N^w_{17},\ldots,N^w_{25}$ do not satisfy this requirement. This is because of the analytical functions involved in the formulation of these shape functions. As the consequence, the variables corresponding to these functions only represent displacement amplitudes at the respective locations. To obtain the actual displacements for these variables, the contributions from all of the other shape functions involved have to be included in the calculation.

2.2.2 Beam Elements

Figure 3(b) shows a super beam element of length a, with its nodal configuration. The element has 3 actual nodes and a total of 19 degrees of freedom. Table 2 summarizes the degrees of freedom defined at each node. The element displacement fields referred to the centroidal axis of a beam in the x direction are described by

$$u = u_p + e\frac{dw}{dx}$$

$$= [L_1(\xi), L_2(\xi), L_3(\xi)]\begin{bmatrix} u_1 \\ u_2 \\ u_3 \end{bmatrix} + u_4 \sin 2\pi\xi + u_5 \sin 4\pi\xi$$

$$+ e[H_1'(\xi), H_2'(\xi), H_3'(\xi), H_4'(\xi)]\begin{bmatrix} w_1 \\ w_{,x^1} \\ w_2 \\ w_{,x^3} \end{bmatrix} + e\phi'(\xi)w_3 \qquad (7)$$

$$w = [H_1(\xi), H_2(\xi), H_3(\xi), H_4(\xi)]\begin{bmatrix} w_1 \\ w_{,x^1} \\ w_2 \\ w_{,x^2} \end{bmatrix} + \phi(\xi)w_3 \qquad (8)$$

$$v = v_p + e\theta$$

$$= [H_1(\xi), H_2(\xi), H_3(\xi), H_4(\xi)] \begin{bmatrix} v_1 \\ v_{,x^1} \\ v_2 \\ v_{,x^2} \end{bmatrix}$$

$$+ e[H_1(\xi), H_2(\xi), H_3(\xi), H_4(\xi)] \begin{bmatrix} \theta_1 \\ \theta_{,x^1} \\ \theta_2 \\ \theta_{,x^2} \end{bmatrix} + e\phi(\xi)\theta_3 \qquad (9)$$

$$\theta = [H_1(\xi), H_2(\xi), H_3(\xi), H_4(\xi)] \begin{bmatrix} \theta_1 \\ \theta_{,x^1} \\ \theta_2 \\ \theta_{,x^2} \end{bmatrix} + \phi(\xi)\theta_3 \qquad (10)$$

where u, w and v represent the axial, vertical bending (in the z direction), and lateral bending (in the y direction) displacements about the centroidal axis of the beam, respectively, and θ is the torsional angle; the subscript p refers to the plate; v_i and $v_{,xi}$ are the nodal lateral bending displacement and slope variables; θ_i and $\theta_{,xi}$ are the nodal rotation and twist variables; the primes in Eq. (7) denote differentiation with respect to the x coordinate, and e is the distance between the centroidal axis of the beam and the mid-surface of the plate. For the local coordinate system adopted in

Fig. 2, e should be assigned a negative value if the beam is located on the positive z axis side of the plate.

Equations (7) to (10) can also be re-arranged in the matrix form

$$\begin{bmatrix} u \\ w \\ \theta \\ v \end{bmatrix} = [\bar{N}]\,\{\bar{\delta}_e\} \qquad (11)$$

where $[\bar{N}]$ is the beam shape function matrix, and $\{\bar{\delta}_e\}$ is the beam nodal displacement vector. Both are given explicitly in Appendix B.

It may be noted that the functions in the last four columns of $[\bar{N}]$ (Appendix B), e.g. $\phi(\xi)$, $e\phi(\xi)$, $e\phi'(\xi)$, $\sin 2\pi\xi$ and $\sin 4\pi\xi$, do not rigourously satisfy the requirements of a shape function and hence the variables corresponding to these functions, i.e. w_3, θ_3, u_4 and u_5, only represent the displacement amplitudes of the beam at the respective locations.

To further facilitate discussion of the beam mass and stiffness calculations to be presented in Sections 2.5 and 2.6, $[\bar{N}]$ can be partitioned into two parts

$$\begin{Bmatrix} u \\ w \end{Bmatrix} = [\bar{N}_I]\,\{\bar{\delta}_e^{\,I}\} \qquad (12)$$

and

$$\begin{Bmatrix} \theta \\ v \end{Bmatrix} = [\bar{N}_{II}]\,\{\bar{\delta}_e^{\,II}\} \qquad (13)$$

Here, the first part, Eq. (12), describes the beam axial and vertical bending displacement fields, while the second part accounts for the beam torsional angle and lateral bending displacement. Details of $[\bar{N}_I]$, $[\bar{N}_{II}]$, $\{\bar{\delta}_e^{\,I}\}$ and $\{\bar{\delta}_e^{\,II}\}$ are provided in Appendix B.

2.2.3 Some Remarks on the Elements

The basic displacement functions have now been specified, and the derivation of all the element property matrices such as mass and stiffness matrices is a standard process. Before doing that, it is worthwhile to give some remarks on the compatibility, convergence and order of accuracy as provided by these elements.

1) Consider the w displacement field for the super plate element. If one temporarily neglects all the other terms except for the first term in Eq. (3), the well-known rectangular plate bending element developed by Bogner et al. [4] is obtained (Fig. 4). The additional terms in Eq. (3) included herein are to improve the element. Firstly, the last term $\phi(\xi)\phi(\eta)$ in Eq. (3) can capture the basic response of a fully clamped plate even with a single plate element. Secondly, the remaining two terms (second and third terms of Eq. (3)) are included to ensure the compatibility of displacements between plate and beam elements. The w displacement field is C^1 continuous and it will result in, for linear plate bending problems, convergence of strain energy of the order of $O(\ell^4)$ where ℓ is a characteristic dimension of the element.

2) It is known that the in-plane displacement fields u and v for the super plate element must contain cubic terms if compatibility with the bending displacement field w is to be maintained in the case of folded plates.

To achieve this goal the shape functions contained in the first term of Eqs. (1) and (2) are based on a cubic-quadratic assumption as adopted by Tinawi [5] (Fig. 5). For example, the u displacement varies cubically along the edges 2-3 and 1-4 and has a quadratic variation elsewhere. These shape functions not only ensure C^0 continuity between adjacent elements but also provide a consistent order of convergence in strain energy. Note that this is a basic change from the initial super element work [3] which was based on a quadratic-quadratic assumption. The other two terms involving sine functions in Eqs. (1) and (2) are added to adequately simulate nonlinear geometric effects in a large deflection analysis. The sine functions are interpolated by quadratic functions in the other direction in order to maintain the same order of accuracy and complete compatibility between plate and beam elements, and also to simulate shear lag effects. The plate element formulated here is a conforming element.

3) To be consistent with the super plate element, care has been taken in the choice of the displacement fields for the super beam element. It is seen that quadratic polynomials are included in the first term of Eq. (7) for the axial displacement u and cubic polynomials in the first terms of Eqs. (8) to (10) for the vertical bending w, lateral bending v and torsional θ displacements, respectively. These polynomials will ensure an order of accuracy ($O(\ell^4)$) in strain energy consistent with the plate elements. The axial displacement field is C^0 continuous while the vertical and lateral bending displacement and rotational fields are all C^1 continuous. It is also noted that all the extra terms introduced into Eqs. (7) to (10) are fully compatible with the corresponding terms in the plate element. Hence, this beam element is also a conforming element.

2.3 Strain Displacement Relations

Based on thin plate theory, the strain-displacement relations including first order nonlinearities are given by

$$\begin{aligned} \epsilon_x &= \frac{\partial u}{\partial x} - z\,\frac{\partial^2 w}{\partial x^2} + \frac{1}{2}\left(\frac{\partial w}{\partial x}\right)^2 \\ \epsilon_y &= \frac{\partial v}{\partial y} - z\,\frac{\partial^2 w}{\partial y^2} + \frac{1}{2}\left(\frac{\partial w}{\partial y}\right)^2 \qquad (14) \\ \gamma_{xy} &= 2\epsilon_{xy} = \frac{\partial u}{\partial y} + \frac{\partial v}{\partial x} - 2z\,\frac{\partial^2 w}{\partial x \partial y} + \frac{\partial w}{\partial x}\,\frac{\partial w}{\partial y} \end{aligned}$$

where ϵ_x, ϵ_y and ϵ_{xy} are the components of Cauchy's strain tensor, and γ_{xy} is the engineering shear strain. In Eqs. (14), u, v, and w are the displacements of the mid-surface of the plate in the x, y and z directions, respectively. It is recognized that the nonlinear terms in Eqs. (14) are important if the deflections are equal to or larger than one thickness of the plate but still small relative to the lateral dimensions of the plate.

Similarly, the strain-displacement relation for a beam element can also be obtained by using slender beam theory. The results are listed below.

$$\epsilon_x = \frac{du_p}{dx} + (e-z)\,\frac{d^2 w}{dx^2} + \frac{1}{2}\left(\frac{dw}{dx}\right)^2 \qquad (15)$$

for a beam element in the x direction, and

$$\epsilon_y = \frac{dv_p}{dy} + (e-z)\,\frac{d^2 w}{dy^2} + \frac{1}{2}\left(\frac{dw}{dy}\right)^2 \qquad (16)$$

for a beam element in the y direction. Here e is the eccentricity of the beam centroid from the mid-surface of a plate, and z is referred to the centroidal axis of a beam.

Substitution of Eqs. (1) to (3) into Eq. (14) results in

$$\{\epsilon\} = \begin{bmatrix} \epsilon_x \\ \epsilon_y \\ \gamma_{xy} \end{bmatrix} = [B_o]\{\delta_e\} + \{C_o\} \tag{17}$$

where $[B_o]$ is the linear strain-displacement matrix given by

$$[B_o] = \begin{bmatrix} \frac{\partial}{\partial x} & 0 & -z\,\frac{\partial^2}{\partial x^2} \\ 0 & \frac{\partial}{\partial y} & -z\,\frac{\partial^2}{\partial y^2} \\ \frac{\partial}{\partial y} & \frac{\partial}{\partial x} & -2z\,\frac{\partial^2}{\partial x \partial y} \end{bmatrix} [N] \tag{18}$$

and $\{C_o\}$ contains the nonlinear terms of the strain-displacement relations, that is

$$\{C_o\} = \begin{bmatrix} \frac{1}{2}\,\frac{\partial N_i^w}{\partial x}\,\frac{\partial N_j^w}{\partial x}\,w_i\,w_j \\ \frac{1}{2}\,\frac{\partial N_i^w}{\partial y}\,\frac{\partial N_j^w}{\partial y}\,w_i\,w_j \\ \frac{1}{2}\,\left(\frac{\partial N_i^w}{\partial x}\,\frac{\partial N_j^w}{\partial y} + \frac{\partial N_i^w}{\partial x}\,\frac{\partial N_j^w}{\partial y}\right)\,w_i\,w_j \end{bmatrix} ,\ i,j=1,2,\ldots,25 \tag{19}$$

It is noted that the summation convention is assumed for the repeated indices i and j in Eq. (19). The relevant equations for beam elements can also be obtained by using Eqs. (15) or (16), together with Eq. (12), and the details are presented in Appendix C.

2.4 Constitutive Relations

To account for the material nonlinearities, a classical incremental plasticity theory is adopted for this work. For simplicity, the plasticity theory applied here uses the simple von Mises yield criterion with the associated flow rule, and assumes isotropic linear hardening of the material and neglects time-dependent and thermal effects. The detailed discussion about the theory can be found in many textbooks [6].

The constitutive relations are generally expressed in the following incremental form,

$$\{d\sigma\} = [D]\{d\epsilon\} \tag{20}$$

where $\{d\sigma\}^T = (d\sigma_x, d\sigma_y, d\tau_{xy})$ and $\{d\epsilon\}^T = (d\epsilon_x, d\epsilon_y, d\gamma_{xy})$ are the incremental stress and strain vectors, respectively, and [D] is the constitutive matrix. Details of [D] are provided in Appendix D for both linear elastic and elasto-plastic materials.

2.5 Virtual Work Principle

In order to establish a set of discretized equations of equilibrium for a nonlinear static or dynamic system the principle of virtual work is usually applied. By this principle it is required that for a dynamic system to be in equilibrium at time t, the total internal virtual work be equal to the total external virtual work, including the effect of inertia and damping forces, for any given virtual displacement which satisfies the prescribed kinematic boundary conditions. That is,

$$\int_V \rho\{\delta u\}^T\{\ddot{u}\}dV + \int_V \mu\{\delta u\}^T\{\dot{u}\}dV + \int_V \{\delta\epsilon\}^T\{\sigma\}dV = \int_A \{\delta u\}^T\{F\}dA \qquad (21)$$

where ρ is the mass density, μ is the viscous damping parameter, V and A are, respectively, the volume and surface area of the element, $\{\delta u\}$ is the virtual displacement vector, $\{\delta\epsilon\}$ is the virtual strain vector, $\{\ddot{u}\}$ and $\{\dot{u}\}$ are, respectively, the acceleration and velocity vectors, $\{F\}$ represents the applied surface traction vector, and $\{\sigma\}^T = (\sigma_x, \sigma_y, \tau_{xy})$ is the stress vector. For a static system, the velocity and acceleration terms $\{\ddot{u}\}$ and $\{\dot{u}\}$ in Eq. (21) vanish.

After introducing the assumed displacement functions, Eqs. (1) to (3), and the strain-displacement relations, Eq. (14) into Eq. (21), the governing equations of motion for a single plate element are obtained as

$$[m]\{\ddot{\delta}_e\} + [c]\{\dot{\delta}_e\} + \{\gamma^{int}\} = \{\gamma^{ext}\} \qquad (22)$$

where

$[m] = \int_V \rho[N]^T[N]dV$ = consistent mass matrix,

$[c] = \int_V \mu[N]^T[N]dV$ = viscous damping matrix,

$\{\gamma^{int}\} = \int_V [[B_o]+[C_L]]^T\{\sigma\}dV$ = internal force vector,

$\{\gamma^{ext}\} = \int_A [N]^T\{F\}dA$ = external load vector, and $\{\dot{\delta}_e\}$, $\{\ddot{\delta}_e\}$ represent the nodal velocity and acceleration vectors, respectively, [N] is the matrix of shape functions in Eq. (6), and $[C_L]$ is the nonlinear strain-displacement matrix obtained from $\{C_o\}$ (Eq. 17) when the first variation is taken. See details in Appendix C.

A similar set of equations of motion can also be derived for a single beam element by substituting the appropriate beam functions (Eqs. (7) and (8)) and using the respective beam strain-displacement relation (Eqs. (15) or (16)), as given in Appendix C. However, the resulting equations are based solely on the beam bending theory so that the effects of beam torsion and lateral bending have not yet been taken into account. In this work linear theory has been applied to formulate the torsional and lateral bending mass and stiffness matrices which will be discussed in detail in Sections 2.6 and 2.7.

Once the equations of motion for each element are formulated, the global equations of motion are obtained by the systematic assemblage of all element contributions. The final form can be expressed as

$$[M]\{\ddot{\delta}\} + [C]\{\dot{\delta}\} + \{R^{int}\} = \{R^{ext}\} \qquad (23)$$

where $\{\dot{\delta}\}$ and $\{\ddot{\delta}\}$ represent the global velocity and acceleration vectors of the complete structure, and all the other matrices and vectors denoted by capitals are the global quantities of those defined in Eq. (22), respectively.

2.6 Mass and Damping Matrices

As indicated by Eq. (22), all the relevant element properties have to be calculated before solving the governing equations of motion. In this section the mass and damping matrices will be explicitly formulated for both the super plate and beam elements.

Using the definitions introduced in Eq. (22) and the appropriate shape functions, the element consistent mass matrix can now be written for a plate element as

$$[m_p] = \int_V [N]^T \rho [N] dV \tag{24}$$

and for a beam bending element as

$$[m_b^b] = \int_V [\tilde{N}_I]^T \rho [\tilde{N}_I] dV \tag{25}$$

where ρ is the mass per unit volume, and $[N]$, $[\tilde{N}_I]$ are, respectively, the shape function matrices for the plate and beam bending elements defined previously. The matrix $[m_b^b]$ is of the order 10x10.

As mentioned before, the effects of beam torsion and lateral bending are also important for the response analysis and hence they should be included in the mass formulation. Consider the beam rotation and lateral bending velocities at the centroid. One can write the kinetic energy for a beam in the x direction as

$$T = \frac{1}{2} \omega^2 \rho \int_o^a (J_c \theta^2 + Av^2) dx \tag{26}$$

where ω is the natural frequency of the beam, ρ is the mass density, J_c is the polar moment of inertia about the centroid, A is the cross-sectional area, and a is the length of the beam. Substituting the first part of Eq. (9) into Eq. (26) the expression for the kinetic energy can be expanded to the form

$$T = \frac{1}{2}\,\omega^2\rho \int_o^a [J_o\theta^2 + A(v_p^2 + 2ev_p\theta)]dx \qquad (27)$$

where J_o is the polar moment of inertia about the mid-surface of the plating. Hence, the mass matrix for the beam torsion and lateral bending effects is simply given by

$$(m_b^t)_{ij} = \rho J_o \int_o^a (\bar{N}_{II}^p)_{,1i}(\bar{N}_{II}^p)_{,1j}dx + \rho A\int_o^a (\bar{N}_{II}^p)_{,2i}(\bar{N}_{II}^p)_{,2j}dx$$

$$+ \rho Ae\int_o^a \left[(\bar{N}_{II}^p)_{,1i}(\bar{N}_{II}^p)_{,2j} + (\bar{N}_{II}^p)_{,2i}(\bar{N}_{II}^p)_{,1j}\right] dx \qquad (28)$$

Introducing the shape functions $[\bar{N}_{II}^p]$ (see Appendix B) into Eq. (28), after integrations, the torsional mass matrix can be written explicitly as

$$[m_b^t] = [m_{b1}^t] + [m_{b2}^t] + [m_{b3}^t] \qquad (29)$$

which is of the order 9x9. Details of the three matrices $[m_{b1}^t]$, $[m_{b2}^t]$ and $[m_{b3}^t]$ are given in Appendix E.

The total beam mass matrix is then obtained by combining the matrix $[m_b^b]$ (Eq. 25) with the matrix $[m_b^t]$ (Eq. 29), i.e.

$$[m_b] = [\bar{m}_b^b] + [\bar{m}_b^t] \qquad (30)$$

where the matrices $[\bar{m}_b^b]$ and $[\bar{m}_b^t]$ are the so-called "expanded" matrices of order 19x19 and correspond to the original matrices $[m_b^b]$ and $[m_b^t]$, respectively. The derivation above is also valid for a beam in the y direction when the variables a, v_p and dx are replaced by b, u_p, and dy, respectively.

It is assumed for simplicity that the element damping matrix is proportional to the mass matrix for both the plates and beams, which is of the form

$$[c_i] = \gamma\ [m_i] \tag{31}$$

where γ is a constant to be determined from the damping parameter μ, i.e. $\gamma = \mu/\rho$, and the subscript i is used to designate types of elements. For example, i=p means a plate element, whereas i=b, a beam element.

2.7 Stiffness Matrices

Consider a nonlinear static problem for now. The general equations of equilibrium, Eq. (22), are simplified to the form

$$\Phi(\{\delta\}) = \{\gamma^{int}(\{\delta\})\} - \{\gamma^{ext}\} = 0 \tag{32}$$

which is a set of nonlinear equations, and Φ is considered to be a vector in the following. For an exact solution $\{\delta\}$, the Φ vector is zero, but for an approximate solution $\{\delta\}_i$, which does not exactly satisfy equilibrium, Φ is non-zero. To improve the approximate solution of the displacement vector, the problem has to be resolved in an iterative manner. First, expanding Eq. (31) by Taylor series about a known solution $\{\delta\}_i$ so that,

$$\Phi(\{\delta\}_{i+1}) = \Phi(\{\delta\}_i) + \frac{\partial\Phi}{\partial\{\delta\}}\bigg|_i (\{\delta\}_{i+1} - \{\delta\}_i) + \ldots. \qquad (33)$$

and then neglecting terms $O(|\{\delta\}|^2)$, with the notion $\{\Delta\delta\} = \{\delta\}_{i+1} - \{\delta\}_i$, results in

$$\Phi(\{\delta\}_{i+1}) = \Phi(\{\delta\}_i) + \frac{\partial\Phi}{\partial\{\delta\}}\bigg|_i \{\Delta\delta\} = 0 \qquad (34)$$

or in a more convenient form

$$\Phi(\{\delta\}_i) + [k_T]\{\Delta\delta\} = 0 \qquad (35)$$

where $[k_T]$ is termed the tangent stiffness matrix. The form of $[k_T]$ for the present formulation can be obtained by differentiating $\{\gamma^{int}\}$ with respect to the displacement vector $\{\delta\}$ since $\{\gamma^{ext}\}$ is not a function of $\{\delta\}$. That is,

$$[k_T] = \frac{\partial\{\gamma^{int}\}}{\partial\{\delta\}} = \frac{\partial}{\partial\{\delta\}}\int_V [[B_o] + [C_L]]^T\{\sigma\}dV \qquad (36)$$

Using the appropriate constitutive relations, Eq. (20) and after some mathematical manipulations, the final form of $[k_T]$ can be expressed as

$$[k_T] = \int_V ([[B_o]+[C_L]]^T[D]\ [[B_o]+[C_L]] + [\Omega])dv \qquad (37)$$

where $[\Omega]$ is the so-called geometric stiffness matrix given by

$$[\Omega] = \left(\frac{\partial[C_L]^T}{\partial\{\delta\}}\right)\{\sigma\} \qquad (38)$$

A typical entry in the geometric stiffness matrix [Ω] is given by

$$\Omega_{ij} = \frac{\partial N_r^w}{\partial x} \frac{\partial N_s^w}{\partial x} \sigma_x + \frac{\partial N_r^w}{\partial y} \frac{\partial N_s^w}{\partial y} \sigma_y + \left(\frac{\partial N_r^w}{\partial x} \frac{\partial N_s^w}{\partial y} + \frac{\partial N_r^w}{\partial y} \frac{\partial N_s^w}{\partial x}\right) \tau_{xy}$$

$$(i,j = 1,2,\ldots,59;\ r,s = 1,2,\ldots,25) \tag{39}$$

for a plate element, and

$$\Omega_{ij} = \frac{dN_r^b}{dx} \frac{dN_s^b}{dx} \sigma_x \quad (i,j = 1,2,\ldots,10;\ r,s = 1,2,\ldots,5) \tag{40}$$

for a beam element in the x direction. In Eqs. (39) and (40), the indices i and j represent, respectively, the row and column numbers of that entry in the element matrix [Ω]. There is one-to-one correspondence between the indices, i,j and r,s which can be found in Appendix F. In Eq. (40), N_r^b and N_s^b are the shape functions for the beam bending displacement w such that

$$N_p^b = H_p(\xi) \quad (p = 1,\ldots,4) \qquad \text{and } N_5^b = \phi(\xi) \tag{41}$$

It is noted that for the beam element Eq. (37) only represents the vertical bending stiffness $[k_b^b]$. To include the effects of torsion and lateral bending, consider a beam element in the x-direction again. The strain energy of the beam due to torsion, lateral bending and warping is calculated from

$$U = \frac{1}{2} GJ \int_0^a \left(\frac{d\theta}{dx}\right)^2 dx + \frac{1}{2} EI_{zz} \int_0^a \left(\frac{d^2v}{dx^2}\right)^2 dx + \frac{1}{2} E\Gamma \int_0^a \left(\frac{d^2\theta}{dx^2}\right)^2 dx \tag{42}$$

where G, E are the shear and Young's modulus, respectively, J is the torsional constant, I_{zz} is the moment of inertia about the z axis, Γ is the warping constant, and a is the length of the beam. Substituting Eq. (9) into Eq. (42) and utilizing the same notations as adopted in Eq. (27) results in

$$U = \frac{1}{2} GJ \int_o^a (\frac{d\theta}{dx})^2 dx + \frac{1}{2} EI_{zz} \int_o^a \left[(\frac{d^2v_p}{dx^2})^2 + 2e \frac{d^2v_p}{dx^2} \frac{d^2\theta}{dx^2} + e^2 (\frac{d^2\theta}{dx^2})^2 \right] dx$$

$$+ \frac{1}{2} E\Gamma \int_o^a (\frac{d^2\theta}{dx^2})^2 dx \qquad (43)$$

where v_p is the lateral displacement at the mid-surface of the plate and e is the eccentricity of the beam centroid from the mid-surface of the plate. After substituting from Eq. (13) and carrying out the integrations, the resulting stiffness matrices may be put in the convenient form

$$[k_b^t] = [k_{b1}^t] + [k_{b2}^t] + [k_{b3}^t] + [k_{b4}^t] \qquad (44)$$

which is of the order 9x9. Details of the four matrices $[k_{b1}^t]$, $[k_{b2}^t]$, $[k_{b3}^t]$ and $[k_{b4}^t]$ are given in Appendix G.

The total beam stiffness matrix $[k_t]$ is then obtained by a systematic assemblage of the two matrices $[k_b^b]$ (Eq. 37) and $[k_b^t]$ (Eq. 44) into one matrix in the same manner as for the mass matrix (Eq. 30).

For a beam in the y direction, the above derivation is still valid if all the relevant functions and variables are changed accordingly to the appropriate ones.

2.8 Load Vectors

The types of loads which are of interest in this work are mainly shock wave loads such as air-blast or underwater shock loads. These loads are usually described by a pressure distribution function q over the structure such that

$$q = q(x,y,z,t) \tag{45}$$

where x, y and z are the coordinates of a point at which the pressure is measured, and t is the time variable. In practice, q may be a very complex function of time and location. However, the pressure loads can be classified into two categories. The first category concerns only uniformly distributed loads with temporal variations, and the second includes more general spatially varying loads.

For the first category, the load can be expressed as

$$q(t) = q_m f(t) \tag{46}$$

where q_m is the peak pressure and f(t) represents the temporal variation which can be effectively modelled by

$$f(t) = \left[\begin{array}{lll} (1-t/\tau)^{\frac{1}{\lambda}-1} & , & 0 \le t \le \tau \\ 0 & , & t > \tau \end{array} \right. \tag{47}$$

where τ is the duration of the load and λ is the decay parameters. Various shapes of blast loads can be simulated by this function with an appropriate value of λ, as shown in Figure 6(a). It is also possible to account for blast loads of arbitrary time histories. In this case $q(t)$ is specified by discrete data points with linear interpolation between points as depicted in Fig. 6(b).

The element load vector for these simplified loading cases can be calculated in a closed form via the following expression

$$\{P\} = \{r^{ext}\} = \int_A [N]^T \{F\} dA \tag{48}$$

where $[N]$ is the shape function matrix and $\{F\}$ is the surface traction vector which contains only the pressure load q. After using the appropriate shape functions and carrying out the integration, the load vectors for both the plate and beam elements are obtained and they take the following forms:

(a) for a plate element

$$\begin{aligned}\{P\}^T = \frac{abq}{144} (&0, 0, 36, 0, 0, 6a, 6b, ab, 0, 0, 36, 0, 0, -6a, \\ &6a, -ab, 0, 0, 36, 0, 0, -6a, -6b, ab, 0, 0, 36, \\ &0, 0, 6a, -6b, -ab, 0, 72\psi, 12\psi b, 0, 0, 0, 72\psi, \\ &-12\psi a, 0, 0, 0, 72\psi, -12\psi b, 0, 0, 0, 72\psi, 12\psi a, \\ &0, 0, 0, 0, 144\psi^2, 0, 0, 0, 0)\end{aligned} \tag{49}$$

where a,b are the length and width, respectively, of the plate element, q is the pressure in units of force per unit area, and ψ is the constant evaluated by

$$\psi = \int_o^1 \phi(\xi) d\xi = \frac{1}{A_\phi \beta} [\alpha(\cosh\beta + \cos\beta - 2) + (\sinh\beta - \sin\beta)] \tag{50}$$

(b) for a beam element

$$\{P\}^T = \frac{aq}{12}(0, 0, 6, 0, a, 0, 0, 0, 0, 6, 0, -a, 0, 0, 0, 12\psi, 0, 0, 0) \tag{51}$$

where a is the length of the beam element and q is in units of force per unit length.

For the loads in the second category, the spatial distribution of the pressure varies with time. In this case, exact integration of Eq. (48) is not possible, and hence numerical integration is used to generate the element load vectors at each time step or load increment. In the computer codes, a user-supplied external module has been created for reading in the complex time-pressure history at each Gauss point in the plane of the plate.

2.9 Numerical Integration

The Gaussian integration scheme is used to evaluate the volume integrals in Eqs. (24),(25) and (37). The number of integration points used in a given direction depends on the assumed shape functions as well as the material behaviour. It was found from previous work [3] that the numbers of integration points in each direction, summarized in Table 3, are adequate for most of the analyses using the similar super elements. Hence, for the present work, the same sampling scheme is adopted herein. It should be noted that in Table 3 the numbers quoted with the asterisk symbol are for rectangular beam elements. For beams of I or T cross-sections an additional point is introduced for each flange. Details of the location and weighting coefficients of the sampling points for both the plate and beam elements can be found in [3].

2.10 Time Integration

It is noted that the discretized equations of motion, Eq. (23), must be solved by employing a numerical time integration procedure. There are a number of direct time integration schemes available in the literature [7], and the choice of an appropriate scheme is, to a large extent, dependent on the nature of the problem to be dealt with. For simplicity as well as efficiency, the popular Newmark-β scheme is implemented in this work. This is an implicit method which is unconditionally stable for linear problems and a single step method. As compared to explicit methods it does not require a diagonalized mass matrix and permits use of large time steps without causing numerical instability problems. However, the accuracy of the solutions generally decreases with increasing size of the time step, and a proper time step has to be used in order to achieve an acceptably accurate solution.

The Newmak-β method is based on the following assumptions

$$\{\dot{\delta}\}_{n+1} = \frac{2}{\Delta t}\left(\{\delta\}_{n+1}-\{\delta\}_n\right) - \{\dot{\delta}\}_n \tag{52}$$

$$\{\delta\}_{n+1} = \frac{4}{\Delta t^2}\left(\{\delta\}_{n+1}-\{\delta\}_n\right) - \frac{4}{\Delta t}\{\dot{\delta}\}_n - \{\ddot{\delta}\}_n \tag{53}$$

where Δt is a time step, and the subscripts, n and n+1 denote times at t_n and t_{n+1}, respectively. Assuming that the solution of Eq. (23) at $t_n = n\Delta t$ is known, the object is to find the new solution at the next time step $t_{n+1} = (n+1)\Delta t$. Substitution of Eqs. (52) and (53) in Eq. (23) and with the help of the incremental form for the internal force vector,

$$\{R^{int}\}_{n+1} = \{R^{int}\}_n + [K_t]_n \left(\{\delta\}_{n+1}-\{\delta\}_n\right) \tag{54}$$

the following generalized equation is obtained

$$[K^{eff}]\ \{\Delta\delta\} = \{R^{eff}\}_{n+1} \tag{55}$$

where $\{\Delta\delta\}$ is the incremental displacement vector defined as

$$\{\Delta\delta\} = \{\delta\}_{n+1} - \{\delta\}_n \tag{56}$$

$[K^{eff}]$ is the effective stiffness matrix given by

$$[K^{eff}] = \frac{4}{\Delta t^2}\,[M] + \frac{2}{\Delta t}\,[C] + [K_t]_n \tag{57}$$

and $\{R^{eff}\}$ is the effective load vector given by

$$\begin{aligned}\{R^{eff}\} = {} & \{R^{ext}\}_{n+1} - \{R^{int}\}_n \\ & + [M](\frac{4}{\Delta t}\,\{\dot{\delta}\}_n + \{\ddot{\delta}\}_n) + [C]\{\dot{\delta}\}_n\end{aligned} \tag{58}$$

2.11 Iterative Solution Procedure

For nonlinear problems as considered in this work, Eq. (55) represents a set of nonlinear equations due to the presence of geometrical and material nonlinearities. In the process of solving the equations at time t_{n+1}, the tangent stiffness matrix $[K_t]_n$ in Eq. (57) is estimated based on the previous known solution $\{\delta\}_n$. If $[K_t]_n$ is not an accurate representation of the tangent stiffness matrix from time t_n to t_{n+1}, the solution of Eq. (55) for $\{\delta\}_{n+1}$ will be in error. Such an error will result in a residual nodal force vector given by the imbalance of Eq. (23) as

$$\{R^{err}\} = \{R^{ext}\}_{n+1} - [M]\{\ddot{\delta}\}_{n+1} - [C]\{\dot{\delta}\}_{n+1} - \{R^{int}\}_{n+1} \qquad (59)$$

If the norm of $\{R^{err}\}$ is not within the tolerance specified, sub-iterations must be performed. In this work, both the full Newton-Raphson and the modified Newton-Raphson iteration procedures are implemented, and the choice of one or the other is generally problem-dependent.

It is found from the previous experience [9] that use of the time step size suggested below,

$$\Delta t \le \begin{cases} T_f/10, & \text{for non-dissipative systems} \\ T_f/40, & \text{for dissipative systems} \end{cases} \qquad (60)$$

usually results in a reasonably accurate solution for the Newmark-β method. In Eq. (60), T_f denotes the fundamental period of the system. However, it is noted that these suggestions are only good for moderate blast loads. When the structure is subjected to a very intense blast load, or a load in which its spatial distribution is rapidly changing with time, the allowable time step size is rather governed by the speed of propagation of plastic deformation or by the time scale of significant spatial variation of the applied load.

3. ANALYSIS OF FOLDED PLATE AND BOX STRUCTURES

In this section the basic super finite element model developed in Section 2 for stiffened plate structures is extended to folded plate and stiffened box structures by introducing appropriate transformation matrices. To formulate these matrices, it is necessary to investigate compatibility conditions along the element boundaries where adjacent plates form an angle junction or a 90-degree corner. To ensure compatibility between elements at those locations, some of the degrees of freedom are replaced by new variables, and some are eliminated through boundary conditions. In the end the modified versions of the elements still maintain all of the features contained in the original elements. Two models are presented in this section. The first one is a folded plate model which involves minimum transformation of nodal variables, whereas the second is a general model which is applicable to the folded plate and rectangular box structures.

3.1 Folded Plate Model

The super finite element discretization of a folded plate structure is shown in Fig. 7. To simplify the model the global rectangular coordinate system (X,Y,Z) is defined in such a manner that the Y axis is parallel to the longitudinal direction of the folded plates. Figure 8 shows two adjacent elements along an angular junction (e.g. ABCF and FCDE) isolated from the complete structure in Fig. 7. It is seen in this figure that a local coordinate system (x,y,z) is established on the mid-surface for each of the plate elements. The local y axis for both elements is assumed to be in the same direction as the global Y axis, while the local x and z axes are defined in the transverse and the thickness directions of the elements, respectively.

A set of local coordinates (x,y,z) is related to the global ones (X,Y,Z) by the direction cosines a_{ij} in the form

$$\begin{bmatrix} x \\ y \\ z \end{bmatrix} = \begin{bmatrix} a_{11} & a_{12} & a_{13} \\ a_{21} & a_{22} & a_{23} \\ a_{31} & a_{32} & a_{33} \end{bmatrix} \begin{bmatrix} X \\ Y \\ Z \end{bmatrix} \tag{61}$$

or in short form

$$\{x\} = [\lambda]\{X\} \tag{62}$$

where $\{x\}^T = (x,y,z)$, $\{X\}^T = (X,Y,Z)$, and $[\lambda]$ represents the coordinate transformation matrix. The direction cosines in Eq. (61) can be obtained from the known global coordinates of nodes 1, 2 and 4 (Fig. 3(a)). See Appendix H for details.

3.1.1 Compatibility Conditions

Modelling of the folded plate structure is essentialy a 3-dimensional problem. The super elements developed in the previous section have to be properly transformed from the local system (x,y,z) to the global system (X,Y,Z) if the inter-element compatibility of displacements is to be maintained. Due to the fact that some additional functions are introduced in the super element formulation, the transformation of the elements is not trivial as in conventional finite elements. One has to carefully investigate the displacement variation along all sides of the elements to ensure compatibility between various elements.

For the super plate element in Fig. 3(a), node 9 is an internal node and, hence, no transformation is necessary for the degrees of freedom associated with that node. However, the remaining degrees of freedom are all defined along the element boundaries and, in this case, care has to be taken to ensure that the transformation does not ruin the compatibility conditions. Consider the element ABCF shown in Fig. 8. It is seen that the side 2-3 is right at the junction between two plates. Along this junction the in-plane displacement component u from the element ABCF must be compatible with the bending displacement w from the neighbouring element FCDE. It can be shown that both the u and w displacements will vary cubically along the side 2-3 if the bending amplitude, w_6 (associated with the ϕ function) at the mid-side node is set to zero. In this work the requirement of $w_6=0$ at the junction is enforced by applying appropriate boundary conditions so that no special transition element is needed. It may be noted that the v displacement is defined to be tangent to the junction and thus its compatibility is automatically satisfied.

Next, examine the displacement field along the other side 3-4. Since two adjacent elements are situated on the same plate, the displacements u, v and w are always continuous across the boundary. However, dificulties are encountered if the in-plane slope $v_{,x}$ at the corner node 3 is to be transformed to a global variable. To overcome the problem, it is assumed that $v_{,x}$ is only continuous across the side 3-4 but discontinuous over the side 2-3. In other words, $v_{,x}$ is no longer a common variable between the elements ABCF and FCDE. Therefore, the $v_{,x}$ variables at nodes 3 and 4 are now moved to the mid-side node 7. Similarly, the $v_{,x}$ variables at nodes 1 and 2 are moved to node 5. All the variables defined at nodes 5 and 7 will not be transformed and are referred to the local system only.

To further facilitate the element transformation, three commonly used rotations θ_x, θ_y and θ_z are introduced as the degrees of freedom to replace $w_{,y}$, $w_{,x}$ and $u_{,y}$, respectively. Assuming that

$$\begin{aligned} \theta_x &= w_{,y} \\ \theta_y &= -w_{,x} \\ \theta_z &= -u_{,y} \end{aligned} \tag{63}$$

the modified displacement vector is then given by

$$\begin{aligned} \{\delta_e{}^*\}^T = (&u_1, v_1, w_1, \theta_{x1}, \theta_{y1}, \theta_{z1}, w_{,xy1}, u_2, v_2, w_2, \theta_{x2}, \\ &\theta_{y2}, \theta_{z2}, w_{,xy2}, u_3, v_3, w_3, \theta_{x3}, \theta_{y3}, \theta_{z3}, w_{,xy3}, \\ &u_4, v_4, w_4, \theta_{x4}, \theta_{y4}, \theta_{z4}, w_{,xy4}, u_5, w_5, \theta_{x5}, u_8, \\ &u_{11}, v_{,x1}, v_{,x2}, v_5, w_6, \theta_{y6}, v_9, v_{12}, u_6, w_7, \theta_{x7}, \\ &u_9, u_{12}, v_{,x4}, v_{,x3}, v_6, w_8, \theta_{y8}, v_8, v_{11}, u_7, v_7, \\ &w_9, u_{10}, v_{10}, u_{13}, v_{13}) \end{aligned} \tag{64}$$

The relation between $\{\delta_e\}$ and $\{\delta_e{}^*\}$ is defined through matrix $[\chi_I]$ shown in Appendix I, and given by

$$\{\delta_e\} = [\chi_I]\{\delta_e{}^*\} \tag{65}$$

The degrees of freedom associated with each node are summarized in Table 4 for this folded plate model.

In the case when the folded plates are reinforced by a system of orthogonal beams to enhance their load carrying capacities, it is necessary that the super beam element be also transformed. Based on the same assumptions as discussed above, the displacement vector $\{\bar{\delta}_e\}$ is modified into the following forms,

(a) for a beam in the x-direction

$$\{\bar{\delta}_e^*\}^T = (u_1, v_1, w_1, \theta_{x1}, \theta_{y1}, w_{,xy1}, u_2, v_2, w_2, \theta_{x2}, \theta_{y2}, w_{,xy2}, u_3, w_3, \theta_{x3}, u_4, u_5, v_{,x1}, v_{,x2}) \tag{66}$$

where $\theta_{xi} = \theta_i$, $\theta_{yi} = -w_{,xi}$ and $w_{,xyi} = \theta_{,xi}$.

(b) for a beam in the y-direction

$$\{\bar{\delta}_e^*\}^T = (u_1, v_1, w_1, \theta_{x1}, \theta_{y1}, \theta_{z1}, w_{,xy1}, u_2, v_2, w_2, \theta_{x2}, \theta_{y2}, \theta_{z2}, w_{,xy2}, u_3, w_3, \theta_{y3}, v_4, v_5) \tag{67}$$

where $\theta_{xi} = w_{,yi}$, $\theta_{yi} = \theta_i$, $\theta_{zi} = -u_{,yi}$ and $w_{,xyi} = \theta_{,yi}$.

It is noted that in Eq. (66) the variables $v_{,x1}$ and $v_{,x2}$ are moved from nodes 1 and 2, respectively, to the middle node 3 (Fig. 3(b)). Table 5 provides a list of the nodal variables associated with each node. There is a similar relation between $\{\bar{\delta}_e\}$ and $\{\bar{\delta}_e^*\}$ as given by Eq. (65) but with a different $[\bar{\chi}_I]$ matrix. See Appendix I for details.

3.1.2 Transformation Matrices

After introducing the modified nodal variable vector $\{\delta_e^*\}$ the super plate element is now ready to be transformed to a global system (XYZ). Referring to the global displacement vector by $\{\bar{\delta}_e\}$ such that

$$\{\bar{\delta}_e\}^T = (\bar{u}_1, \bar{v}_1, \bar{w}_1, \bar{\theta}_{x1}, \bar{\theta}_{y1}, \bar{\theta}_{z1}, w_{,xy1}, \bar{u}_2, \bar{v}_2, \bar{w}_2, \bar{\theta}_{x2},$$
$$\bar{\theta}_{y2}, \bar{\theta}_{z2}, w_{,xy2}, \bar{u}_3, \bar{v}_3, \bar{w}_3, \bar{\theta}_{x3}, \bar{\theta}_{y3}, \bar{\theta}_{z3}, w_{,xy3},$$
$$\bar{u}_4, \bar{v}_4, \bar{w}_4, \bar{\theta}_{x4}, \bar{\theta}_{y4}, \bar{\theta}_{z4}, w_{,xy4}, u_5, w_5, \theta_{x5}, u_8,$$
$$u_{11}, v_{,x1}, v_{,x2}, v_5, w_6, \theta_{y6}, v_9, v_{12}, u_6, w_7, \theta_{x7},$$
$$u_9, u_{12}, v_{,x4}, v_{,x3}, v_6, w_8, \theta_{y8}, v_8, v_{11}, u_7, v_7,$$
$$w_9, u_{10}, v_{10}, u_{13}, v_{13}) \qquad (68)$$

then, the vector $\{\delta_e^*\}$ corresponding to the local system (xyz), given by Eq. (64), is transformed such that

$$\{\delta_e^*\} = [\Lambda_I]\ \{\bar{\delta}_e\} \qquad (69)$$

where $[\Lambda_I]$ is the transformation matrix of order 59x59 given by

$$[\Lambda_I] = \begin{bmatrix} \underset{7x7}{[Q_I]} & & & & \\ & \underset{7x7}{[Q_I]} & & & \\ & & \underset{7x7}{[Q_I]} & & \\ & & & \underset{7x7}{[Q_I]} & \\ & & & & \underset{31x31}{[I]} \end{bmatrix} \qquad (70)$$

in which $[I] = [\delta_{ij}]$ is a unit matrix, and

$$[Q_I] = \begin{bmatrix} [\lambda] & & \\ & [\lambda] & \\ & & 1 \end{bmatrix} \tag{71}$$

Similarly, for beam elements in the y-direction, the vector $\{\delta_e^*\}$ is transformed such that

$$\{\bar{\delta}_e^*\} = [\bar{\Lambda}_I] \{\bar{\bar{\delta}}_e\} \tag{72}$$

where $\{\bar{\bar{\delta}}_e\}$ is the beam global vector given by

$$\{\bar{\bar{\delta}}_e\}^T = (\bar{u}_1, \bar{v}_1, \bar{w}_1, \bar{\theta}_{xi}, \bar{\theta}_{y1}, \bar{\theta}_{z1}, w_{,xy1}, \bar{u}_2, \bar{v}_2, \bar{w}_2, \bar{\theta}_{x2},$$
$$\bar{\theta}_{y2}, \bar{\theta}_{z2}, w_{,xy2}, v_3, w_3, \theta_{y3}, v_4, v_5) \tag{73}$$

and $[\bar{\Lambda}_I]$ is the beam transformation matrix given by

$$[\bar{\Lambda}_I] = \begin{bmatrix} \underset{7x7}{[Q_I]} & & \\ & \underset{7x7}{[Q_I]} & \\ & & \underset{5x5}{[I]} \end{bmatrix} \tag{74}$$

where $[Q_I]$ is defined by Eq. (71).

It is noted that for beams in the x-direction no transformation is needed. Furthermore, the extra bending displacement variable at the middle node 3, w_3, is forced to zero through boundary conditions in the manner similar to the plate elements.

Now the mass and stiffness matrices as well as the applied load vector corresponding to the global system (XYZ) can be obtained using Eqs. (65) and (69), thus

$$
\begin{aligned}
[\bar{m}_p] &= [T_{PI}]^T[m_p][T_{PI}] \\
[\bar{k}_T] &= [T_{PI}]^T[k_T][T_{PI}] \qquad (75) \\
\{\bar{P}\} &= [T_{PI}]^T\{P\}
\end{aligned}
$$

where $[T_{PI}]$ is the total transformation matrix given by

$$[T_{PI}] = [\chi_I][\Lambda_I] \qquad (76)$$

Similarly, for the beam elements in the y-direction, using Eqs. (67) and (72) yields

$$
\begin{aligned}
[\bar{m}_b] &= [T_{bI}]^T[m_b][T_{bI}] \\
[\bar{k}_b] &= [T_{bI}]^T[k_b][T_{bI}] \qquad (77) \\
\{\bar{P}_b\} &= [T_{bI}]^T\{P_b\}
\end{aligned}
$$

with

$$[T_{bI}] = [\tilde{\chi}_I][\tilde{\Lambda}_I] \qquad (78)$$

3.2 Rectangular Box Model

Unlike the folded plate structure which is basically a prismatic structure, a rectangular box is a real 3-dimensional structure in which six plates are joined together along three mutually perpendicular lines (called principal axes), as shown in Fig. 9. It is assumed that the global axes X, Y and Z are defined along the three principal axes, respectively. Moreover, the local axes x and y are selected to be in the positive direction of the global axes. For the box type of structures, the element transformation is much more complex than that for the folded plate structures. One of the difficulties encountered is that the two in-plane slope $u_{,y}$ and $v_{,x}$ and the twist $w_{,xy}$ are not generally transformable in 3-dimensional space. However, thanks to the rectangular shape of the box, the problem can be resolved by using proper physical assumptions. The model developed in this section is a generalized one which is also suitable for the folded plate structures discussed in the previous section. The performance of the present model, in comparison with the folded plate model, will be investigated in Section 4 through numerical examples.

3.2.1 Compatibilty Conditions

In development of the rectangular box model the difficulties arise mainly from the three-plate corner junction shown in Fig. 10. At this corner the displacement fields from three orthogonal plates must be compatible to each other. But, away from the corner, the compatibility conditions involve only two plates, which is similar to the case of folded plate structures. To cover all possible cases, it is assumed that each plate in Fig. 10 is discretized by four elements. From the compatibility point of view, three types of elements are involved and can be identified as follows:

(a) corner element, ABED, in which at least two perpendicular sides (AB and AD) are on junctions;

(b) junction element, BCFE or DEHG, which has one or two parallel sides along junctions;

(c) inside element, EFIH, which does not include any junction.

To keep the model as simple as possible, a unified element is developed in this work, which models each case with a special transformation matrix $[\chi_{II}]$ such that

$$\{\delta_e\} = [\chi_{II}]\{\delta_e^*\} \tag{79}$$

where $\{\delta_e\}$, $\{\delta_e^*\}$ are, respectively, the original and modified displacement vectors and both correspond to the local coordinate system.

In analogy to the folded plate model, the three general rotations θ_x, θ_y and θ_z are employed to replace the bending and in-plane slopes. In addition, the in-plane shear strain, γ_{xy} is introduced as a nodal variables. It is assumed for all cases that

$$\begin{aligned} \theta_x &= w_{,y} \\ \theta_y &= -w_{,x} \\ \gamma_{xy} &= u_{,y} + v_{,x} \end{aligned} \tag{80}$$

However, the definition of θ_z varies with location of the element. For example, if either side 1-2 or 3-4 is on a junction, one uses the definition

$$\theta_z = v_{,x} \tag{81a}$$

or if either side 1-4 or 2-3 is on a junction, one uses

$$\theta_z = -u_{,y} \tag{81b}$$

and otherwise

$$\theta_z = v_{,x} - u_{,y} \tag{81c}$$

It is noted that the three rotations, θ_x, θ_y and θ_z are always defined at the corner nodes, but the shear strain γ_{xy} may be moved away from corner nodes to mid-side nodes. For instance, if side 1-2 is on a junction, γ_{xy1} and γ_{xy2} are moved to nodes 8 and 6, respectively. The reason for doing this is to allow for discontinuity of shear strain across the junction but still remain continuous within each plate. In the earlier work by Tinawi [5], γ_{xy} was constrained to be zero for his flat shell element. This physically imposes a point constraint on the element and numerically leads to a slight increase in element stiffness. In the present work, this assumption is only employed for the box corner (i.e. point A in Fig. 10) and it is enforced through boundary conditions for numerical simplicity. In this case it is theoretically correct.

To further illustrate the model, an example is given in Appendix J with emphasis on the formulation of the transformation matix $[\chi_{II}]$ as well as the modified nodal vector $\{\delta_e^*\}$.

Similar assumptions can be applied to the super beam elements. For a beam in the x-direction the modified nodal vector $\{\bar{\delta}_e^*\}$ is given by

$$\{\bar{\delta}_e^*\}^T = (u_1, v_1, w_1, \theta_{x1}, \theta_{y1}, \theta_{z1}, w_{,xy1}, u_2, v_2, w_2, \theta_{x2},$$
$$\theta_{y2}, \theta_{z2}, w_{,xy2}, u_3, w_3, \theta_{x3}, u_4, u_5) \qquad (82)$$

where $\theta_{xi} = \theta_i$, $\theta_{yi} = -w_{,xi}$, $\theta_{zi} = v_{,xi}$ and $w_{,xyi} = \theta_{,xi}$. For a beam in the y-direction, $\{\bar{\delta}_e^*\}$ takes the form

$$\{\delta_e^*\}^T = (u_1, v_1, w_1, \theta_{x1}, \theta_{y1}, \theta_{z1}, w_{,xy1}, u_2, v_2, w_2, \theta_{x2},$$
$$\theta_{y2}, \theta_{z2}, w_{,xy2}, v_3, w_3, \theta_{y3}, v_4, v_5) \qquad (83)$$

where $\theta_{xi} = w_{,yi}$, $\theta_{yi} = \theta_i$, $\theta_{zi} = -u_{,yi}$ and $w_{,xyi} = \theta_{,yi}$. The transformation matrix $[\bar{\chi}_{II}]$ is provided in Appendix J.

3.2.2 Transformation Matrices

To transform the rectangular box model, described in the previous subsection, from the local system to the global system, the following relation can be written

$$\{\delta_e^*\} = [\Lambda_{II}]\{\bar{\delta}_e\} \qquad (84)$$

where $\{\bar{\delta}_e\}$ is the global nodal vector and, for the inside type of elements, it takes the form,

$$\{\bar{\delta}_e\}^T = (\bar{u}_1, \bar{v}_1, \bar{w}_1, \bar{\theta}_{x1}, \bar{\theta}_{y1}, \bar{\theta}_{z1}, \bar{w}_{,xy1}, \gamma_{xy1}, \bar{u}_2, \bar{v}_2, \bar{w}_2,$$
$$\bar{\theta}_{x2}, \bar{\theta}_{y2}, \bar{\theta}_{z2}, \bar{w}_{,xy2}, \gamma_{xy2}, \bar{u}_3, \bar{v}_3, \bar{w}_3, \bar{\theta}_{x3}, \bar{\theta}_{y3}, \bar{\theta}_{z3},$$
$$\bar{w}_{,xy3}, \gamma_{xy3}, \bar{u}_4, \bar{v}_4, \bar{w}_4, \bar{\theta}_{x4}, \bar{\theta}_{y4}, \bar{\theta}_{z4}, \bar{w}_{,xy4}, \gamma_{xy4},$$
$$u_5, w_5, \theta_{x5}, u_8, u_{11}, v_5, w_6, \theta_{y6}, v_9, v_{12}, u_6, w_7,$$
$$\theta_{x7}, u_9, u_{12}, v_6, w_8, \theta_{y8}, v_8, v_{11}, u_7, v_7, w_9, u_{10},$$
$$v_{10}, u_{13}, v_{13}) \qquad (85)$$

and $[\Lambda_{II}]$ is the transformation matrix and for the inside elements, it is given by

$$[\Lambda_{II}] = \begin{bmatrix} \underset{8x8}{[Q_{II}]} & & & & \\ & \underset{8x8}{[Q_{II}]} & & & \\ & & \underset{8x8}{[Q_{II}]} & & \\ & & & \underset{8x8}{[Q_{II}]} & \\ & & & & \underset{27x27}{[I]} \end{bmatrix} \tag{86}$$

with

$$[Q_{II}] = \begin{bmatrix} \underset{3x3}{[\lambda]} & & \\ & \underset{3x3}{[\lambda]} & \\ & & \underset{2x2}{[I]} \end{bmatrix} \tag{87}$$

In Eq. (87), $[\lambda]$ is the coordinate transformation matrix introduced in Eq. (62), and [I] is the unit matrix.

It is noted that for corner elements or junction elements, the twist variable $w_{,xy}$ must also be properly transformed. In general, $w_{,xy}$ represents a second order tensor and, hence, its transformation usually involves the other two terms $w_{,xx}$ and $w_{,yy}$ which are not included in the present model. However due to the special rectangular shape of the box, the transformation of $w_{,xy}$ can be simplified without involving $w_{,xx}$ and $w_{,yy}$. It can be shown that the sign of $w_{,xy}$ depends on the location of the junction. Table 6 summarizes the sign convention for different locations. It may be noted that when two perpendicular sides (e.g. 1-2 and 2-3) are both in the junction, a corner is formed. In this case it is required by kinematic conditions that $\bar{w}_{,xy} = 0$ for node 2. Similar to the shear strain γ_{xy}, the elimination of $w_{,xy}$ at the box corner is realized via boundary condition specifications.

Finally, the total transformation matrix $[T_{pII}]$ is obtained using Eqs. (79) and (84),

$$\{\delta_e\} = [T_{pII}]\{\bar{\delta}_e\} \tag{88}$$

where

$$[T_{pII}] = [\chi_{II}][\Lambda_{II}] \tag{89}$$

The transformation of the mass and stiffness matrices and the load vector are now carried out using Eq. (75) in which $[T_{pI}]$ is replaced by $[T_{pII}]$.

For the super beam elements the total transformation matrix is given by

$$[T_{bII}] = [\bar{\chi}_{II}][\bar{\Lambda}_{II}] \tag{90}$$

where $[\bar{\chi}_{II}]$ and $[\bar{\Lambda}_{II}]$ are given in Appendix J.

4. NUMERICAL VERIFICATIONS

Results presented in this section are obtained from a variety of examples which were chosen to verify the proposed super finite element formulation and to illustrate the accuracy and convergence of the super elements in various applications. The problems analyzed are categorized into three groups. The first group deals solely with static responses, while the second is concerned with free vibrations. The last group presents the results obtained from transient analyses. In each group, the results are presented in such a manner that simple structures such as beams and plates are considered first and then are followed by more complex structures of box type. In order to examine the accuracy and efficiency of the formulation, the results obtained are compared with experimental data or other available solutions. For the cases where both experimental and numerical results are not available, a convergence study is carried out using refined grids. In general, good agreement is obtained for most of the problems considered and the present formulation is found to be accurate and economical for preliminary engineering design.

4.1 Static Analysis Results

Since the objective of this work is to develop a numerical model for blast loaded stiffened box structures, the uniformly distributed load is of primary interest here and has been assumed for most of the examples considered below. This does not imply that the other types of loading cannot be handled by the model. On the contrary, the model developed here is quite versatile. The effects of geometric and material nonlinearities are investigated in some of the examples. For linear analysis the total load is applied in one load step while for nonlinear analysis, an incremental approach is adopted.

4.1.1 Beams

(1) Cantilever Beams

The first example considered is the cantilever beam shown in Figure 11. This example was chosen to investigate whether lateral bending effects are correctly simulated by the in-plane displacements of the super plate element. The material properties are $E = 30000$ ksi and $\nu = 0.25$. The beam is subjected to a parabolically distributed shear force at its free end and the total applied load is 40 kips. The beam is idealized into one, two and four elements, respectively. The two cases of boundary conditions are applied as follows: Case 1 - all three nodes at the support are completely fixed (Fig. 11(b)); and, Case 2 - only the mid-side node is fixed while the other two nodes are constrained only in the axial direction (Fig. 11(c)).

A linear elastic analysis is carried out and the results are presented in Tables 7 and 8. In Table 7, the present predictions for the tip deflection of the free end are compared with the known exact solution and other numerical predictions [5]. As expected, the predictions obtained from the first set of boundary conditions are stiffer than that from the second set. The convergence of the results in both cases is quite fast. Some of the stress calculations are shown in Table 8 for the four element idealization. As compared to the exact solution the largest error in the stress calculations is less than 2.2%.

(2) Rectangular Beam with Simple Supports

This simple beam problem is chosen here to verify the new beam element formulation. The beam is simply supported at both ends and has the following dimensions and material properties:

Length, a = 500 mm

Width, b = 10 mm

Depth, h = 10 mm

Young's modulus, E = 220,000 N/mm^2

A single beam element is used to represent the beam. A linear elastic analysis is carried out for an applied load of 10 kN/m. The beam central deflection, strain energy and maximum normal stress are presented in Table 9 together with those obtained by the finite strip [8] and exact [10] methods. The present prediction is in excellent agreement with both the finite strip and exact solutions, and it underestimates the exact strain energy by only 0.14% and overestimates the exact maximum normal stress by 2.73%.

4.1.2 Flat Plates

(1) Square Plate with Simply Supported Edges

This example, previously investigated by a number of researchers [3,8], is used here to evaluate the performance of the new plate element. The square plate is assumed to be simply supported all round and has the following dimensions and material properties:

Dimensions, a x b x h = 100 mm x 100 mm x 1 mm

Young's modulus, E = 205,000 N/mm^2

Poisson's ratio, ν = 0.3

The plate is subjected to a uniform pressure load. For the initial analysis, the plate is modelled by one plate element with all the in-plane motions being constrained on the boundaries. The linear elastic response results for the structure under a pressure load of 0.1 N/mm^2 are presented in Table 10.

It can be seen that the present results are exactly the same as predicted by Koko et al. [3] and are in excellent agreement with the finite strip solution [8]. As compared with the exact solution [10], all the three numerical calculations overestimate the central deflection but underestimate the strain energy. However, the error is very small.

Large deflection elastic and elastic-plastic central displacement responses are tabulated in Table 11. For the elastic-plastic calculation, it is assumed that $E_T = 1025$ N/mm², and $\sigma_0 = 210$ N/mm². Since the in-plane motions have been totally constrained on the boundaries, the present element has the same displacement interpolation functions as Koko et al. [3] in this case. One would expect then that the results obtained from the two formulations would be identical, which is exactly the case shown by Table 11.

To test the performance of the new element in the nonlinear analysis, the in-plane constraints have to be relaxed and in this case a 2x2 mesh has been used to discretize the plate. The large deflection elastic analysis was repeated and the results are presented in Table 12. It is seen that the present element predicts a slightly higher strain energy than that by Koko et al. [3] but a slightly lower central displacement. From the strain energy convergence point of view, an improved solution has been obtained by the present element.

(2) Square Plate with Clamped Edges

The dimensions and material properties are the same as the simply supported square plate discussed above. The plate is now clamped all round and is discretized by one, two and four elements, respectively. The linear elastic central displacement and strain energy responses at a pressure load of 0.1 N/mm² are presented in Table 13 and compared with the finite strip [8] and exact solutions. It is seen that the one element solution is very close to the one-mode finite strip solution, while the two and four element solutions gradually converge towards the exact solution.

(3) Clamped 2-Bay Stiffened Plate

The configuration and material properties for the two-bay stiffened plate example are provided in Fig. 12. All edges are assumed to be clamped, and one half of the structure is modelled by one plate element and one beam element using symmetry. The linear elastic response results for the structure under a pressure load of 0.001 N/mm^2 are listed in Table 14 along with the finite strip predictions [8]. The present analysis overpredicts the panel central displacement by 2.2 percent and underpredicts the strain energy by 3.7 percent in comparison with the one-mode finite strip analysis.

(4) Clamped DRES1B Stiffened Panel

This example is selected to verify the present formulation for two-way stifffened panel structures. Figure 13 provides details of the example. The structure is completely clamped all round. To simplify the analysis only the section ABCD is modelled by one plate element and two beam elements. Symmetry conditions are assumed along the BC, CD and DA boundaries, respectively. This simplified representation implies that the panel is effectively infinitely long with identically repeated bays and stiffeners. A comparison study has been carried out in [3] for the clamped DRES stiffened panel using the simplified as well as the complete panel representation. It was found that the results obtained from the two different representations are very close to each other for elastic analysis but significantly different for nonlinear elastic-plastic analysis.

The linear elastic response of the panel subjected to a pressure load of 50 psi is presented in Table 15 together with the Koko et al. and ADINA predictions. The present model yields the same deflections as Koko et al. as expected. The super element results compare very well with those obtained from the ADINA analysis.

The nonlinear elastic response under the same load is provided in Table 16 along with the Koko et al. and ADINA predictions. Once again the present analysis repeats Koko et al.'s prediction, and the super element solutions are stiffer than the ADINA solution for which a finer mesh was used.

4.1.3 Tube Structures

(1) Unstiffened Cubic Tube

Figure 14 shows details of the configuration of this example. The tube has a cubic shape and is made up of four identical square plates. The material properties are $E = 205,000$ N/mm^2 and $\nu = 0.3$. The structure is analysed using three different meshes. The first is a 1x1 coarse grid with one plate element representing each square plate of the tube, and the two subsequent meshes are finer, namely, 2x2 and 4x4 for each plate. For the finer grids, 2x2 and 4x4, only a one-eighth portion, ABCDEF, of the structure is modelled, respectively, by two and eight elements using symmetry. Both internal and external pressure loads are simulated.

A linear elastic analysis is carried out first at a pressure load of 0.1 N/mm^2. The panel centre and free edge mid-point deflections as well as strain energy are presented in Table 17 for three different models using three different grids. Here, FPM denotes the Flat Plate Model, RBM stands for the Rectangular Box Model and SBM is a Simplified Box Model in which all the shear strain nodal variables γ_{xy} in RBM are assumed to be zero as suggested in [5]. It is observed that for each grid used the displacement predictions from the three models are essentially the same but the strain energy calculations do show a slight difference. For the coarser grids, 1x1 and 2x2, FPM and RBM end up with the same numerical representation of the structure so that the same amount of strain energy is predicted. However, for the finer grid, 4x4, RBM predicts a slightly lower strain energy than FPM as expected. Although an additional constraint is introduced in SBM, it seems that the strain energy is not very much different from the other two models. This is because the shear strains in this case are very small in comparison with the normal strains. When the shear strains become larger for non-uniform loads the predictions by SBM may be much stiffer than those by the other two models.

It may be noted that the linear elastic analysis above neglects the effect of geometric stiffness caused by the membrane stresses, which is obviously not physically correct. As a result, the predicted structural response is independent of the direction of the applied pressure. To properly account for this effect, the large deflection elastic analysis is performed using the rectangular box model, RBM. The strain energy, in-plane and bending displacements for the 1x1 grid are plotted in Figs. 15, 16 and 17, respectively, along with theoretical calculations based on a one-dimensional assumption. See Appendix K for details. In Fig. 15, the nonlinear elastic solutions are also compared with the linear elastic calculations. As can be seen, the inclusion of the geometric stiffness matrix [Ω] makes the structural response sensitive to the direction of the applied loads. For internal pressure, the tensile membrane stresses stiffen up the structure and result in a reduction in the total strain energy with respect to the linear elastic case. Conversely, external pressure produces compressive membrane stresses and thus softens the structure. As a consequence, more strain energy is generated at the same load level. When the external pressure is further increased, the structure is further softened and eventually it will fail in buckling. It has been found that the buckling load predicted by the 1x1 grid is $q_{cr} = 0.372$ N/mm², (as evidenced by the tangent stiffness matrix becoming singular) which is only slightly higher than the theoretical calculation, 0.371 N/mm². It is also seen from Fig. 15 that the super finite element results are in excellent agreement with the theoretical solutions.

The in-plane displacements at the free edge corner (point C) and junction mid-point (point F) are plotted in Fig. 16 for both internal and external pressure loads. It is observed that the in-plane displacements at both locations are almost the same, which implies that the in-plane displacement field in the transverse direction is quite uniform and the one-dimensional assumption for the theoretical calculation is a fairly good approximation. The bending displacement at the panel center (point A) is compared to that at the free edge mid-point (point B)in Fig. 17. Again, negligible differences are observed. In comparison with the theoretical calculations, the discrepancies for both the in-plane and bending displacements are very small.

Finally, the results obtained using the finer grids, 2x2 and 4x4, are compared in Figs. 18 and 19. It is seen that not much improvement in the displacement and strain energy calculations is observed. Therefore, it can be concluded that the coarse grid is quite adequate for modelling the cubic tube structure.

(2) Stiffened Cubic Tube

The cubic tube structure above is now reinforced by two-way beam stiffeners to enhance its load carrying capacity. As depicted by Fig. 20, two orthogonal beam stiffeners are placed along the centerlines of each square plate. Each stiffener has a rectangular cross-section of $b \times h = 3 \times 6$ mm. To investigate the sensitivity of the structural response to the stiffener locations, both interior and exterior stiffeners are simulated, respectively. Only the internal pressure loading is considered for this example. The structure is discretized by 2x2 and 4x4 grids, respectively. Similar to the above example, using symmetry, one eighth of the structure is discretized by two plate and four beam elements for the 2x2 grid, and eight plate and eight beam elements for the 4x4 grid.

The nonlinear elastic analysis results are presented in Figs. 21 and 22, respectively, for the interior and exterior beams. It is seen that the general trends for both cases are quite similar. As compared to the unstiffened tube structure, the beam stiffeners make the structural response no longer like a one-dimensional problem. Instead, the bending displacement at the beam crossing point C is only about 44% of that at the beam free end point A for the interior stiffeners and about 48% for the exterior stiffeners. As expected, the predictions using the 4x4 grid are larger than those by the 2x2 grid. It seems that the location of stiffeners has little effect on the response calculations for the present example.

(3) Cubic Container

Figure 23 shows a cubic liquid container with rigid corners. The container has dimensions of 610 mm x 610 mm x 610 mm and all four panels are assumed to be fixed at the bottom to a rigid base. The thickness of the plates is 9.525 mm. The modulus of elasticity is 2715 MPa, and Poisson's ratio 0.375. The container is internally loaded by hydrostatic pressure from water. This example has been experimentally investigated by Davies [11] and analytically studied by Davies [11] and Canisius [12]. An approximate linear solution was obtained by Davies using the Kantorovich method. Based on the finite strip method, both linear and nonlinear elastic solutions were obtained by Canisius. To illustrate the capability of the present formulation the example is re-analyzed here for both linear and nonlinear responses using the rectangular box model.

The three grids used to discretize the structure are 1x1, 2x2 and 4x4, all per panel. Using symmetry, only one quarter of the structure is analyzed for the finer grids of 2x2 and 4x4. The predicted strain energy and lateral displacements at the center (point A) and the top-center (point B) of the panels are presented in Table 18 along with the finite strip predictions [12] and the experimental results [11]. It is seen that the strain energy obtained from the three grids seems to converge monotonically but not the displacements. It is also noted that the nonlinear results are only slightly less than the linear results. This is because the plates are quite thick, so that nonlinear effects are not appreciable under the hydrostatic pressure. The nonlinear effects can be expected to be more important for thinner plates. Overall, as compared to the experimental results, the present predictions except for the linear analysis using the 1x1 grid are all on the slightly stiff side but very close.

In order to further investigate the importance of nonlinear effects, more simulations are carried out considering thicknesses of 8 mm and 6 mm for the wall plates. Both containers have the same internal dimensions as above, and again are completely full of water. The finest 4x4 grid is used in all cases. The displacements obtained from the present investigation are provided in Table 19 together with the corresponding finite strip results [12]. As can be seen, the present displacement predictions are consistently lower than those of the finite strip method with the discrepancies within the range of 2.3% to 7.7%. The higher displacements predicted by the finite strip method may be due to the fact that the fixed corner constraints were only satisfied by a penalty approach in the finite strip model. In any case, the differences are within acceptable limits.

4.1.4 Box Structures

(1) Unstiffened Cubic Box

Details of this example are given in Fig. 24. The material properties are $E = 205{,}000\ N/mm^2$, $E_T = 1{,}025\ N/m^2$, $\sigma_0 = 210\ N/mm^2$ and $\nu = 0.3$. Three discretizations are used to represent the structure. In the 1x1 grid discretization, six plate elements are employed to model the complete structure. Using symmetry, only one eighth of the box is analyzed in the 2x2 and 4x4 grid representations using eight and twelve elements, respectively. Once again, both internal and external pressure loads are considered.

First, a linear elastic analysis is performed at an applied load of 0.1 N/mm^2. The results from the three grids are presented in Table 20 in terms of the panel center displacement and the total strain energy. It can be seen that the solutions converge very rapidly with grid refinement.

A large deflection elastic analysis is then carried out and the results obtained are plotted in Figs. 25 to 27. The total strain energy results obtained from the three grids are compared in Fig. 25. The general trends are quite similar for internal and external pressure loads. Again the convergence of the strain energy is quite good. It is interesting to note that the differences in strain energy from the three grids increases with load in a parabolic fashion. Figures 26 and 27 show the in-plane displacement at the junction mid-span (point B or C) and the bending displacement at the panel center (point A), respectively. It is seen from Fig. 26 that the in-plane displacement is not very sensitive to grid refinement. The external pressure seems to generate more membrane deformation than the internal pressure at the same load level. However, the bending displacement does increase with grid refinement as shown in Fig. 27. At low load levels, the pressure load applied internally or externally does not affect the response very much. But, as the load increases the response under external pressure tends to be significantly larger than that under internal pressure. It is also noted that the convergence of the results in both loading cases is quite satisfactory.

Finally, the large deflection, elastic-plastic responses are calculated from the 4x4 grid. The panel center displacements obtained, respectively, from the internal and external loading cases are presented in Fig. 28. For comparison purposes, the results from the large deflection elastic analysis are also plotted in the same figure. As can be seen, material yielding leads to a significant increase in the displacement. For example, the maximum displacement is increased by about 90% for the internal loading case and 250% for the external loading case.

The bending displacement profiles along CD and AB are plotted in Figs. 29 and 30 at three load levels for the internal and external pressure, respectively. A very similar trend is obtained for both loading cases except that the displacement along AB is inward for the external load but outward for the internal load. At the low load level of 0.1 N/mm^2 when yielding has just taken place, the displacements along CD are still very small. Then, at the higher load level of 0.3 N/mm² when a considerable amount of material has yielded, the displacements along both CD and AB increase dramatically. Finally, at the load level of 0.5 N/mm², the plastic deformation accumulated in the structure leads to the maximum displacements.

(2) Stiffened Cubic Box

The stiffened cubic box has the same dimensions and material properties as the above example except that each panel of the structure is reinforced by two rectangular beams along the panel center lines in both directions, as illustrated by Fig. 31. The dimensions of the beam cross-sections are b=3mm and h=6mm. Both interior and exterior beams are considered, respectively, in this example. The box is assumed to be subjected to an internal pressure load. Two grids are used to idealize the structure. Again, using symmetry, one eighth of the structure is modelled by three plate elements and six beam elements for the 2x2 grid, and twelve plate and twelve beam elements for the 4x4 grid.

Some of the linear elastic response results at a load of 0.1 N/mm² are presented in Table 21. As a reference, a simplified analysis is carried out considering a single clamped panel isolated from the box and its results are also listed in Table 21. It is seen that the displacements from the simplified analysis are slightly lower than those from the full structure analysis as expected. This small exercise, in fact, helps to verify that the transformation matrices introduced in the rectangular box model have been correctly implemented.

The large deflection elastic and elastic-plastic responses are plotted in Figs. 32 and 33, respectively, for both interior and exterior stiffeners.

Several calculations are carried out for the elastic-plastic case to ensure that the load step is adequate. The results reported here are from the calculations using a load step of 0.05 N/mm². It is observed from Fig. 32 that the elastic-plastic response curves obtained from the 4x4 grid display some nonsmoothness at the higher load levels. One possible explanation for this is that the load step used is not small enough causing numerical errors in the tangent stiffness calculations. To further investigate this hypothesis, the analysis is repeated using a very fine load step of 0.025 N/mm². It is found that the same phenomenon occurs at almost the same load levels even with this smaller load step. It is interesting to note that this phenomenon only occurred for the internal stiffener case for which the stiffeners were in compression. Other than this phenomenon, the general trends shown in Figs. 32 and 33 are quite similar to those observed in the stiffened plate analysis [3]. It is also noted that the refined 4x4 grid shows very little improvement for the nonlinear elastic response but does give significant increase in the nonlinear elastic-plastic displacements. This is presumably because the finer grid with its increased number of Gauss points gives a better representation of the yielding regions.

For the elastic-plastic case, the displacement profiles at three load levels are plotted along BE and AF in Figs. 34 and 35, respectively, for the interior stiffened and exterior stiffened boxes. In general, the displacement distributions for both boxes are quite similar. It can be seen from both figures that at the low load of 0.6 N/mm² when yielding has just started in the plates, the displacements along BE are still larger than those along AF for most of the considered ranges. Later, at higher load levels when considerable yielding has taken place in both the plates and stiffeners, the displacements along AF have reached the magnitude of those along BE near the box corners and have exceeded those along BE in the central region.

4.2 Vibration Analysis Results

Before presenting the transient applications of the super element models, the accuracy of the consistent mass matrices developed in Section 2 is tested in the context of free vibration analysis. In what follows only linear undamped vibrations are considered and various types of structures have been analyzed.

4.2.1 Flat Plates

(1) Square Plates with Various Edge Constraints

This is a classical problem for which exact or approximate solutions are available in the literature [13]. It is re-analyzed here to assess the accuracy of the super element formulation against known solutions.

In the literature the natural frequencies of a square plate are usually expressed in terms of the non-dimensional parameter λ given by

$$\lambda = \frac{\rho h \omega^2 a^4}{D \pi^4} \qquad (91)$$

where $D = Eh^3/12(1-\nu^2)$ is the plate bending rigidity, h is the plate thickness, ρ the mass density, ω the frequency in rad/sec, and a the side length of the plate. In the present calculations, only one plate element is used and the following dimensions and material constants are used,

Dimensions, $a \times b \times h$ = 100 mm x 100 mm x 1 mm

Young's modulus, E = 205,000 N/mm^2

Poisson's ratio, $\nu = 0.3$

Mass density, $\rho = 0.79\text{x}10^4$ kg/m^3

The first two non-dimensional frequencies for the various combinations of edge constraints are presented in Table 22 along with the corresponding known solutions [13]. The edge constraints are described in abbreviation by four letters with C, S and F standing for a clamped, simply supported and free edge, respectively. The sequence of the letters starts from the left side and progresses clockwise. The present calculations repeated the earlier results by Koko et al. [14] and have shown that excellent agreement is obtained for the fundamental frequency in all eight cases considered.

(2) 3-Bay Continuous Plate

The configuration of this plate is shown in Fig. 36. This example has been investigated by a number of researchers [14,15]. The long edges AB and DC are both simply supported and the other two short edges AD and BC are assumed to be both either simply supported or clamped. The two interior supports are line supports along which no vertical displacement w is allowed. In the present calculations three plate elements are employed to discretize the plate. In Table 23 the first three frequencies obtained are compared with other available solutions in terms of the non-dimensional parameter λ given by

$$\lambda = \omega \ell^2 \left(\frac{\rho h}{D}\right)^{1/2} \qquad (92)$$

In the above equation ω is the natural frequency in rad/sec, D is the plate bending rigidity, h the plate thickness, ρ the mass density, and ℓ is the length parameter defined in Fig. 36. Once again, the earlier predictions by Koko et al. [14] have been repeated here. Furthermore, the super element calculations are in good agreement with the finite strip calculations [15] for all the frequencies presented in Table 23.

(3) 2x4 Bay Stiffened Plate with Clamped Edges

The last example for the flat plate vibration analysis is depicted in Fig. 37. The material constants used in this example are $E = 71 \times 10^9$ N/m², $\nu = 0.3$ and $\rho = 2700$ kg/m³. Using symmetry, only one quarter of the plate is modelled by two plate and four beam elements as shown in Fig. 37. The first six natural frequencies are listed in Table 24 together with the earlier super element predictions by Koko et al. [14]. The symmetry conditions applied along the centre lines in the x and y directions are denoted by the first and second letters, respectively - A, for anti-symmetric, and S, for symmetric - in the second column. Some of the frequencies obtained from the present calculations are slightly higher than the earlier predictions presumably because of the strict C^1 continuity now enforced for the lateral bending displacement functions. However, the differences are quite small.

4.2.2 Box Structures

(1) Cubic Tube Structure

The dimensions and material properties for this example are the same as those used for the static analysis of Section 4.1.3. In addition, the mass density is assumed to be 0.79×10^4 kg/m³. The three grid discretizations adopted in the static analysis are used here again. In the 1x1 grid discretization, the complete structure is modelled by four plate elements.

However, for the 2x2 and 4x4 grids, only one eighth of structure needs to be considered due to symmetry. For the later cases, six combinations of symmetry conditions are applied to the three symmetry planes so as to capture all possible vibration modes. The first twenty natural frequencies obtained from the present analysis are displayed in Table 25. It is noted that for the 1x1 grid the vibration modes can be identified only up to the seventh due to the limited number of variables available in the eigenvectors. It is seen that the frequencies converge from above with grid refinement as expected.

In order to get an assessment of the accuracy, some approximate solutions have been obtained using the weighted average approach and are compared with those by the super element method in Table 26. By weighted average approach, the natural frequencies of each individual panel are first calculated based on boundary conditions corresponding to a particular mode shape predicted in the super element calculations and after summing them up and dividing by the total number of panels the approximate frequency for the complete structure is obtained. For example, the mode shape associated with the fundamental frequency of the cubic tube shown in Fig. 38 indicates that each panel vibrates just like a square plate simply supported along two opposite edges. Assuming the boundary conditions of SFSF, the estimated frequency for both the individual panel and the complete structure is obtained and in this case it was 236 Hz. As can be seen from Table 26, the results from the super element calculations are in excellent agreement with those of the approximate solutions for the cases considered.

(2) Cubic Box Structure

The same unstiffened box structure used as the example for the static applications in Section 4.1.4 is considered here again for the free vibration analysis. Three grid idealizations are employed as before. For the 2x2 and 4x4 grids one eighth of the structure is analyzed using symmetry. In order to simulate all possible modes four sets of boundary conditions have been applied to the three symmetry planes, respectively. The first twenty natural frequencies obtained are presented in Table 27. Note that for the 1x1 grid, only the first three vibration modes can be properly identified. Similarly, the approximate solutions for the first three frequencies are obtained using the weighted averaged approach as discussed before, and they are compared with the corresponding super element predictions in Table 28. It is seen that the super element predictions are very close to the approximate solutions. It can be concluded that the present mass matrix formulation is correct for the free vibration of box structures.

4.3 Transient Analysis Results

In this section, the super element model is further investigated in transient applications. First, two flat plate examples are presented to test the basic formulation. Due to lack of comparison results available in the literature only two simple box structures are considered here for illustrative purposes.

4.3.1 Flat Plates

(1) Square Plate with Simply Supported Edges

The dimensions and material properties of the square plate are the same as those used for the static analysis in Section 4.1.2. In addition the mass density is assumed to be $7.9\text{x}10^3$ kg/m^3. All four edges of the plate are simply supported. The plate is subjected to a step load of $67.2\text{x}10^{-3}$ MPa and is modelled by one plate element. Both linear elastic and large-deflection elastic analyses are carried out and a time step of 0.103 msec is used for both cases. Figure 39 displays the transient response of the central deflection predicted by the present as well as the earlier super element models [16]. It is seen that the results obtained by the two models are identical as expected.

(2) Clamped 2-Bay Stiffened Plate

This example has the same configuration and material constants as given in Fig. 12. In addition, the following material properties are used: $\rho = 2670$ kg/m³, $E_T = 344.5$ MPa and $\sigma_0 = 284$ MPa. The plate boundaries are assumed to be completely clamped and the structure is subjected to a blast-type of load described by the exponential variation $q(t) = q_m(\frac{1-t}{\tau})\exp(\frac{-\beta t}{\tau})$ with $q_m = 0.6$ MPa, $\tau = 1$ msec and $\beta = 0.28$. Due to symmetry, only one half of the structure is modelled by one plate and one beam element. Using a time step of 0.025 msec a large-deflection, elastic-plastic analysis is performed. The half panel center and stiffener midpoint displacement responses are plotted in Fig. 40. The present predictions are the same as those by the earlier model [16].

4.3.2 Box Structures

(1) Cubic Tube Structure

The simple tube structure is used here again for the transient analysis. The dimensions and material constants are the same as before. The structure is subjected to a step pressure load of 0.3 N/mm² and a 1x1 grid is used to discretize the structure. For linear elastic analysis a time step of 0.09 msec is used while a time step of 0.045 msec is employed for nonlinear analysis.

The linear and nonlinear elastic responses are shown in Figs. 41 and 42, respectively, for an internal and an external pressure load. As can be seen, the linear transient responses for the internal and external pressures are exactly the same with the largest displacement occurring at the free edge point A. For the nonlinear case the displacements at both the free edge and the panel center are reduced for the internal pressure loading, while conversely they are increased for external pressure load. This, once again, shows the effect of the membrane stresses due to the internal and external pressure, respectively.

(2) Cubic Box Structure

The second example considered here is the cubic box structure as shown in Fig. 24 and it is the same as for the static analysis. The other material properties used are $\rho = 7.9\text{x}10^3$ kg/m³, $E_T = 1025$ N/mm² and $\sigma_0 = 210$ N/mm². The structure is subjected to a step pressure load of 0.3 N/mm². For comparison purposes, both internal and external pressure loadings are considered. Time steps of 0.05 and 0.025 msec are used for the linear elastic and nonlinear analyses, respectively.

The linear and nonlinear elastic transient responses from the 1x1 grid solutions are presented in Fig. 43. It is observed that for both linear and nonlinear analyses, the panel center displacement for internal pressure loading is similar to that for external pressure loading. The inclusion of nonlinear effects has reduced the displacement by about 47% and 44%, respectively, for the internal and external loading cases.

For the large-deflection, elastic-plastic analysis, the results from the 1x1 grid solutions are compared with those from the 4x4 grid solutions in

Fig 44. For the 1x1 grid idealization, the panel center displacements under internal and external pressure loads are almost the same. However, when the finer 4x4 grid is used, the permanent displacement generated under external pressure load is larger than that under internal pressure load. For both cases, the permanent displacement predicted by the 4x4 grid is higher than that by the 1x1 grid. From a qualitative point of view, the results may be considered to be satisfactory.

5. CONCLUSIONS

An efficient nonlinear analysis capability has been developed for stiffened box structures. The model is based on a super finite element formulation and is capable of simulating the large-deflection, elastic-plastic response of various structures subjected to static and dynamic loads. The present work was directly motivated by the satisfactory performance of the super finite elements in nonlinear analysis of stiffened plates [3,14,16]. The objective of this work was to extend their applicability to more complex and larger structures such as stiffened box structures.

The new developments made in this work include modification of the displacement functions for both plate and beam elements to provide complete C^1 continuity and compatibility on the interfaces between various elements and formulation of appropriate transformation matrices for modelling of three dimensional structures, e.g. folded plates and rectangular boxes.

The new formulation has been applied to the static, vibration and transient analysis of various structures such as flat plates, folded plates and rectangular boxes. Both isotropic and beam-stiffened structures were considered and the results obtained were compared with experimental results or other available solutions. In the cases where neither experimental nor numerical results were available, convergence studies were carried out using refined grids. Good approximations were obtained in most cases even with a single super element per bay or span. It has been shown that the super element formulation developed here can provide reasonable solutions to nonlinear problems of stiffened box structures.

6. ACKNOWLEDGEMENTS

The research work presented in this report was financially supported by the Canadian National Defence Department through a contract from the Defence Research Establishment Suffield, Alberta, Canada.

7. REFERENCES

[1] N.W. Murray, Introduction to the Theory of Thin-Walled Structures, Clarendon Press, Oxford, U.K., 1984.

[2] J.W. Bull, Finite Element Applications to Thin-Walled Structures, Elsevier Applied Science, London, U.K., 1990.,

[3] T.S. Koko and M.D. Olson, "Nonlinear Analysis of Stiffened Plates Using Super Elements", International Journal for Numerical Methods in Engineering, Vol. 31, pp. 319-343, 1991.

[4] F.K. Bogner, F.L. Fox and L.A. Schmit, "The Generation of Compatible Stiffness and Mass Matrices by the Use of Interpolation Formulas", Proceedings of the Conference on Matrix Methods in Structural Mechanics, Wright-Patterson Air Force Base/Air Force Flight Dynamics Lab, Tr-66-80, pp. 397-443, 1966.

[5] R.A. Tinawi, Behaviour of Orthotropic Bridge Decks, Ph.D. Thesis, Dept. of Civil Engineering and Applied Mechanics, McGill University, Montreal, Canada, 1972.

[6] R. Hill, The Mathematical Theory of Plasticity, Oxford University Press, Oxford, U.K., 1950.

[7] K.J. Bathe and E.L. Wilson, Numerical Method in Finite Element Analysis, Prentice-Hall, Inc., Englewood Cliffs, N.J., U.S.A., 1976.

[8] S.B.S. Abayakoon, M.D. Olson and D.L. Anderson, "Large Deflection Elastic-Plastic Analysis of Plate Structues by the Finite Strip Method", International Journal for Numerical Methods in Engineering, Vol. 28, pp. 331-358, 1989.

[9] J. Jiang, M.D. Olson and D.L. Anderson, "Nonlinear Transient Analysis of Cylindrical Shell Structures by the Finite Strip Method", Dept. of Civil Engineering, UBC, Struc. Res. Series Report No. 35, 87 pages, 1990.

[10] S. Timoshenko and S. Woinowsky-Krieger, Theory of Plates and Shells, McGraw Hill, New York, 1959.

[11] J.D. Davies, "The Influence of Support Conditions on the Behaviour of Square Concrete Tanks", Magazine of Concrete Research, Vol. 16, No. 48, pp. 153-165, 1964.

[12] T.D.G. Canisius, A Mindlin Finite Strip for the Analysis of Rectangular Containers and Continuous Plates with Elastically Restrained Supports, Ph.D. Thesis, Department of Civil Engineering, University of British Columbia, Vancouver, Canada, 1990.

[13] S. Durvasula, R.N. Burbure and S. Srinivasan, "Natural Frequencies of Vibration of Isotropic Flat Plates - I", Report No. AE190S, Dept. of Aeronautical Eng., Indian Institute of Science, Bangalore-12, 1968.

[14] T.S. Koko and M.D. Olson, "Vibration Analysis of Stiffened Plates by Super Elements", J. Sound & Vibration (in press).

[15] C.I. Wu and Y.K. Cheung, "Frequency Analysis of Rectangular Plates Continuous in One or Two Directions", Earthquake Engineering and Structural Dynamics, Vol. 3, pp. 3-14, 1974.

[16] T.S. Koko and M.D. Olson, "The Response of Air-Blast Loaded Stiffened Plates", Comp. Methods Ap. Mechs. and Eng. (in press).

Table 1: Nodal Degrees of Freedom for Plate Element ($\{\delta_e\}$)

Node No.	Degrees of Freedom
1	$u_1, v_1, w_1, u_{,y1}, v_{,x1}, w_{,x1}, w_{,y1}, w_{,xy1}$
2	$u_2, v_2, w_2, u_{,y2}, v_{,x2}, w_{,x2}, w_{,y2}, w_{,xy2}$
3	$u_3, v_3, w_3, u_{,y3}, v_{,x3}, w_{,x3}, w_{,y3}, w_{,xy3},$
4	$u_4, v_4, w_4, u_{,y4}, v_{,x4}, w_{,x4}, w_{,y4}, w_{,xy4}$
5	$u_5, w_5, w_{,y5}, u_8, u_{11},$
6	$v_5, w_6, w_{,x6}, v_9, v_{12},$
7	$u_6, w_7, w_{,y7}, u_9, u_{12},$
8	$v_6, w_8, w_{,x8}, v_8, v_{11},$
9	$u_7, v_7, w_9, u_{10}, v_{10}, u_{13}, v_{13}$

Table 2: Nodal Degrees of Freedom for Beam Element ($\{\bar{\delta}_e\}$)

Direction	Node No.	Degrees of Freedom
x	1	$u_1, v_1, w_1, v_{,x1}, w_{,x1}, \theta_1, \theta_{,x1}$
	2	$u_2, v_2, w_2, v_{,x2}, w_{,x2}, \theta_2, \theta_{,x2}$
	3	$u_3, w_3, \theta_3, u_4, u_5$
y	1	$v_1, u_1, w_1, u_{,y1}, w_{,y1}, \theta_1, \theta_{,y1}$
	2	$v_2, u_2, w_2, u_{,y2}, w_{,y2}, \theta_2, \theta_{,y2}$
	3	$v_3, w_3, \theta_3, v_4, v_5$

Table 3: Number of Gauss Integration Points

Plate Element			Beam Element		
Direction	Elastic	Elastoplastic	Direction	Elastic	Elastoplastic
x y z	5 5 2	5 5 4	Axial Thickness	5 2*	5 4*

Table 4: Nodal Degrees of Freedom for Plate Element in Folded Plate Model ($\{\delta_e^*\}$)

Node No.	Degrees of Freedom
1	$u_1, v_1, w_1, \theta_{x1}, \theta_{y1}, \theta_{z1}, w_{,xy1}$
2	$u_2, v_2, w_2, \theta_{x2}, \theta_{y2}, \theta_{z2}, w_{,xy2}$
3	$u_3, v_3, w_3, \theta_{x3}, \theta_{y3}, \theta_{z3}, w_{,xy3}$
4	$u_4, v_4, w_4, \theta_{x4}, \theta_{y4}, \theta_{z4}, w_{,xy4}$
5	$u_5, w_5, \theta_{x5}, u_8, u_{11}, v_{,x1}, v_{,x2}$
6	$v_5, w_6, \theta_{y6}, v_9, v_{12}$
7	$u_6, w_7, \theta_{x7}, u_9, u_{12}, v_{,x4}, v_{,x3}$
8	$v_6, w_8, \theta_{y8}, v_8, v_{11}$
9	$u_7, v_7, w_9, u_{10}, v_{10}, u_{13}, v_{13}$

Table 5: Nodal Degrees of Freedom for Beam Element in Folded Plate Model ($\{\delta_e^*\}$)

Direction	Node No.	Degrees of Freedom
x	1	u_1, v_1, w_1, θ_{x1}, θ_{y1}, $w_{,xy1}$
	2	u_2, v_2, w_2, θ_{x2}, θ_{y2}, $w_{,xy2}$
	3	u_3, w_3, θ_{x3}, u_4, u_5
y	1	u_1, v_1, w_1, θ_{x1}, θ_{y1}, θ_{z1}, $w_{,xy1}$
	2	u_2, v_2, w_2, θ_{x2}, θ_{y2}, $u_{,y2}$, $w_{,xy2}$
	3	v_3, w_3, θ_{y3}, v_4, v_5

Table 6: Sign Convention for Global Twist, $\bar{w}_{,xy_i}$

Junction Nodes	Global Twist $\bar{w}_{,xy_i}$
1, 2	$w_{,xy1}$, $w_{,xy2}$
2, 3	$-w_{,xy2}$, $-w_{,xy_3}$
3, 4	$w_{,xy3}$, $w_{,xy4}$
1, 4	$-w_{,xy1}$, $-w_{,xy4}$

Table 7: Convergence of Tip Deflection for Cantilever Beam

Number of Elements	Present (in)		Tinawi [5] (in)
	Case 1	Case 2	
1 2 3	0.2857 0.3418 0.3504	0.3114 0.3530 0.3567	0.3393 0.3462 0.3513
Exact	0.3558		

Table 8: Stress σ_x Calculated for Totally Fixed Boundary Conditions (ksi)

	at A	at B	at C	at D
Present	70.69	49.60	29.63	9.79
Exact	70.00	50.00	30.00	10.00

Table 9: Linear Elastic Response of Simply Supported Beam

	Central Deflection (mm)	Strain Energy (Nm)	Maximum Stress (N/mm^2)
Present (% error)	44.486 (+0.22)	70.924 (-0.14)	1926.2 (+2.73)
Finite strip	44.560	70.924	1935.1
Exact	44.389	71.023	1875.0

Table 10: Linear Elastic Response of Simply Supported Square Plate

	Present and Koko [3]		Exact	Finite Strip
	Prediction	% Error		
Central Deflection (mm)	2.1889	+1.16	2.1639	2.1890
Strain Energy (Nm)	0.4517	-0.4	0.4535	0.4512

Table 11: Large Deflection Responses of Simply Supported Square Plate

Load (N/mm^2)	Central Deflection (mm)	
	Elastic	Elastic-Plastic
	Present and Koko [3]	Present and Koko [3]
0.04	0.5811	0.5811
0.08	0.8418	0.8418
0.12	1.015	1.015
0.16	1.147	1.147
0.20	1.256	1.259
0.24	1.350	1.365
0.28	1.432	1.463
0.32	1.506	1.552
0.36	1.574	1.646
0.40	1.636	1.747

Table 12: Large Deflection Elastic Response of Simply Supported Square Plate Without In-Plane Boundary Constraints

Load (N/mm²)	Central Deflection (mm)		Strain Energy (Nm)	
	Present	Koko [3]	Present	Koko [3]
0.04	0.7066	0.7128	0.0600	0.0599
0.08	1.1138	1.1218	0.1954	0.1931
0.12	1.3943	1.4031	0.3746	0.3693
0.16	1.6129	1.6221	0.5876	0.5782
0.20	1.7944	1.8039	0.8287	0.8143
0.24	1.9512	1.9608	1.0943	1.0741
0.28	2.0900	2.0997	1.3815	1.3548
0.32	2.2151	2.2250	1.6883	1.6544
0.36	2.3293	2.3394	2.0130	1.9714
0.40	2.4347	2.4450	2.3542	2.3044

Table 13: Linear Elastic Response of Clamped Square Plate

	Central Deflection (mm)	Strain Energy (Nm)
Present, 1 element (% error)	0.7102 (+5.8)	0.0972 (-6.2)
Present, 2 elements (% error)	0.6890 (+3.6)	0.0999 (-3.6)
Present, 4 elements (% error)	0.6699 (-0.2)	0.1027 (-0.9)
Finite strip	0.6915	0.1004
Exact	0.6715	0.1036

Table 14: Linear Elastic Response of Clamped 2-Bay Stiffened Plate

	Panel Centre Deflection, A (mm)	Stiffener Center Deflection, B (mm)	Strain Energy (Nm)
Present	0.471	0.042	0.335
Finite Strip	0.461	0.052	0.348

Table 15: Linear Elastic Response of Clamped DRES1B Stiffened Panel

	Super Element	ADINA
	Present and Koko [3]	
Deflection at C (in)	0.37	0.45
Deflection at D (in)	0.38	0.49
Deflection at E (in)	4.23	4.20
Deflection at F (in)	0.21	0.30
Strain Energy (kip-in)	580	

Table 16: Nonlinear Elastic Response of Clamped DRES1B Stiffened Panel

Load (psi)	Deflection at C (in)		Deflection at D (in)	
	Present and Koko [3]	ADINA	Present and Koko [3]	ADINA
10.0	0.075	0.094	0.078	0.099
20.0	0.150	0.188	0.155	0.197
30.0	0.224	0.281	0.231	0.295
40.0	0.297	0.374	0.307	0.391
50.0	0.369	0.465	0.381	0.486
Load (psi)	Deflection at E (in)		Deflection at F (in)	
	Present and Koko [3]	ADINA	Present and Koko [3]	ADINA
10.0	0.404	0.417	0.044	0.058
20.0	0.573	0.599	0.088	0.115
30.0	0.698	0.737	0.130	0.171
40.0	0.803	0.855	0.172	0.226
50.0	0.896	0.960	0.214	0.281

Table 17: Linear Elastic Results of Cubic Tube

Grid	Type of Element	Bending Displacements (mm)		Strain Energy (Nm)
		At Panel Centre (A)	At Free Edge Mid-Point (B)	
1x1	FPM	1.3742	1.5524	1.487067
	RBM	1.3742	1.5524	1.487067
	SBM	1.3742	1.5524	1.487066
2x2	FPM	1.3606	1.5481	1.5001048
	RBM	1.3606	1.5481	1.5001048
	SBM	1.3606	1.5481	1.5000872
4x4	FPM	1.3639	1.5477	1.5041056
	RBM	1.3639	1.5477	1.5041032
	SBM	1.3639	1.5477	1.5040568

Table 18: Linear and Nonlinear Results for Cubic Container

	Displacement at A (mm)		Displacement at B (mm)		Strain Energy (Nm)	
	Linear	Nonlinear	Linear	Nonlinear	Linear	Nonlinear
Present, 1x1 Grid	2.945	2.845	2.056	2.004	1.891	1.821
Present, 2x2 Grid	2.891	2.812	2.164	2.116	2.125	2.064
Present, 4x4 Grid	2.906	2.830	2.156	2.109	2.145	2.090
Finite Strip	3.043	2.960	2.337	2.280		
Experimental	2.911		2.172			

Table 19: Nonlinear Results for Two Thinner Cubic Containers

Plate Thickness (mm)	Displacement at A (mm)		Displacement at B (mm)	
	Present	Finite Strip	Present	Finite Strip
8	4.613	4.819	3.575	3.872
6	9.315	9.539	9.296	9.591

Table 20: Linear Elastic Response of Unstiffened Cubic Box

Grid	Bending Displacement (mm) at		Strain Energy (Nm)
	A	B	
1x1	0.7102		0.5845
2x2	0.6706	0.4028	0.6180
4x4	0.6746	0.4046	0.6233

Table 21: Linear Elastic Response of Stiffened Cubic Box

Type of Model	Beam Location	Grid	Bending Displacements (mm) at			Total Strain Energy (Nm)
			A	B	C	
Full Structure	Interior	2x2	0.01759	0.01102	0.05007	0.05284
		4x4	0.01813	0.01141	0.04787	0.05554
	Exterior	2x2	0.01798	0.01121	0.05019	0.05320
		4x4	0.01989	0.01267	0.04829	0.05706
Simplified	N/A	2x2	0.01653	0.01018	0.04947	0.05105*

*Total strain energy for the box is six times the value for a single panel.

Table 22: Natural Frequencies of Square Plate with Various Edge Constraints

Edge Constraints	λ			
	First Mode		Second Mode	
	Present & Koko [14]	Reference [13]	Present & Koko [14]	Reference [13]
CCCC	13.37	13.40		
CCCS	10.45	10.49	74.83	41.62
SCSC	8.63	8.64	41.59	31.13
CCSS	7.55	7.60	71.12	37.13
SSSC	5.75	5.77	38.07	27.75
CFCF	5.07	5.14	7.25	7.27
SSSS	4.00	4.00	35.38	25.00
SCSF	1.66	1.65	11.60	11.22

Table 23: Natural Frequencies of 3-Bay Continuous Plates

Mode Number	λ			
	Edges AD and BC Simply Supported		Edges AD and BC Clamped	
	Present & Koko [14]	Finite Strip [15]	Present & Koko [14]	Finite Strip [15]
1	12.94	12.94	12.98	12.99
2	20.20	19.74	22.84	20.84
3	21.54	21.61	25.67	25.89

Table 24: Natural Frequencies of 2x4 Bay Stiffened Plate with Clamped Edges (Hz)

Mode Number	Symmetry Condition	Present	Koko [14]
1	SS	1120.7	1112.4
2	SA	1304.8	1300.2
3	AA	1312.3	1312.2
4	AS	1423.6	1422.7
5	SS	1479.4	1479.4
6	SA	1524.0	1521.7

Table 25: Natural Frequencies of Cubic Tube Structure

Mode Number	Symmetry Condition	Natural Frequencies (Hz)		
		1x1 Grid	2x2 Grid	4x4 Grid
1	SSS	236	236	236
2	ASS	374	373	373
3	SAS	398	396	396
4	AAS	508	506	505
5	SSS	545	545	545
6	SAS	652	649	648
7	SSS	908	903	901
8	ASA		955	955
9	ASS		978	975
10	SSS		1074	1069
11	AAA		1147	1147
12	ASS		1215	1213
13	AAS		1383	1381
14	ASA		1499	1495
15	AAA		1649	1646
16	ASA		1741	1735
17	SAS		1863	1848
18	AAS		1916	1898
19	ASS		1934	1926
20	SAS		1980	1959

Table 26: Comparison of Present Predictions with Approximate Solutions for Natural Frequencies of Cubic Tube Structure (Hz)

Mode Number	Super Element Predictions for 1x1 Grid	Approximate Solutions	
		Boundary Conditions	Frequency
1	236	SFSF for all panels	236
3	398	SFSF for all panels	396
5	545	CFCF for all panels	545
6	652	CFCF for all panels	653
7	908	SFSF for all panels	901

Table 27: Natural Frequencies of Cubic Box Structure

Mode Number	Symmetry Condition	Natural Frequencies (Hz)		
		1x1 Grid	2x2 Grid	4x4 Grid
1	SSS	614	611	610
2	ASS	676	673	672
3	SSS	885	883	883
4	SAA		1290	1287
5	ASS		1429	1427
6	ASS		1571	1568
7	SAA		1722	1719
8	AAA		2148	2141
9	SAA		2304	2296
10	SSS		2477	2420
11	SSS		2561	2496
12	AAA		2657	2652
13	ASS		2871	2798
14	ASS		2891	2808
15	SSS		3250	3171
16	SSS		3324	3245
17	ASS		3391	3326
18	SAA		3514	3433
19	SAA		3836	3750
20	ASS		3967	3869

Table 28: Comparison of Present Predictions with Approximate Solutions for the First Three Frequencies of Cubic Box Structure (Hz)

Mode Number	Super Element Predictions for 1x1 Grid	Approximate Solutions	
		Boundary Conditions	Frequency
1	614	SSSS for 2 and SCSC for 4 panels	636
2	676	SSCC for all 6 panels	668
3	885	CCCC for all 6 panels	886

8. APPENDICES

Appendix A

Shape Functions for Super Plate Elements

With reference to Eq. (6), the matrix of shape function [N] is given by

$$[N] = \left[\begin{matrix} N_1^u & 0 & 0 & N_2^u & 0 & 0 & 0 & 0 & N_3^u & 0 \\ 0 & N_1^v & 0 & 0 & N_2^v & 0 & 0 & 0 & 0 & N_3^v \\ 0 & 0 & N_1^w & 0 & 0 & N_2^w & N_3^w & N_4^w & 0 & 0 \end{matrix}\right.$$

$$\begin{matrix} 0 & N_4^u & 0 & 0 & 0 & 0 & N_5^u & 0 & 0 & N_6^u \\ 0 & 0 & N_4^v & 0 & 0 & 0 & 0 & N_5^v & 0 & 0 \\ N_5^w & 0 & 0 & N_6^w & N_7^w & N_8^w & 0 & 0 & N_9^w & 0 \end{matrix}$$

$$\begin{matrix} 0 & 0 & 0 & 0 & N_7^u & 0 & 0 & N_8^u & 0 & 0 \\ N_6^v & 0 & 0 & 0 & 0 & N_7^v & 0 & 0 & N_8^v & 0 \\ 0 & N_{10}^w & N_{11}^w & N_{12}^w & 0 & 0 & N_{13}^w & 0 & 0 & N_{14}^w \end{matrix}$$

$$\begin{matrix} 0 & 0 & N_9^u & 0 & 0 & N_{12}^u & N_{15}^u & 0 & 0 & 0 \\ 0 & 0 & 0 & 0 & 0 & 0 & 0 & N_9^v & 0 & 0 \\ N_{15}^w & N_{16}^w & 0 & N_{17}^w & N_{18}^w & 0 & 0 & 0 & N_{19}^w & N_{20}^w \end{matrix}$$

$$\begin{array}{cccccccccc}
0 & 0 & N^u_{10} & 0 & 0 & N^u_{13} & N^u_{16} & 0 & 0 & 0 \\
N^v_{13} & N^v_{16} & 0 & 0 & 0 & 0 & 0 & N^v_{10} & 0 & 0 \\
-0 & 0 & 0 & N^w_{21} & N^w_{22} & 0 & 0 & 0 & N^w_{23} & N^w_{24}
\end{array}$$

$$\left.\begin{array}{ccccccccc}
0 & 0 & N^u_{11} & 0 & 0 & N^u_{14} & 0 & N^u_{17} & 0 \\
N^v_{12} & N^v_{15} & 0 & N^v_{11} & 0 & 0 & N^v_{14} & 0 & N^v_{17} \\
0 & 0 & 0 & 0 & N^w_{25} & 0 & 0 & 0 & 0
\end{array}\right] \qquad (A.1)$$

and the element nodal variable vector $\{\delta_e\}$ is defined as

$$\begin{aligned}\{\delta_e\}^T = \; & (u_1, v_1, w_1, u_{,y1}, v_{,x1}, w_{,x1}, w_{,y1}, w_{,xy1}, u_2, v_2, w_2, \\
& u_{,y2}, v_{,x2}, w_{,x2}, w_{,y2}, w_{,xy2}, u_3, v_3, w_3, u_{,y3}, v_{,x3}, \\
& w_{,x3}, w_{,y3}, w_{,xy3}, u_4, v_4, w_4, u_{,y4}, v_{,x4}, w_{,x4}, w_{,y4}, \\
& w_{,xy4}, u_5, w_5, w_{,y5}, u_8, u_{11}, v_5, w_6, w_{,x6}, v_9, v_{12}, \\
& u_6, w_7, w_{,y7}, u_9, u_{12}, v_6, w_8, w_{,x8}, v_8, v_{11}, u_7, v_7, \\
& w_9, u_{10}, v_{10}, u_{13}, v_{13})\end{aligned} \qquad (A.2)$$

In Eq. (A.1), the shape functions N^u_i, N^v_i and N^w_j are explicitly given by

$$\begin{array}{lll}
N^u_1 = L_1(\xi)H_1(\eta) & N^u_2 = L_1(\xi)H_2(\eta) & N^u_3 = L_2(\xi)H_1(\eta) \\
N^u_4 = L_2(\xi)H_2(\eta) & N^u_5 = L_2(\xi)H_3(\eta) & N^u_6 = L_2(\xi)H_4(\eta) \\
N^u_7 = L_1(\xi)H_3(\eta) & N^u_8 = L_1(\xi)H_4(\eta) & N^u_9 = L_3(\xi)L_1(\eta) \\
N^u_{10} = L_3(\xi)L_2(\eta) & N^u_{11} = L_3(\xi)L_3(\eta) & N^u_{12} = \sin 2\pi\xi \; L_1(\eta) \\
N^u_{13} = \sin 2\pi\xi \; L_2(\eta) & N^u_{14} = \sin 2\pi\xi \; L_3(\eta) & N^u_{15} = \sin 4\pi\xi \; L_1(\eta) \\
N^u_{16} = \sin 4\pi\xi \; L_2(\eta) & N^u_{17} = \sin 4\pi\xi \; L_3(\eta) &
\end{array} \qquad (A.3)$$

$$\begin{array}{lll}
N_1^V = H_1(\xi)L_1(\eta) & N_2^V = H_2(\xi)L_1(\eta) & N_3^V = H_3(\xi)L_1(\eta) \\
N_4^V = H_4(\xi)L_1(\eta) & N_5^V = H_3(\xi)L_2(\eta) & N_6^V = H_4(\xi)L_2(\eta) \\
N_7^V = H_1(\xi)L_2(\eta) & N_8^V = H_2(\xi)L_2(\eta) & N_9^V = L_2(\xi)L_3(\eta) \\
N_{10}^V = L_1(\xi)L_3(\eta) & N_{11}^V = L_3(\xi)L_3(\eta) & N_{12}^V = L_1(\xi)\sin 2\pi\eta \\
N_{13}^V = L_2(\xi)\sin 2\pi\eta & N_{14}^V = L_3(\xi)\sin 2\pi\eta & N_{15}^V = L_1(\xi)\sin 4\pi\eta \\
N_{16}^V = L_2(\xi)\sin 4\pi\eta & N_{17}^V = L_3(\xi)\sin 4\pi\eta &
\end{array} \tag{A.4}$$

$$\begin{array}{lll}
N_1^W = H_1(\xi)H_1(\eta) & N_2^W = H_2(\xi)H_1(\eta) & N_3^W = H_1(\xi)H_2(\eta) \\
N_4^W = H_2(\xi)H_2(\eta) & N_5^W = H_3(\xi)H_1(\eta) & N_6^W = H_4(\xi)H_1(\eta) \\
N_7^W = H_3(\xi)H_2(\eta) & N_8^W = H_4(\xi)H_2(\eta) & N_9^W = H_3(\xi)H_3(\eta) \\
N_{10}^W = H_4(\xi)H_3(\eta) & N_{11}^W = H_3(\xi)H_4(\eta) & N_{12}^W = H_4(\xi)H_4(\eta) \\
N_{13}^W = H_1(\xi)H_3(\eta) & N_{14}^W = H_2(\xi)H_3(\eta) & N_{15}^W = H_1(\xi)H_4(\eta) \\
N_{16}^W = H_2(\xi)H_4(\eta) & N_{17}^W = \phi(\xi)H_1(\eta) & N_{18}^W = \phi(\xi)H_2(\eta) \\
N_{19}^W = H_3(\xi)\phi(\eta) & N_{20}^W = H_4(\xi)\phi(\eta) & N_{21}^W = \phi(\xi)H_3(\eta) \\
N_{22}^W = \phi(\xi)H_4(\eta) & N_{23}^W = H_1(\xi)\phi(\eta) & N_{24}^W = H_2(\xi)\phi(\eta) \\
N_{25}^W = \phi(\xi)\phi(\eta) & &
\end{array} \tag{A.5}$$

The quadratic Lagrange polynomials are

$$L_1(\xi) = 2\xi^2-3\xi+1, \quad L_2(\xi) = 2\xi^2-\xi, \quad L_3(\xi) = 4(\xi-\xi^2) \tag{A.6}$$

The cubic Hermitian polynomials are

$$\begin{array}{ll}
H_1(\xi) = 1-3\xi^2+2\xi^3, & H_2(\xi) = a(\xi-2\xi^2+\xi^3) \\
H_3(\xi) = 3\xi^2-2\xi^3, & H_4(\xi) = a(-\xi^2+\xi^3)
\end{array} \tag{A.7}$$

Appendix B

Shape Functions for Super Beam Elements

With reference to Eq. (11), the beam shape function matrix $[\bar{N}]$ is given by

$$
[\bar{N}] = \left[\begin{array}{ccccccc}
L_1(\xi) & 0 & eH_1'(\xi) & 0 & eH_2'(\xi) & 0 & 0 \\
0 & 0 & H_1(\xi) & 0 & H_2(\xi) & 0 & 0 \\
0 & 0 & 0 & 0 & 0 & H_1(\xi) & H_2(\xi) \\
0 & H_1(\xi) & 0 & H_2(\xi) & 0 & eH_1(\xi) & eH_2(\xi)
\end{array} \right.
$$

$$
\begin{array}{ccccccc}
L_2(\xi) & 0 & eH_3'(\xi) & 0 & eH_4'(\xi) & 0 & 0 \\
0 & 0 & H_3(\xi) & 0 & H_4(\xi) & 0 & 0 \\
0 & 0 & 0 & 0 & 0 & H_3(\xi) & H_4(\xi) \\
0 & H_3(\xi) & 0 & H_4(\xi) & 0 & eH_3(\xi) & eH_4(\xi)
\end{array}
$$

$$
\left. \begin{array}{ccccc}
L_3(\xi) & e\phi'(\xi) & 0 & \sin 2\pi\xi & \sin 4\pi\xi \\
0 & \phi(\xi) & 0 & 0 & 0 \\
0 & 0 & \phi(\xi) & 0 & 0 \\
0 & 0 & e\phi(\xi) & 0 & 0
\end{array} \right] \tag{B.1}
$$

and the beam nodal displacement vector $\{\bar{\delta}_e\}$ is defined as

$$
\{\bar{\delta}_e\}^T = (u_1,\ v_1,\ w_1,\ v_{,x^1},\ w_{,x^2},\ \theta_1,\ \theta_{,x^1},\ u_2,\ v_2,\ w_2,
$$

$$
v_{,x^2},\ w_{,x^2},\ \theta_2,\ \theta_{,x^2},\ u_3,\ w_3,\ \theta_3,\ u_4,\ u_5) \tag{B.2}
$$

The beam displacement fields described by Eq. (11) were partitioned into two parts in Eqs. (12) and (13). Details of the expressions for $[\bar{N}_I]$, $[\bar{N}_{II}]$, $[\bar{N}^P_{II}]$, $\{\bar{\delta}^I_e\}$ and $\{\bar{\delta}^{II}_e\}$ are given in the following

$$[\bar{N}_I] = \begin{bmatrix} L_1(\xi) & eH_1'(\xi) & eH_1'(\xi) & L_2(\xi) & eH_3'(\xi) & eH_4'(\xi) & L_3(\xi) \\ 0 & H_1(\xi) & H_2(\xi) & 0 & H_3(\xi) & H_4(\xi) & 0 \end{bmatrix.$$

$$\left. \begin{matrix} e\phi_1'(\xi) & \sin 2\pi\xi & \sin 4\pi\xi \\ \phi(\xi) & 0 & 0 \end{matrix} \right] \tag{B.3}$$

$$[\bar{N}_{II}] = \begin{bmatrix} H_1(\xi) & H_2(\xi) & H_3(\xi) & H_4(\xi) & \phi(\xi) \\ eH_1(\xi) & eH_2(\xi) & eH_3(\xi) & eH_4(\xi) & e\phi(\xi) \end{bmatrix.$$

$$\left. \begin{matrix} 0 & 0 & 0 & 0 \\ H_1(\xi) & H_2(\xi) & H_3(\xi) & H_4(\xi) \end{matrix} \right]. \tag{B.4}$$

$$[\bar{N}^P_{II}] = \begin{bmatrix} H_1(\xi) & H_2(\xi) & H_3(\xi) & H_4(\xi) & \phi(\xi) \\ 0 & 0 & 0 & 0 & 0 \end{bmatrix.$$

$$\left. \begin{matrix} 0 & 0 & 0 & 0 \\ H_1(\xi) & H_2(\xi) & H_3(\xi) & H_4(\xi) \end{matrix} \right] \tag{B.5}$$

$$\{\bar{\delta}^I_e\}^T = (u_1, w_1, w_{,x^1}, u_2, w_2, w_{,x^2}, u_3, w_3, u_4, u_5) \tag{B.6}$$

$$\{\bar{\delta}^{II}_e\}^T = (\theta_1, \theta_{,x^1}, \theta_2, \theta_{,x^2}, \theta_3, v_1, v_{,x_1}, v_2, v_{,x^2}) \tag{B.7}$$

Appendix C

Strain-Displacement Matrices

Using Eq. (17), the virtual strains can be related to the virtual displacements by

$$\{\delta\epsilon\} = [[B] + [C_L]]\{\delta u\} \qquad \text{(C.1)}$$

where $\{\delta\epsilon\}$ is the vector of virtual strains, $\{\delta u\}$ is the vector of virtual displacements, and $[B]$ and $[C_L]$ are the linear and nonlinear strain-displacement matrices, respectively. For plate elements, $[B]$ and $[C_L]$ are of the order of 3 x 59 and 1 x 10 for beam elements.

Details of the [B] Matrix

For plate elements, the [B] matrix is given by

$$[B] = \left[\begin{matrix}
\frac{\partial N_1^u}{\partial x} & 0 & -z\frac{\partial^2 N_1^w}{\partial x^2} & \frac{\partial N_2^u}{\partial x} & 0 & -z\frac{\partial^2 N_2^w}{\partial x^2} & -z\frac{\partial^2 N_3^w}{\partial x^2} \\
0 & \frac{\partial N_1^v}{\partial y} & -z\frac{\partial^2 N_1^w}{\partial y^2} & 0 & \frac{\partial N_2^v}{\partial y} & -z\frac{\partial^2 N_2^w}{\partial y^2} & -z\frac{\partial^2 N_3^w}{\partial y^2} \\
\frac{\partial N_1^u}{\partial y} & \frac{\partial N_1^v}{\partial x} & -2z\frac{\partial^2 N_1^w}{\partial x\partial y} & \frac{\partial N_2^u}{\partial y} & \frac{\partial N_2^v}{\partial x} & -2z\frac{\partial^2 N_2^w}{\partial x\partial y} & -2z\frac{\partial^2 N_3^w}{\partial x\partial y}
\end{matrix}\right.$$

$$\left.\begin{matrix}
-z\frac{\partial^2 N_4^w}{\partial x^2} & \frac{\partial N_3^u}{\partial x} & 0 & -z\frac{\partial^2 N_5^w}{\partial x^2} & \frac{\partial N_4^u}{\partial x} & 0 & -z\frac{\partial^2 N_6^w}{\partial x^2} \\
-z\frac{\partial^2 N_4^w}{\partial y^2} & 0 & \frac{\partial N_3^v}{\partial y} & -z\frac{\partial^2 N_5^w}{\partial y^2} & 0 & \frac{\partial N_4^v}{\partial y} & -z\frac{\partial^2 N_6^w}{\partial y^2} \\
-2z\frac{\partial^2 N_4^w}{\partial x\partial y} & \frac{\partial N_3^u}{\partial y} & \frac{\partial N_3^v}{\partial x} & -2z\frac{\partial^2 N_5^w}{\partial x\partial y} & \frac{\partial N_4^u}{\partial y} & \frac{\partial N_4^v}{\partial x} & -2z\frac{\partial^2 N_6^w}{\partial x\partial y}
\end{matrix}\right.$$

$$\begin{array}{ccccccc}
-z\,\dfrac{\partial^2 N_7^w}{\partial x^2} & -z\,\dfrac{\partial^2 N_8^w}{\partial x^2} & \dfrac{\partial N_5^u}{\partial x} & 0 & -z\,\dfrac{\partial^2 N_9^w}{\partial x^2} & \dfrac{\partial N_6^u}{\partial x} & 0 \\
-z\,\dfrac{\partial^2 N_7^w}{\partial y^2} & -z\,\dfrac{\partial^2 N_8^w}{\partial y^2} & 0 & \dfrac{\partial N_5^v}{\partial y} & -z\,\dfrac{\partial^2 N_9^w}{\partial y^2} & 0 & \dfrac{\partial N_6^v}{\partial y} \\
-2z\,\dfrac{\partial^2 N_7^w}{\partial x\partial y} & -2z\,\dfrac{\partial^2 N_8^w}{\partial x\partial y} & \dfrac{\partial N_5^u}{\partial y} & \dfrac{\partial N_5^v}{\partial x} & -2z\,\dfrac{\partial^2 N_9^w}{\partial x\partial y} & \dfrac{\partial N_6^u}{\partial y} & \dfrac{\partial N_6^v}{\partial x}
\end{array}$$

$$\begin{array}{ccccccc}
-z\,\dfrac{\partial^2 N_{10}^w}{\partial x^2} & -z\,\dfrac{\partial^2 N_{11}^w}{\partial x^2} & -z\,\dfrac{\partial^2 N_{12}^w}{\partial x^2} & \dfrac{\partial N_7^u}{\partial x} & 0 & -z\,\dfrac{\partial^2 N_{13}^w}{\partial x^2} & \dfrac{\partial N_8^u}{\partial x} \\
-z\,\dfrac{\partial^2 N_{10}^w}{\partial y^2} & -z\,\dfrac{\partial^2 N_{11}^w}{\partial y^2} & -z\,\dfrac{\partial^2 N_{12}^w}{\partial y^2} & 0 & \dfrac{\partial N_7^v}{\partial y} & -z\,\dfrac{\partial^2 N_{13}^w}{\partial y^2} & 0 \\
-2z\,\dfrac{\partial^2 N_{10}^w}{\partial x\partial y} & -2z\,\dfrac{\partial^2 N_{11}^w}{\partial x\partial y} & -2z\,\dfrac{\partial^2 N_{12}^w}{\partial x\partial y} & \dfrac{\partial N_7^u}{\partial y} & \dfrac{\partial N_7^v}{\partial x} & -2z\,\dfrac{\partial^2 N_{13}^w}{\partial x\partial y} & \dfrac{\partial N_8^u}{\partial y}
\end{array}$$

$$\begin{array}{ccccccc}
0 & -z\,\dfrac{\partial^2 N_{14}^w}{\partial x^2} & -z\,\dfrac{\partial^2 N_{15}^w}{\partial x^2} & -z\,\dfrac{\partial^2 N_{16}^w}{\partial x^2} & \dfrac{\partial N_9^u}{\partial x} & -z\,\dfrac{\partial^2 N_{17}^w}{\partial x^2} & -z\,\dfrac{\partial^2 N_{18}^w}{\partial x^2} \\
\dfrac{\partial N_8^v}{\partial y} & -z\,\dfrac{\partial^2 N_{14}^w}{\partial y^2} & -z\,\dfrac{\partial^2 N_{15}^w}{\partial y^2} & -z\,\dfrac{\partial^2 N_{16}^w}{\partial y^2} & 0 & -z\,\dfrac{\partial^2 N_{17}^w}{\partial y^2} & -z\,\dfrac{\partial^2 N_{18}^w}{\partial y^2} \\
\dfrac{\partial N_8^v}{\partial x} & -2z\,\dfrac{\partial^2 N_{14}^w}{\partial x\partial y} & -2z\,\dfrac{\partial^2 N_{15}^w}{\partial x\partial y} & -2z\,\dfrac{\partial^2 N_{16}^w}{\partial x\partial y} & \dfrac{\partial N_9^u}{\partial y} & -2z\,\dfrac{\partial^2 N_{17}^w}{\partial x\partial y} & -2z\,\dfrac{\partial^2 N_{18}^w}{\partial x\partial y}
\end{array}$$

$$\begin{array}{ccccccc}
\dfrac{\partial N_{12}^u}{\partial x} & \dfrac{\partial N_{15}^u}{\partial x} & 0 & -z\,\dfrac{\partial^2 N_{19}^w}{\partial x^2} & -z\,\dfrac{\partial^2 N_{20}^w}{\partial x^2} & 0 & 0 \\
0 & 0 & \dfrac{\partial N_9^v}{\partial y} & -z\,\dfrac{\partial^2 N_{19}^w}{\partial y^2} & -z\,\dfrac{\partial^2 N_{20}^w}{\partial y^2} & \dfrac{\partial N_{13}^v}{\partial y} & \dfrac{\partial N_{16}^v}{\partial y} \\
\dfrac{\partial N_{12}^u}{\partial y} & \dfrac{\partial N_{15}^u}{\partial y} & \dfrac{\partial N_9^v}{\partial x} & -2z\,\dfrac{\partial^2 N_{19}^w}{\partial x\partial y} & -2z\,\dfrac{\partial^2 N_{20}^w}{\partial x\partial y} & \dfrac{\partial N_{13}^v}{\partial x} & \dfrac{\partial N_{16}^v}{\partial x}
\end{array}$$

$$
\begin{matrix}
\frac{\partial N^u_{10}}{\partial x} & -z\,\frac{\partial^2 N^w_{21}}{\partial x^2} & -z\,\frac{\partial^2 N^w_{22}}{\partial x^2} & \frac{\partial N^u_{13}}{\partial x} & \frac{\partial N^u_{16}}{\partial x} & 0 & -z\,\frac{\partial^2 N^w_{23}}{\partial x^2} \\
0 & -z\,\frac{\partial^2 N^w_{21}}{\partial y^2} & -z\,\frac{\partial^2 N^w_{22}}{\partial y^2} & 0 & 0 & \frac{\partial N^v_{10}}{\partial y} & -z\,\frac{\partial^2 N^w_{23}}{\partial y^2} \\
\frac{\partial N^u_{10}}{\partial y} & -2z\,\frac{\partial^2 N^w_{21}}{\partial x \partial y} & -2z\,\frac{\partial^2 N^w_{22}}{\partial x \partial y} & \frac{\partial N^u_{13}}{\partial y} & \frac{\partial N^u_{16}}{\partial y} & \frac{\partial N^v_{10}}{\partial x} & -2z\,\frac{\partial^2 N^w_{23}}{\partial x \partial y}
\end{matrix}
$$

$$
\begin{matrix}
-z\,\frac{\partial^2 N^w_{24}}{\partial x^2} & 0 & 0 & \frac{\partial N^u_{11}}{\partial x} & 0 & -z\,\frac{\partial^2 N^w_{25}}{\partial x^2} & \frac{\partial N^u_{14}}{\partial x} \\
-z\,\frac{\partial^2 N^w_{24}}{\partial y^2} & \frac{\partial N^v_{12}}{\partial y} & \frac{\partial N^v_{15}}{\partial y} & 0 & \frac{\partial N^v_{11}}{\partial y} & -z\,\frac{\partial^2 N^w_{25}}{\partial y^2} & 0 \\
-2z\,\frac{\partial^2 N^w_{24}}{\partial x \partial y} & \frac{\partial N^v_{12}}{\partial x} & \frac{\partial N^v_{15}}{\partial x} & \frac{\partial N^u_{11}}{\partial y} & \frac{\partial N^v_{11}}{\partial x} & -2z\,\frac{\partial^2 N^w_{25}}{\partial x \partial y} & \frac{\partial N^u_{14}}{\partial y}
\end{matrix}
$$

$$
\left.
\begin{matrix}
0 & \frac{\partial N^u_{17}}{\partial x} & 0 \\
\frac{\partial N^v_{14}}{\partial y} & 0 & \frac{\partial N^v_{17}}{\partial y} \\
\frac{\partial N^v_{14}}{\partial x} & \frac{\partial N^u_{17}}{\partial y} & \frac{\partial N^v_{17}}{\partial x}
\end{matrix}
\right] \tag{C.2}
$$

For a beam element in the x-direction, the [B] matrix is given by

$$
[B] = \left[\frac{dL_1}{dx},\ (e-z)\,\frac{d^2H_1}{dx^2},\ (e-z)\,\frac{d^2H_2}{dx^2},\ \frac{dL_2}{dx},\ (e-z)\,\frac{d^2H_3}{dx^2}, \right.
$$

$$
\left. (e-z)\,\frac{d^2H_4}{dx^2},\ \frac{dL_3}{dx},\ (e-z)\,\frac{d^2\phi}{dx^2},\ \frac{d}{dx}\,(\sin 2\pi\xi),\ \frac{d}{dx}\,(\sin 4\pi\xi) \right] \tag{C.3}
$$

The [B] matrix for a beam in the y-direction takes the same form as that given by Eq. (C.3) except that x is replaced by y and ξ by η.

Details of the $[C_L]$ Matrix

For plate elements, the $[C_L]$ matrix is given by

$$[C_L] = \left[\begin{matrix} 0 & 0 & \frac{\partial N_1^w}{\partial x}\frac{\partial N_j^w}{\partial x}w_j & 0 & 0 \\ 0 & 0 & \frac{\partial N_1^w}{\partial y}\frac{\partial N_j^w}{\partial y}w_j & 0 & 0 \\ 0 & 0 & (\frac{\partial N_1^w}{\partial x}\frac{\partial N_j^w}{\partial y}+\frac{\partial N_1^w}{\partial y}\frac{\partial N_j^w}{\partial x})w_j & 0 & 0 \end{matrix}\right.$$

$$\begin{matrix} \frac{\partial N_2^w}{\partial x}\frac{\partial N_j^w}{\partial x}w_j & \frac{\partial N_3^w}{\partial x}\frac{\partial N_j^w}{\partial x}w_j & \frac{\partial N_4^w}{\partial x}\frac{\partial N_j^w}{\partial x}w_j \\ \frac{\partial N_2^w}{\partial y}\frac{\partial N_j^w}{\partial y}w_j & \frac{\partial N_3^w}{\partial y}\frac{\partial N_j^w}{\partial y}w_j & \frac{\partial N_4^w}{\partial y}\frac{\partial N_j^w}{\partial y}w_j \\ (\frac{\partial N_2^w}{\partial x}\frac{\partial N_j^w}{\partial y}+\frac{\partial N_2^w}{\partial y}\frac{\partial N_j^w}{\partial x})w_j & (\frac{\partial N_3^w}{\partial x}\frac{\partial N_j^w}{\partial y}+\frac{\partial N_3^w}{\partial y}\frac{\partial N_j^w}{\partial x})w_j & (\frac{\partial N_4^w}{\partial x}\frac{\partial N_j^w}{\partial y}+\frac{\partial N_4^w}{\partial y}\frac{\partial N_j^w}{\partial x})w_j \end{matrix}$$

$$\begin{matrix} 0 & 0 & \frac{\partial N_5^w}{\partial x}\frac{\partial N_j^w}{\partial x}w_j & 0 & 0 \\ 0 & 0 & \frac{\partial N_5^w}{\partial y}\frac{\partial N_j^w}{\partial y}w_j & 0 & 0 \\ 0 & 0 & (\frac{\partial N_5^w}{\partial x}\frac{\partial N_j^w}{\partial y}+\frac{\partial N_5^w}{\partial y}\frac{\partial N_j^w}{\partial x})w_j & 0 & 0 \end{matrix}$$

$$
\begin{array}{ccc}
\frac{\partial N_6^w}{\partial x}\frac{\partial N_j^w}{\partial x}w_j & \frac{\partial N_7^w}{\partial x}\frac{\partial N_j^w}{\partial x}w_j & \frac{\partial N_8^w}{\partial x}\frac{\partial N_j^w}{\partial x}w_j \\
\frac{\partial N_6^w}{\partial y}\frac{\partial N_j^w}{\partial y}w_j & \frac{\partial N_7^w}{\partial y}\frac{\partial N_j^w}{\partial y}w_j & \frac{\partial N_8^w}{\partial y}\frac{\partial N_j^w}{\partial y}w_j \\
(\frac{\partial N_6^w}{\partial x}\frac{\partial N_j^w}{\partial y}+\frac{\partial N_6^w}{\partial y}\frac{\partial N_j^w}{\partial x})w_j & (\frac{\partial N_7^w}{\partial x}\frac{\partial N_j^w}{\partial y}+\frac{\partial N_7^w}{\partial y}\frac{\partial N_j^w}{\partial x})w_j & (\frac{\partial N_8^w}{\partial x}\frac{\partial N_j^w}{\partial y}+\frac{\partial N_8^w}{\partial y}\frac{\partial N_j^w}{\partial x})w_j
\end{array}
$$

$$
\begin{array}{ccccc}
0 & 0 & \frac{\partial N_9^w}{\partial x}\frac{\partial N_j^w}{\partial x}w_j & 0 & 0 \\
0 & 0 & \frac{\partial N_9^w}{\partial y}\frac{\partial N_j^w}{\partial y}w_j & 0 & 0 \\
0 & 0 & (\frac{\partial N_9^w}{\partial x}\frac{\partial N_j^w}{\partial y}+\frac{\partial N_9^w}{\partial y}\frac{\partial N_j^w}{\partial x})w_j & 0 & 0
\end{array}
$$

$$
\begin{array}{ccc}
\frac{\partial N_{10}^w}{\partial x}\frac{\partial N_j^w}{\partial x}w_j & \frac{\partial N_{11}^w}{\partial x}\frac{\partial N_j^w}{\partial x}w_j & \frac{\partial N_{12}^w}{\partial x}\frac{\partial N_j^w}{\partial x}w_j \\
\frac{\partial N_{10}^w}{\partial y}\frac{\partial N_j^w}{\partial y}w_j & \frac{\partial N_{11}^w}{\partial y}\frac{\partial N_j^w}{\partial y}w_j & \frac{\partial N_{12}^w}{\partial y}\frac{\partial N_j^w}{\partial y}w_j \\
(\frac{\partial N_{10}^w}{\partial x}\frac{\partial N_j^w}{\partial y}+\frac{\partial N_{10}^w}{\partial y}\frac{\partial N_j^w}{\partial x})w_j & (\frac{\partial N_{11}^w}{\partial x}\frac{\partial N_j^w}{\partial y}+\frac{\partial N_{11}^w}{\partial y}\frac{\partial N_j^w}{\partial x})w_j & (\frac{\partial N_{12}^w}{\partial x}\frac{\partial N_j^w}{\partial y}+\frac{\partial N_{12}^w}{\partial y}\frac{\partial N_j^w}{\partial x})w_j
\end{array}
$$

$$
\begin{array}{ccccc}
0 & 0 & \frac{\partial N_{13}^w}{\partial x}\frac{\partial N_j^w}{\partial x}w_j & 0 & 0 \\
0 & 0 & \frac{\partial N_{13}^w}{\partial y}\frac{\partial N_j^w}{\partial y}w_j & 0 & 0 \\
0 & 0 & (\frac{\partial N_{13}^w}{\partial x}\frac{\partial N_j^w}{\partial y}+\frac{\partial N_{13}^w}{\partial y}\frac{\partial N_j^w}{\partial x})w_j & 0 & 0
\end{array}
$$

$$\begin{array}{lll}
\frac{\partial N^w_{14}}{\partial x}\frac{\partial N^w_j}{\partial x}w_j & \frac{\partial N^w_{15}}{\partial x}\frac{\partial N^w_j}{\partial x}w_j & \frac{\partial N^w_{16}}{\partial x}\frac{\partial N^w_j}{\partial x}w_j \\
\frac{\partial N^w_{14}}{\partial y}\frac{\partial N^w_j}{\partial y}w_j & \frac{\partial N^w_{15}}{\partial y}\frac{\partial N^w_j}{\partial y}w_j & \frac{\partial N^w_{16}}{\partial y}\frac{\partial N^w_j}{\partial y}w_j \\
(\frac{\partial N^w_{14}}{\partial x}\frac{\partial N^w_j}{\partial y}+\frac{\partial N^w_{14}}{\partial y}\frac{\partial N^w_j}{\partial x})w_j & (\frac{\partial N^w_{15}}{\partial x}\frac{\partial N^w_j}{\partial y}+\frac{\partial N^w_{15}}{\partial y}\frac{\partial N^w_j}{\partial x})w_j & (\frac{\partial N^w_{16}}{\partial x}\frac{\partial N^w_j}{\partial y}+\frac{\partial N^w_{16}}{\partial y}\frac{\partial N^w_j}{\partial x})w_j
\end{array}$$

$$\begin{array}{lllll}
0 & \frac{\partial N^w_{17}}{\partial x}\frac{\partial N^w_j}{\partial x}w_j & \frac{\partial N^w_{18}}{\partial x}\frac{\partial N^w_j}{\partial x}w_j & 0 & 0 \\
0 & \frac{\partial N^w_{17}}{\partial y}\frac{\partial N^w_j}{\partial y}w_j & \frac{\partial N^w_{18}}{\partial y}\frac{\partial N^w_j}{\partial y}w_j & 0 & 0 \\
0 & (\frac{\partial N^w_{17}}{\partial x}\frac{\partial N^w_j}{\partial y}+\frac{\partial N^w_{17}}{\partial y}\frac{\partial N^w_j}{\partial x})w_j & (\frac{\partial N^w_{18}}{\partial x}\frac{\partial N^w_j}{\partial y}+\frac{\partial N^w_{18}}{\partial y}\frac{\partial N^w_j}{\partial x})w_j & 0 & 0
\end{array}$$

$$\begin{array}{lllll}
0 & \frac{\partial N^w_{19}}{\partial x}\frac{\partial N^w_j}{\partial x}w_j & \frac{\partial N^w_{20}}{\partial x}\frac{\partial N^w_j}{\partial x}w_j & 0 & 0 \\
0 & \frac{\partial N^w_{19}}{\partial y}\frac{\partial N^w_j}{\partial y}w_j & \frac{\partial N^w_{20}}{\partial y}\frac{\partial N^w_j}{\partial y}w_j & 0 & 0 \\
0 & (\frac{\partial N^w_{19}}{\partial x}\frac{\partial N^w_j}{\partial y}+\frac{\partial N^w_{19}}{\partial y}\frac{\partial N^w_j}{\partial x})w_j & (\frac{\partial N^w_{20}}{\partial x}\frac{\partial N^w_j}{\partial y}+\frac{\partial N^w_{20}}{\partial y}\frac{\partial N^w_j}{\partial x})w_j & 0 & 0
\end{array}$$

$$\begin{array}{lllll}
0 & \frac{\partial N^w_{21}}{\partial x}\frac{\partial N^w_j}{\partial x}w_j & \frac{\partial N^w_{22}}{\partial x}\frac{\partial N^w_j}{\partial x}w_j & 0 & 0 \\
0 & \frac{\partial N^w_{21}}{\partial y}\frac{\partial N^w_j}{\partial y}w_j & \frac{\partial N^w_{22}}{\partial y}\frac{\partial N^w_j}{\partial y}w_j & 0 & 0 \\
0 & (\frac{\partial N^w_{21}}{\partial x}\frac{\partial N^w_j}{\partial y}+\frac{\partial N^w_{21}}{\partial y}\frac{\partial N^w_j}{\partial x})w_j & (\frac{\partial N^w_{22}}{\partial x}\frac{\partial N^w_j}{\partial y}+\frac{\partial N^w_{22}}{\partial y}\frac{\partial N^w_j}{\partial x})w_j & 0 & 0
\end{array}$$

$$\begin{array}{ccccc}
0 & \frac{\partial N^w_{23}}{\partial x}\frac{\partial N^w_j}{\partial x}w_j & \frac{\partial N^w_{24}}{\partial x}\frac{\partial N^w_j}{\partial x}w_j & 0 & 0 \\
0 & \frac{\partial N^w_{23}}{\partial y}\frac{\partial N^w_j}{\partial y}w_j & \frac{\partial N^w_{24}}{\partial y}\frac{\partial N^w_j}{\partial y}w_j & 0 & 0 \\
0 & (\frac{\partial N^w_{23}}{\partial x}\frac{\partial N^w_j}{\partial y}+\frac{\partial N^w_{23}}{\partial y}\frac{\partial N^w_j}{\partial x})w_j & (\frac{\partial N^w_{24}}{\partial x}\frac{\partial N^w_j}{\partial y}+\frac{\partial N^w_{24}}{\partial y}\frac{\partial N^w_j}{\partial x})w_j & 0 & 0
\end{array}$$

$$\left.\begin{array}{cccccccc}
0 & 0 & \frac{\partial N^w_{25}}{\partial x}\frac{\partial N^w_j}{\partial x}w_j & 0 & 0 & 0 & 0 \\
0 & 0 & \frac{\partial N^w_{25}}{\partial y}\frac{\partial N^w_j}{\partial y}w_j & 0 & 0 & 0 & 0 \\
0 & 0 & (\frac{\partial N^w_{25}}{\partial x}\frac{\partial N^w_j}{\partial y}+\frac{\partial N^w_{25}}{\partial y}\frac{\partial N^w_j}{\partial x})w_j & 0 & 0 & 0 & 0
\end{array}\right] \tag{C.4}$$

where j = 1,2,...,25 and $\{w_j\}^T = (w_1, w_{,x^1}, w_{,y^1}, w_{,xy^1}, w_2, w_{,x^2}, w_{,y^2}, w_{,xy^2}, w_3, w_{,x^3}, w_{,y^3}, w_{,xy^3}, w_4, w_{,x^4}, w_{,y^4}, w_{,xy^4}, w_5, w_{,x^5}, w_{,y^5}, w_6, w_{,y^6}, w_7, w_{,y^7}, w_8, w_{,x^8}, w_9)$.

For a beam element in the x-direction, the $[C_L]$ matrix is given by

$$[C_L] = \left[0, \frac{dH_1}{dx}\frac{dH_j}{dx}w_j, \frac{dH_2}{dx}\frac{dH_j}{dx}w_j, 0, \frac{dH_3}{dx}\frac{dH_j}{dx}w_j, \frac{dH_4}{dx}\frac{dH_j}{dx}w_j, \right.$$

$$\left. 0, \frac{dH_5}{dx}\frac{dH_j}{dx}w_j, 0, 0 \right] \tag{C.5}$$

where j = 1,2,...,5, $H_5 = \phi(\xi)$ and $\{w_j\}^T = (w_1, w_{,x^1}, w_2, w_{,x^2}, w_3)$.

The $[C_L]$ matrix for a beam in the y-direction takes the same form as given by Eq. (C.5) except that all the derivatives are taken with respect to y instead of x.

Appendix D

Constitutive Matrices

With reference to Eq. 20, the constitutive matrix [D] takes one of the following forms depending on the material behaviour. For the linear elastic behaviour, the [D] matrix is given by

$$[D_e] = \frac{E}{1-\nu^2}\begin{bmatrix} 1 & \nu & 0 \\ \nu & 1 & 0 \\ 0 & 0 & \frac{1-\nu}{2} \end{bmatrix} \qquad (D.1)$$

and for the elastoplastic behaviour it takes the form

$$[D_{ep}] = [D_e] - \frac{[D_e]\{\frac{\partial F}{\partial \sigma}\}\{\frac{\partial F}{\partial \sigma}\}^T[D_e]}{\{\frac{\partial F}{\partial \sigma}\}^T[D_e]\{\frac{\partial F}{\partial \sigma}\} + \frac{E\,E_T}{E-E_T}} \qquad (D.2)$$

where E, ν are the Young's modulus and Poisson's ratio, respectively, E_T is the slope of the second segment of uniaxial stress-strain curve, and $F = (\sigma_x^2 - \sigma_x\sigma_y + \sigma_y^2 + 3\tau_{xy}^2) - \sigma_o^2 = 0$ is the yield surface with σ_o being the yield stress.

Appendix E

Beam Torsional Mass Matrix

For a beam element in the x-direction, the beam torsional mass matrix is calculated by

$$[m_b^t] = [m_{b_1}^t] + [m_{b_2}^t] + [m_{b_3}^t] \qquad \text{(E.1)}$$

where

$$[m_{b_1}^t] = \rho J_0 \begin{bmatrix} \frac{13a}{35} & \frac{11a^2}{210} & \frac{9a}{70} & -\frac{13a^2}{420} & \mu_4 a & 0 & 0 & 0 & 0 \\ \frac{11a^2}{210} & \frac{a^3}{105} & \frac{13a^2}{420} & -\frac{a^3}{140} & \mu_5 a^2 & 0 & 0 & 0 & 0 \\ \frac{9a}{70} & \frac{13a^2}{420} & \frac{13a}{35} & -\frac{11a^2}{210} & \mu_4 a & 0 & 0 & 0 & 0 \\ -\frac{13a^2}{420} & -\frac{a^3}{140} & -\frac{11a^2}{210} & \frac{a^3}{105} & -\mu_5 a^2 & 0 & 0 & 0 & 0 \\ \mu_4 a & \mu_5 a^2 & \mu_4 a & -\mu_5 a^2 & \mu_6 a & 0 & 0 & 0 & 0 \\ 0 & 0 & 0 & 0 & 0 & 0 & 0 & 0 & 0 \\ 0 & 0 & 0 & 0 & 0 & 0 & 0 & 0 & 0 \\ 0 & 0 & 0 & 0 & 0 & 0 & 0 & 0 & 0 \\ 0 & 0 & 0 & 0 & 0 & 0 & 0 & 0 & 0 \end{bmatrix} \qquad \text{(E.2)}$$

$$[m^t_{b_2}] = \rho A \begin{bmatrix} 0 & 0 & 0 & 0 & 0 & 0 & 0 & 0 & 0 \\ 0 & 0 & 0 & 0 & 0 & 0 & 0 & 0 & 0 \\ 0 & 0 & 0 & 0 & 0 & 0 & 0 & 0 & 0 \\ 0 & 0 & 0 & 0 & 0 & 0 & 0 & 0 & 0 \\ 0 & 0 & 0 & 0 & 0 & 0 & 0 & 0 & 0 \\ 0 & 0 & 0 & 0 & 0 & \frac{13a}{35} & \frac{11a^2}{210} & \frac{9a}{70} & -\frac{13a^2}{420} \\ 0 & 0 & 0 & 0 & 0 & \frac{11a^2}{210} & \frac{a^3}{105} & \frac{13a^2}{420} & -\frac{a^3}{140} \\ 0 & 0 & 0 & 0 & 0 & \frac{9a}{70} & \frac{13a^2}{420} & \frac{13a}{35} & -\frac{11a^2}{210} \\ 0 & 0 & 0 & 0 & 0 & -\frac{13a^2}{420} & -\frac{a^3}{140} & -\frac{11a^2}{210} & \frac{a^3}{105} \end{bmatrix} \tag{E.3}$$

$$[m^t_{b_3}] = \rho A e \begin{bmatrix} 0 & 0 & 0 & 0 & 0 & \frac{13a}{35} & \frac{11a^2}{210} & \frac{9a}{70} & -\frac{13a^2}{420} \\ 0 & 0 & 0 & 0 & 0 & \frac{11a^2}{210} & \frac{a^3}{105} & \frac{13a^2}{420} & -\frac{a^3}{140} \\ 0 & 0 & 0 & 0 & 0 & \frac{9a}{70} & \frac{13a^2}{420} & \frac{13a}{35} & -\frac{11a^2}{210} \\ 0 & 0 & 0 & 0 & 0 & -\frac{13a^2}{420} & -\frac{a^3}{140} & -\frac{11a^2}{210} & \frac{a^3}{105} \\ 0 & 0 & 0 & 0 & 0 & \mu_4 a & \mu_5 a^2 & \mu_4 a & -\mu_5 a^2 \\ \frac{13a}{35} & \frac{11a^2}{210} & \frac{9a}{70} & -\frac{13a^2}{420} & \mu_4 a & 0 & 0 & 0 & 0 \\ \frac{11a^2}{210} & \frac{a^3}{105} & \frac{13a^2}{420} & -\frac{a^3}{140} & \mu_5 a^2 & 0 & 0 & 0 & 0 \\ \frac{9a}{70} & \frac{13a^2}{420} & \frac{13a}{35} & -\frac{11a^2}{210} & \mu_4 a & 0 & 0 & 0 & 0 \\ -\frac{13a^2}{420} & -\frac{a^3}{140} & -\frac{11a^2}{210} & \frac{a^3}{105} & -\mu_5 a^2 & 0 & 0 & 0 & 0 \end{bmatrix} \tag{E.4}$$

with $\mu_4 = 0.2615821802$, $\mu_5 = 0.0562872124$ and $\mu_6 = 0.396478085$.

For a beam in the y-direction, replace a by b in the above expressions.

Appendix F

Geometric Stiffness Matrices

The geometric stiffness matrix [Ω] (Eq. 38) is a symmetric square matrix of order 59x59 for plates elements and 10x10 for beam elements. The typical entry in [Ω] for a plate element is given by Eq. 39. The following chart summarizes the correspondence between the indices i,j and the subscripts r,s in Eq. 43.

i or j	r or s	i or j	r or s	i or j	r or s
1	0	21	0	41	0
2	0	22	10	42	0
3	1	23	11	43	0
4	0	24	12	44	21
5	0	25	0	45	22
6	2	26	0	46	0
7	3	27	13	47	0
8	4	28	0	48	0
9	0	29	0	49	23
10	0	30	14	50	24
11	5	31	15	51	0
12	0	32	16	52	0
13	0	33	0	53	0
14	6	34	17	54	0
15	7	35	18	55	25
16	8	36	0	56	0
17	0	37	0	57	0
18	0	38	0	58	0
19	9	39	19	59	0
20	0	40	20		

For a beam element in the x-direction, the typical entry is given by Eq. (40). The correspondence rule for the index pairs (i,j) and (r,s) in Eq. (40) is defined in the following chart.

i or j	1	2	3	4	5	6	7	8	9	10
r or s	0	1	2	0	3	4	0	5	0	0

It is noted that the entry Ω_{ij} is zero if one of the subscripts r,s corresponding to the indices i,j is zero.

For a beam element in the y-direction, the typical entry in $[\Omega]$ is given by

$$\Omega_{ij} = \frac{dN_r^b}{dy}\frac{dN_s^b}{dy}\sigma_y \qquad (i,j = 1,2,\ldots,10;\ \ r,s = 1,2,\ldots,5) \qquad \text{(F.1)}$$

The correspondence chart above is still applicable in this case.

Appendix G

Beam Torsional Stiffness Matrix

The beam torsoinal stiffness matrix is given by Eq. (44). For a beam element in the x-direction, the four sub-matrices $[k^t_{bi}]$ (i = 1,2,3,4) are defined by

$$[k^t_{b_1}] = \frac{GJ}{a}\begin{bmatrix} \frac{6}{5} & \frac{a}{10} & -\frac{6}{5} & \frac{a}{10} & 0 & 0 & 0 & 0 & 0 \\ \frac{a}{10} & \frac{2a^2}{15} & -\frac{a}{10} & -\frac{a^2}{30} & \mu_1 a & 0 & 0 & 0 & 0 \\ -\frac{6}{5} & -\frac{a}{10} & \frac{6}{5} & -\frac{a}{10} & 0 & 0 & 0 & 0 & 0 \\ \frac{a}{10} & -\frac{a^2}{30} & -\frac{a}{10} & \frac{2a^2}{15} & -\mu_1 a & 0 & 0 & 0 & 0 \\ 0 & \mu_1 a & 0 & -\mu_1 a & \mu_2 & 0 & 0 & 0 & 0 \\ 0 & 0 & 0 & 0 & 0 & 0 & 0 & 0 & 0 \\ 0 & 0 & 0 & 0 & 0 & 0 & 0 & 0 & 0 \\ 0 & 0 & 0 & 0 & 0 & 0 & 0 & 0 & 0 \\ 0 & 0 & 0 & 0 & 0 & 0 & 0 & 0 & 0 \end{bmatrix} \tag{G.1}$$

$$[k^t_{b_2}] = \frac{EI_{zz}}{a^3}\begin{bmatrix} 0 & 0 & 0 & 0 & 0 & 0 & 0 & 0 & 0 \\ 0 & 0 & 0 & 0 & 0 & 0 & 0 & 0 & 0 \\ 0 & 0 & 0 & 0 & 0 & 0 & 0 & 0 & 0 \\ 0 & 0 & 0 & 0 & 0 & 0 & 0 & 0 & 0 \\ 0 & 0 & 0 & 0 & 0 & 0 & 0 & 0 & 0 \\ 0 & 0 & 0 & 0 & 0 & 12 & 6a & -12 & 6a \\ 0 & 0 & 0 & 0 & 0 & 6a & 4a^2 & -6a & 2a^2 \\ 0 & 0 & 0 & 0 & 0 & -12 & -6a & 12 & -6a \\ 0 & 0 & 0 & 0 & 0 & 6a & 2a^2 & -6a & 4a^2 \end{bmatrix} \tag{G.2}$$

$$[k^t_{b_3}] = \frac{EI_{zz}e}{a^3}\begin{bmatrix} 0 & 0 & 0 & 0 & 0 & 12 & 6a & -12 & 6a \\ 0 & 0 & 0 & 0 & 0 & 6a & 4a^2 & -6a & 2a^2 \\ 0 & 0 & 0 & 0 & 0 & -12 & -6a & 12 & -6a \\ 0 & 0 & 0 & 0 & 0 & 6a & 2a^2 & -6a & 4a^2 \\ 0 & 0 & 0 & 0 & 0 & 0 & 0 & 0 & 0 \\ 12 & 6a & -12 & 6a & 0 & 0 & 0 & 0 & 0 \\ 6a & 4a^2 & -6a & 2a^2 & 0 & 0 & 0 & 0 & 0 \\ -12 & -6a & 12 & -6a & 0 & 0 & 0 & 0 & 0 \\ 6a & 2a^2 & -6a & 4a^2 & 0 & 0 & 0 & 0 & 0 \end{bmatrix} \tag{G.3}$$

$$[k^t_{b_4}] = \frac{E(e^2 I_{zz}+\Gamma)}{a^3}\begin{bmatrix} 12 & 6a & -12 & 6a & 0 & 0 & 0 & 0 & 0 \\ 6a & 4a^2 & -6a & 2a^2 & 0 & 0 & 0 & 0 & 0 \\ -12 & -6a & 12 & -6a & 0 & 0 & 0 & 0 & 0 \\ 6a & 2a^2 & -6a & 4a^2 & 0 & 0 & 0 & 0 & 0 \\ 0 & 0 & 0 & 0 & \mu_3 & 0 & 0 & 0 & 0 \\ 0 & 0 & 0 & 0 & 0 & 0 & 0 & 0 & 0 \\ 0 & 0 & 0 & 0 & 0 & 0 & 0 & 0 & 0 \\ 0 & 0 & 0 & 0 & 0 & 0 & 0 & 0 & 0 \\ 0 & 0 & 0 & 0 & 0 & 0 & 0 & 0 & 0 \end{bmatrix} \tag{G.4}$$

with $\mu_1 = 0.5231643586$, $\mu_2 = 4.877697585$, and $\mu_3 = 198.4629301$.

For a beam in the y-direction, replace a by b in the above expressions.

Appendix H

Direction Cosines

The direction cosines a_{ij} used in Eq. (61) are given by

$$
\begin{aligned}
a_{11} &= (X_2-X_1)/s_{21} \\
a_{12} &= (Y_2-Y_1)/s_{21} \\
a_{13} &= (Z_2-Z_1)/s_{21} \\
a_{21} &= (X_4-X_1)/s_{41} \\
a_{22} &= (Y_4-Y_1)/s_{41} \\
a_{23} &= (Z_4-Z_1)/s_{41} \\
a_{31} &= a_{12}a_{23}-a_{22}a_{13} \\
a_{32} &= a_{21}a_{13}-a_{11}a_{23} \\
a_{33} &= a_{11}a_{22}-a_{12}a_{21}
\end{aligned}
\tag{H.1}
$$

where X_i, Y_i and Z_i are the global coordinates of node i and s_{ij} is the length of the side ij given by

$$s_{ij} = \sqrt{(X_j-X_i)^2 + (Y_j-Y_i)^2 + (Z_j-Z_i)^2} \tag{H.2}$$

Appendix I

Transformation Matrices for Folded Plate Model

The transformation matrix $[\chi_I]$ relates the modified nodal vector $\{\delta_e^*\}$ (Eq. 64) to the original nodal vector $\{\delta_e\}$ (Eq. A.2). The entry in $[\chi_I]$ is either zero or one (with positive or negative sign), and the order of matrix $[\chi_I]$ is 59x59. All the non-zero entries, $(\chi_I)_{ij}$, are listed below with the indices i and j representing the row and column numbers, respectively.

i,j	$(\chi_I)_{ij}$	i,j	$(\chi_I)_{ij}$	i,j	$(\chi_I)_{ij}$	i,j	$(\chi_I)_{ij}$
1,1	1	18,16	1	35,31	1	52,52	1
2,2	1	19,17	1	36,32	1	53,53	1
3,3	1	20,20	-1	37,33	1	54,54	1
4,6	-1	21,47	1	38,36	1	55,55	1
5,34	1	22,19	-1	39,37	1	56,56	1
6,5	-1	23,18	1	40,38	-1	57,57	1
7,4	1	24,21	1	41,39	1	58,58	1
8,7	1	25,22	1	42,40	1	59,59	1
9,8	1	26,23	1	43,41	1		
10,9	1	27,24	1	44,42	1		
11,10	1	28,27	-1	45,43	1		
12,13	-1	29,46	1	46,44	1		
13,35	1	30,26	-1	47,45	1		
14,12	-1	31,25	1	48,48	1		
15,11	1	32,28	1	49,49	1		
16,14	1	33,29	1	50,50	-1		
17,15	1	34,30	1	51,51	1		

For the beam elements, $[\bar{\chi}_I]$ has the following non-zero entries.

in the x-direction				in the y-direction			
i,j	$(\bar{\chi}_I)_{ij}$	i,j	$(\bar{\chi}_I)_{ij}$	i,j	$(\bar{\chi}_I)_{ij}$	i,j	$(\bar{\chi}_I)_{ij}$
1,1	1	11,19	1	1,2	1	11,13	-1
2,2	1	12,11	-1	2,1	1	12,11	1
3,3	1	13,10	1	3,3	1	13,12	1
4,18	1	14,12	1	4,6	-1	14,14	1
5,5	-1	15,13	1	5,4	1	15,15	1
6,4	1	16,14	1	6,5	1	16,16	1
7,6	1	17,15	1	7,7	1	17,17	1
8,7	1	18,16	1	8,9	1	18,18	1
9,8	1	19,17	1	9,8	1	19,19	1
10,9	1			10,10	1		

Appendix J

Transformation Matrices for Rectangular Box Model

For the super plate element, the transformation matrix $[\chi_{II}]$ in Eq. (79) usually varies with location of the element due to different compatibility requirements. To illustrate the mathematical details in the formulation of $[\chi_{II}]$, let us consider the most complicated case of element ABED in Figure 10. For this element it is assumed that the local x and y axes are along the global Z and X directions, respectively. At the four corner nodes 1 to 4, the rotation Θ_z is defined, respectively, as

$$\begin{aligned}
\Theta_{z^1} &= v_{,x^1} - u_{,y^1} \\
\Theta_{z^2} &= v_{,x^2} \\
\Theta_{z^3} &= v_{,x^3} - u_{,y^3} \\
\Theta_{z^4} &= -u_{,y^4}
\end{aligned}$$

For the shear strain γ_{xy}, the following assumptions are used,

a) $\gamma_{xy_1} = 0$ is satisfied through boundary conditions,

b) γ_{xy_2} is moved from the corner node 2 to the mid-side node 6,

c) γ_{xy_4} is moved from the corner node 4 to the mid-side node 7.

The modified nodal vector $\{\delta_e^*\}$ can be expressed as

$$\begin{aligned}
\{\delta_e^*\}^T = (&u_1, v_1, w_1, \Theta_{x^1}, \Theta_{y^1}, \Theta_{z^1}, w_{,xy^1}, \gamma_{xy^1}, u_2, v_2, w_2, \\
&\Theta_{x^2}, \Theta_{y^2}, \Theta_{z^2}, w_{,xy^2}, u_3, v_3, w_3, \Theta_{x^3}, \Theta_{y^3}, \Theta_{z^3}, w_{,xy^3}, \\
&\gamma_{xy^3}, u_4, v_4, w_4, \Theta_{x^4}, \Theta_{y^4}, \Theta_{z^4}, w_{,xy^4}, u_5, w_5, \Theta_{x^5}, \\
&u_8, u_{11}, v_5, w_6, \Theta_{y^6}, v_9, v_{12}, \gamma_{xy^2}, u_6, w_7, \Theta_{x^7}, u_9, \\
&u_{12}, \gamma_{xy^4}, v_6, w_8, \Theta_{y^8}, v_8, v_{11}, u_7, v_7, w_9, u_{10}, v_{10}, \\
&u_{13}, v_{13}) \qquad (J.2)
\end{aligned}$$

The transformation matrix $[\chi_{II}]$ associated with Eq. (J.2) is given by the following table for the non-zero entries.

i,j	$(\chi_{II})_{ij}$	i,j	$(\chi_{II})_{ij}$	i,j	$(\chi_{II})_{ij}$	i,j	$(\chi_{II})_{ij}$
1,1	1	15,12	1	29,47	1	46,45	1
2,2	1	16,15	1	30,28	-1	47,46	1
3,3	1	17,16	1	31,27	1	48,48	1
4,6	-1	18,17	1	32,30	1	49,49	1
4,8	1	19,18	1	33,31	1	50,50	-1
5,6	1	20,21	-1	34,32	1	51,51	1
5,8	1	20,23	1	35,33	1	52,52	1
6,5	-1	21,21	1	36,34	1	53,53	1
7,4	1	21,23	1	37,35	1	54,54	1
8,7	1	22,20	-1	38,36	1	55,55	1
9,9	1	23,19	1	39,37	1	56,56	1
10,10	1	24,22	1	40,38	-1	57,57	1
11,11	1	25,24	1	41,39	1	58,58	1
12,14	-1	26,25	1	42,40	1	59,59	1
12,41	1	27,26	1	43,42	1		
13,14	1	28,29	-1	44,43	1		
14,13	-1	29,29	1	45,44	1		

For the super beam element, $[\bar{\chi}_{II}]$ has the following non-zero entries.

in the x-direction				in the y-direction			
i,j	$(\bar{\chi}_{II})_{ij}$	i,j	$(\bar{\chi}_{II})_{ij}$	i,j	$(\bar{\chi}_{II})_{ij}$	i,j	$(\bar{\chi}_{II})_{ij}$
1,1	1	11,13	1	1,2	1	11,13	-1
2,2	1	12,12	-1	2,1	1	12,11	1
3,3	1	13,11	1	3,3	1	13,12	1
4,6	1	14,14	1	4,6	-1	14,14	1
5,5	-1	15,15	1	5,4	1	15,15	1
6,4	1	16,16	1	6,5	1	16,16	1
7,7	1	17,17	1	7,7	1	17,17	1
8,8	1	18,18	1	8,9	1	18,18	1
9,9	1	19,19	1	9,8	1	19,19	1
10,10	1			10,10	1		

The transformation matrix $[\bar{\Lambda}_{II}]$ is given by

$$[\bar{\Lambda}_{II}] = [\bar{\Lambda}_{I}] \tag{J.3}$$

Appendix K

Theoretical Calculations for Cubic Tube Structure

Assuming the problem is one-dimensional, the plate bending differential equation can be written as

$$D \frac{d^4 w}{dx^4} - N_o \frac{d^2 w}{dx^2} = q_o \qquad (-L \leq x \leq L) \qquad \text{(K.1)}$$

where $D = Eh^3/12(1-\nu^2)$ is the plate flexural rigidity, h is the plate thickness, E is the Young's modulus, ν is the Poisson's ratio, $N_o = q_o L$ is the in-plane force, q_o is the applied pressure and L is half of the total length.

First, consider the internal pressure loading, i.e. $N_o \geq 0$. The general solution to Eq. (K.1) can be expressed by the following form:

$$w = A \cosh kx + B \sinh kx + Cx + D - \frac{q_o x^2}{2N_o} \qquad \text{(K.2)}$$

where $k^2 = N_o/D$. By symmetry, it is required that B = 0 and C = 0. Eq. (K.2) is reduced to

$$A \cosh kx + D - \frac{qx^2}{2N_o} = 0 \qquad \text{(K.3)}$$

Now, applying the boundary conditions

$$w(x = \pm L) = 0, \quad w'(x = \pm L) = 0 \qquad \text{(K.4)}$$

and after solving for A and D, the final expression is obtained as

$$w = \frac{q_oL}{KN_o}\left[\frac{\cosh kx}{\sinh kL} + \frac{kL}{2} - \frac{\cosh kL}{\sin kL}\right] - \frac{q_ox^2}{2N_o} \qquad (I.5)$$

The maximum deflection occurs at x=0 and is given by

$$w_{max} = \frac{1 - \cosh kL}{k \sinh kL} + \frac{L}{2} \qquad (K.6)$$

Next, consider the case of external pressure loading, i.e. $N_o \leq 0$. In this case replace q_o and N_o by $-q_o$ and $-N_o$, respectively, in Eq. (K.1). Noting that $k^2 = -N_o/D$, the general solution is obtained by substituting ik for k in Eq. (K.2).

$$w = A \cosh ikx + B \sinh ikx + Cx + D - \frac{q_ox^2}{2N_o} \qquad (K.7)$$

Applying the same boundary conditions as before and using

$$\sinh iz = i \sin z, \qquad \cosh iz = \cos z \qquad (K.8)$$

the following equation is obtained

$$w = \frac{\cos kL - \cos kx}{k \sin kL} + \frac{L^2 - x^2}{2L} \qquad (K.9)$$

The maximum deflection is given by

$$w_{max} = w(x=0) = \frac{\cos kL-1}{k \sin kL} + \frac{L}{2} \tag{K.10}$$

To calculate in-plane displacement, let us write the strain-displacement relation first

$$\epsilon_x = \frac{du}{dx} + \frac{1}{2} \left(\frac{dw}{dx}\right)^2 \tag{K.11}$$

and after introducing Hooke's law

$$\epsilon_x = \frac{\sigma_x}{E} = \frac{N_o}{Et} \tag{K.12}$$

the following differential equation is obtained

$$\frac{du}{dx} = \frac{N_o}{Et} - \frac{1}{2} \left(\frac{dw}{dx}\right)^2 \tag{K.13}$$

By symmetry we assume that u=0 at x=0. Then

$$u_L = u(x=L) = \frac{N_o L}{Et} - \frac{1}{2} \int_o^L \left(\frac{dw}{dx}\right)^2 dx \tag{K.14}$$

Substituting Eqs. (K.5) and (K.9), respectively, into Eq. (K.14) and carrying out proper differentiation and integration leads to

$$\frac{u_L}{L} = \frac{q_o L}{Et} - \frac{1}{2} \left[\frac{1}{3} + \frac{2}{(kL)^2} - \frac{3\coth kL}{2kL} - \frac{\cosh^2 kL}{2} \right] \tag{K.15}$$

for the internal pressure loading, and

$$\frac{u_L}{L} = \frac{-q_oL}{Et} - \frac{1}{(kL)^2\sin^2 kL}\left[\frac{1}{2}(kL)^2 + \left[\frac{(kL)^2}{3} - 2\right]\sin^2 kL \right.$$

$$\left. + \frac{3}{2}\, kL \sin kL \cos kL\right] \tag{K.16}$$

for the external pressure loading.

The total strain energy is then given by

$$U = U_1 + U_2 \tag{K.17}$$

where U_1, U_2 represent the strain energy due to plate bending and in-plane displacements, respectively, given by

$$U_1 = \frac{1}{2} \int\int_A q_o w \, dA = q_o L \int_{-L}^{L} w \, dx \tag{K.18}$$

and

$$U_2 = \frac{1}{2} q_o (2L)^2 u_L = 2q_o L^2 u_L \tag{K.19}$$

It is noted that Eq. (K.19) was derived based on the assumption that the in-plane strain energy is equal to the work done by the pressure load q_o through rigid body motion due to u_L.

Introducing the correct displacement function into Eq. (K.18) and after carrying out the integration, the plate bending strain energy can be explicitly written as

$$U_1 = 2D\left[1 + \left(\frac{kL}{2} - \coth kL\right) kL\right] - \frac{q_o L^3}{3}$$

$$= \frac{2D(kL)^4}{45}\left[1 - \frac{2}{21}(kL)^2\right] \qquad \text{(K.20)}$$

for the internal pressure loading, and

$$U_1 = 2D(1 - kL \coth kL) - \frac{2q_o L^3}{3} \qquad \text{(K.21)}$$

for the external pressure loading.

To calculate buckling load for the external pressure loading case, we use Eq. (K.9) again and notice that

$$w \rightarrow \infty \qquad \text{for} \qquad \sin kL = 0 \qquad \text{(K.22)}$$

Thus, the necessary condition for the buckling of plate is given by

$$kL = \pi \qquad \text{(K.23)}$$

and, finally, the buckling load is obtained by expanding Eq. (K.23), that is,

$$q_{ocr} = \frac{\pi^2}{L^3} D = \frac{\pi^2 Et^3}{12(1-\nu^2)L^3} \qquad (K.24)$$

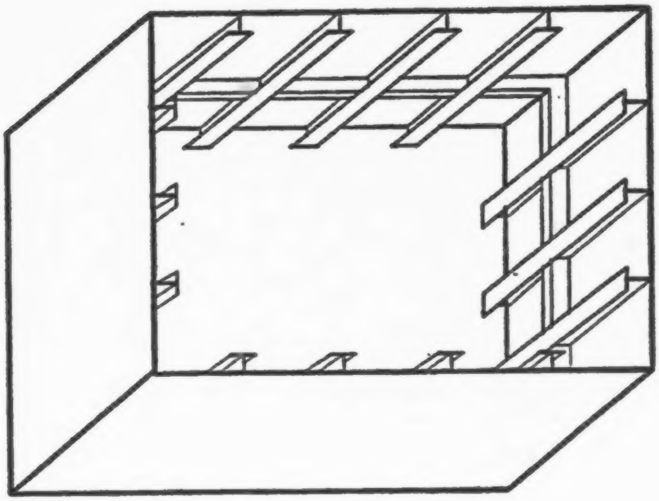

Fig. 1: A Typical Open-Ended, Rib-Stiffened Box Structure.

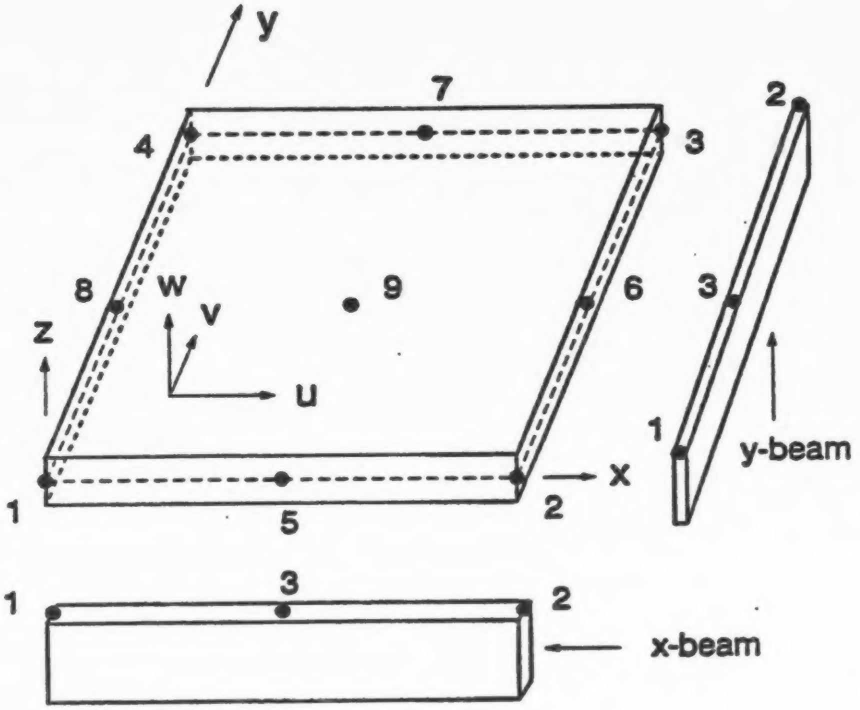
y
7
4
3
2
8
W
V
9
6
3
Z
u
1
y-beam
1
2
X
5
1
3
2
x-beam

Fig. 2: Assemblage of Plate and Beam Elements.

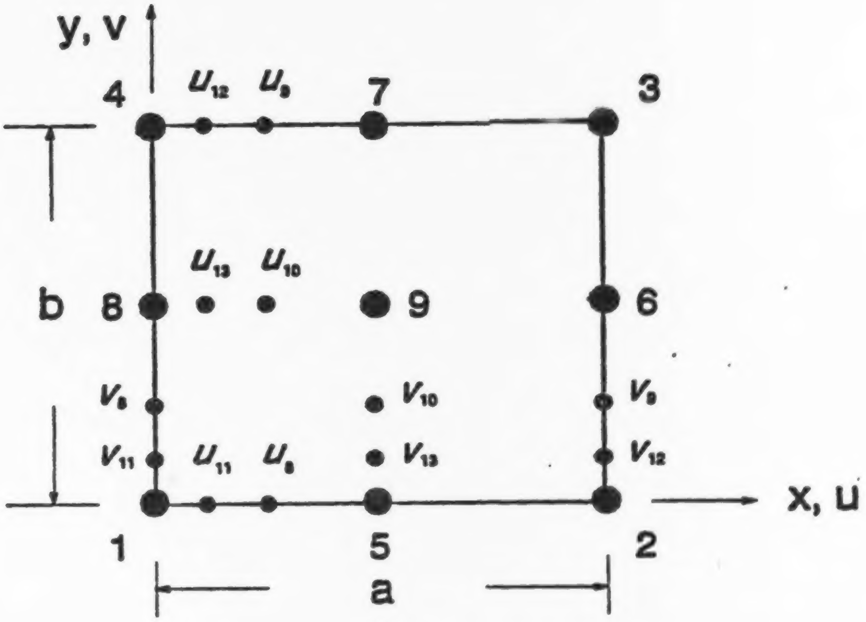
y, v
4
U12
U9
7
3
U13
U10
b
8
9
6
V8
V10
V9
V11
U11
U8
V13
V12
x, u
1
5
2
a

(a) Plate Element

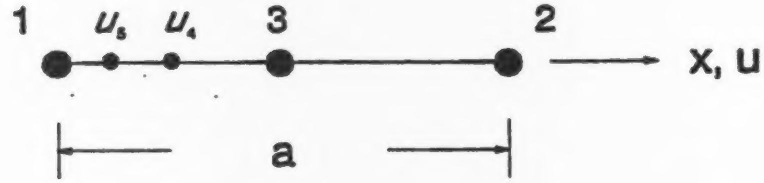
1
U5
U4
3
2
x, u
a

(b) Beam Element in x Direction

Fig. 3: Nodal Configuration of Super Elements.

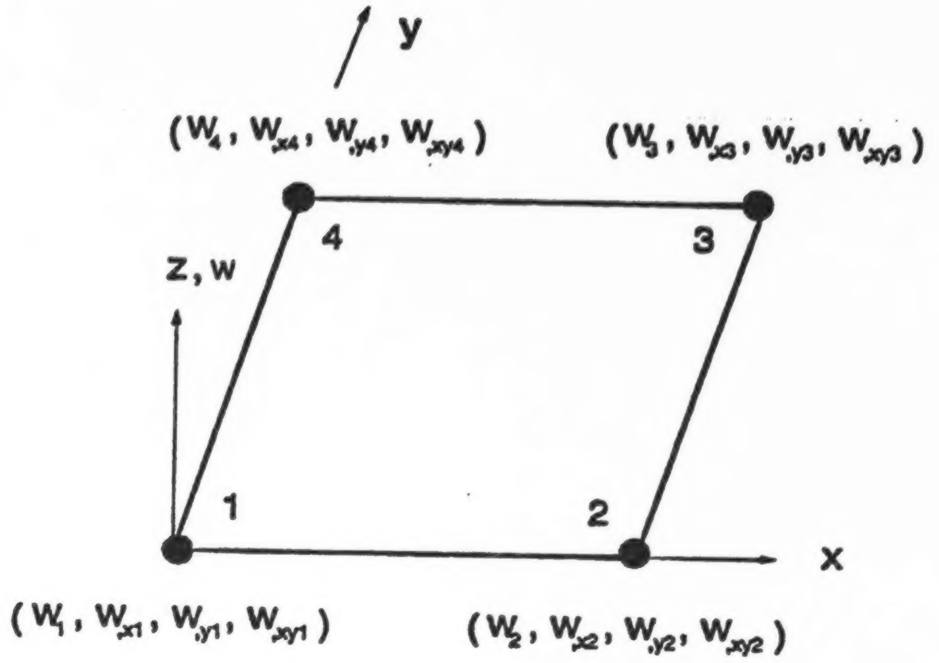
y
(W4 , W,x4 , W,y4 , W,xy4)
(W3 , W,x3 , W,y3 , W,xy3)
4
3
z, w
1
2
x
(W1 , W,x1 , W,y1 , W,xy1)
(W2 , W,x2 , W,y2 , W,xy2)

Fig. 4: Rectangular Conforming Plate Bending Element [4].

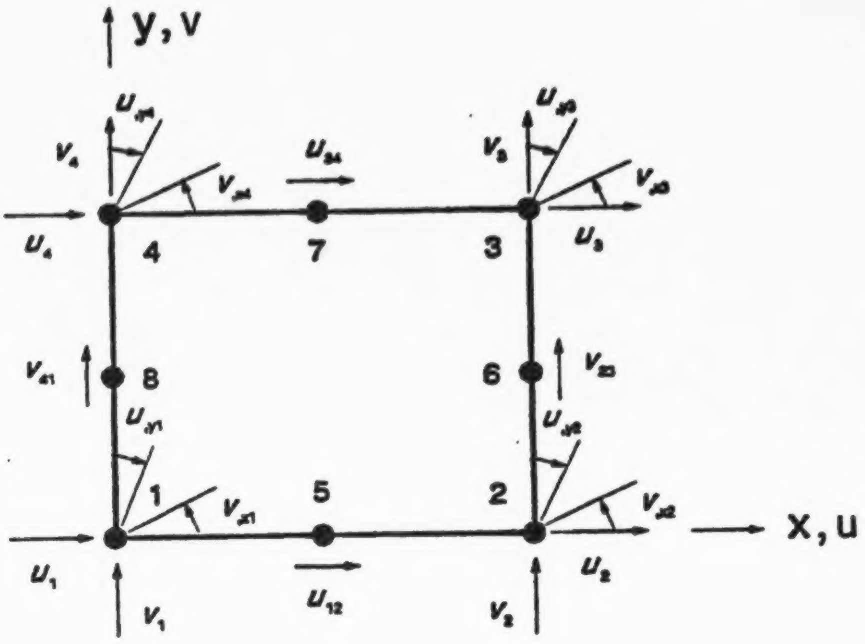
y, v
$U_{,y4}$
V_4
$V_{,x4}$
U_{34}
V_3
$U_{,y3}$
$V_{,x3}$
U_4
4
7
3
U_3
V_{41}
8
6
V_{23}
$U_{,y1}$
$U_{,y2}$
1
$V_{,x1}$
5
2
$V_{,x2}$
X, u
U_1
V_1
U_{12}
V_2
U_2

Fig. 5: Rectangular Plane Stress Element [5].

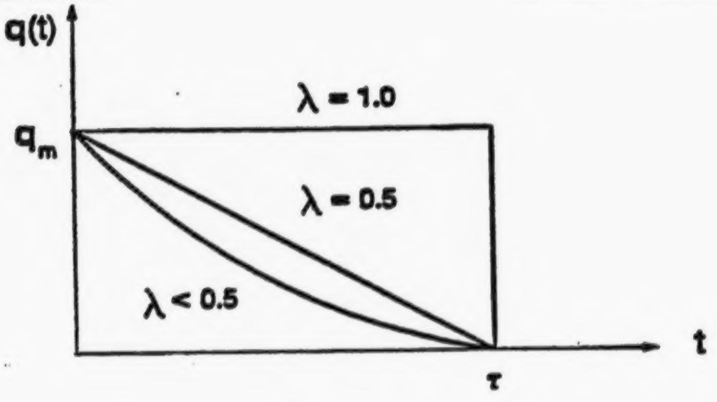

(a) Logarithmic Decay

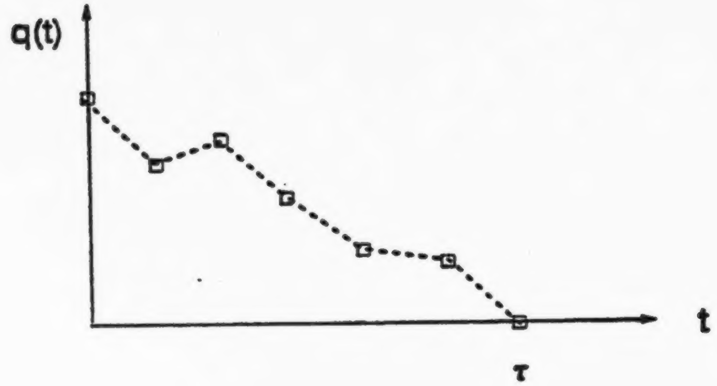

(b) Discrete Data Points

Fig. 6: Shapes of Typical Blast Loads.

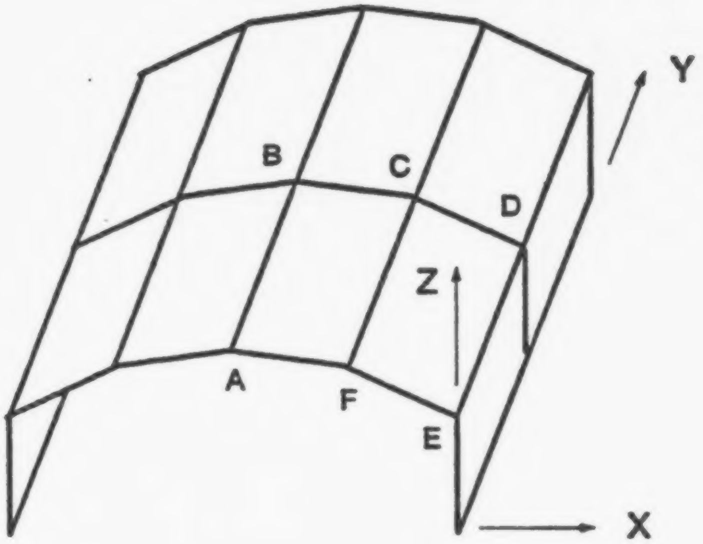

Fig. 7: Super Finite Element Discretization of a Folded Plate Structure.

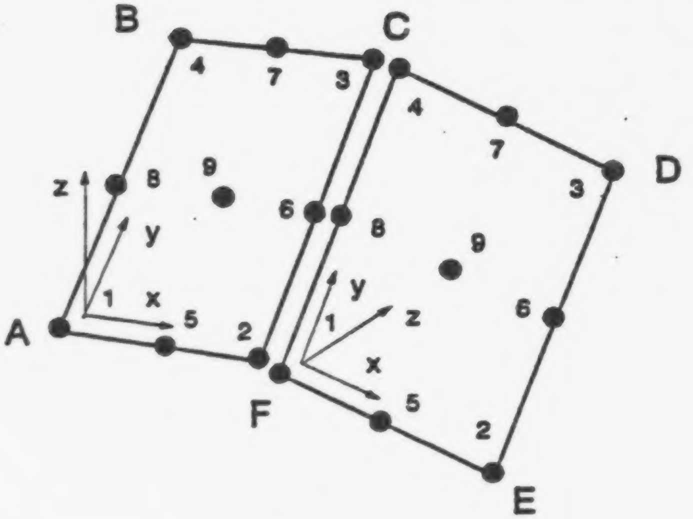
B
C
D
E
F
A
4
7
3
8
9
6
2
5
1
x
y
z
4
7
3
8
9
6
5
2
1
x
y
z

Fig. 8: Two Adjacent Plate Elements Along an Angular Junction.

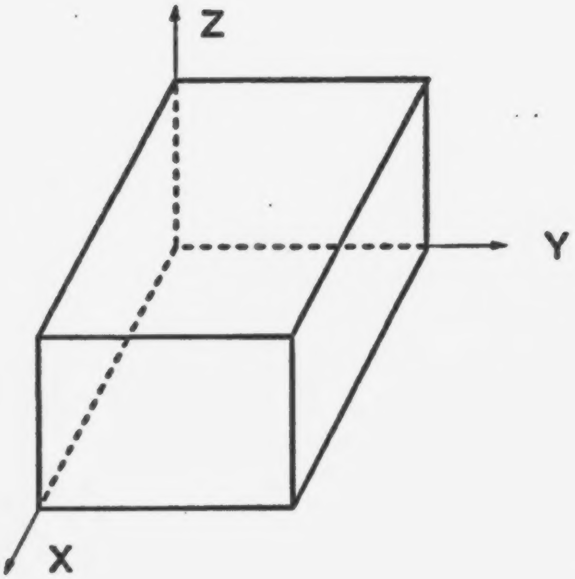

Fig. 9: A Rectangular Close-Ended Box Structure.

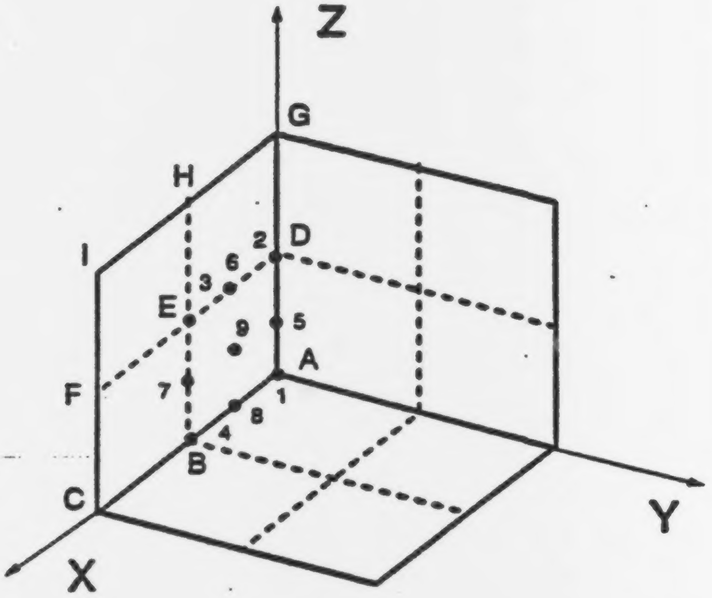
Z
G
H
I
2
D
6
3
E
5
9
A
F
7
1
8
4
B
C
Y
X

Fig. 10: A Three-Plate Corner Junction in Box Structure.

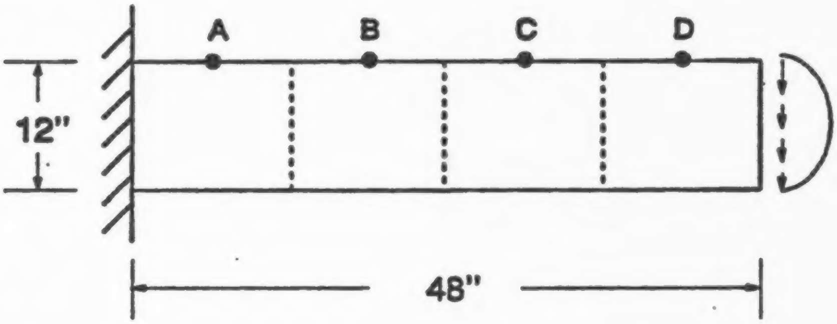

(a) Beam Configuration

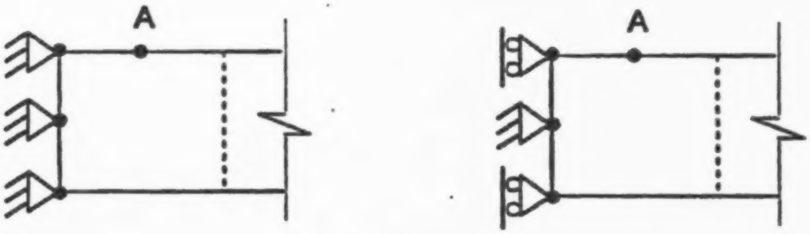

(b) Case 1

(c) Case 2

Fig. 11: Configuration and Boundary Conditions of Cantilever Beam.

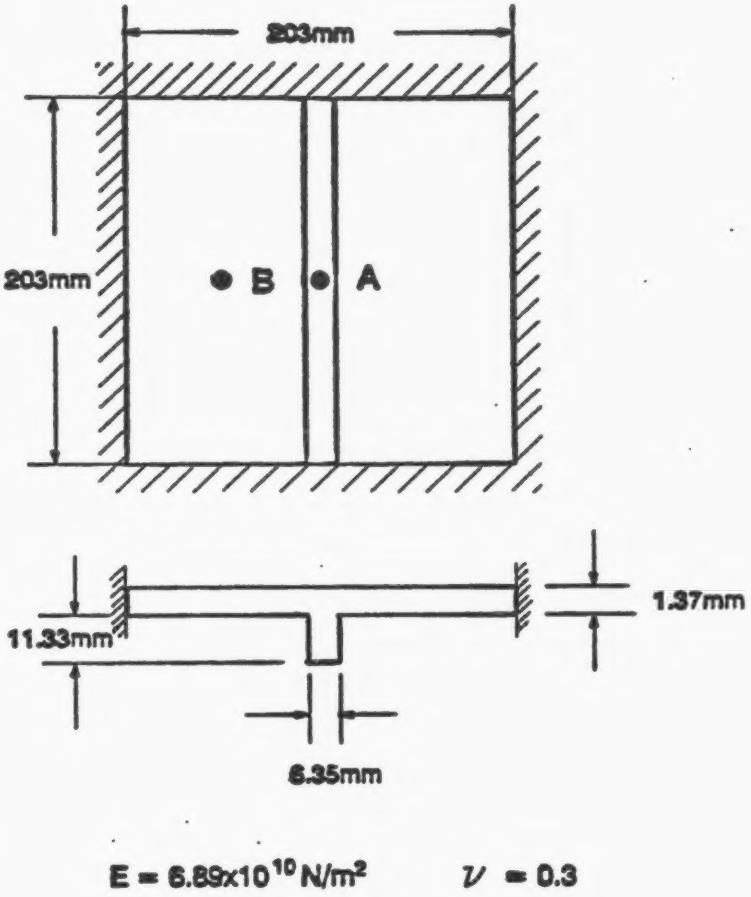
203mm
203mm
B
A
1.37mm
11.33mm
6.35mm
E = 6.89x10^{10} N/m^2
ν = 0.3

Fig. 12: Configuration of 2-Bay Stiffened Plate.

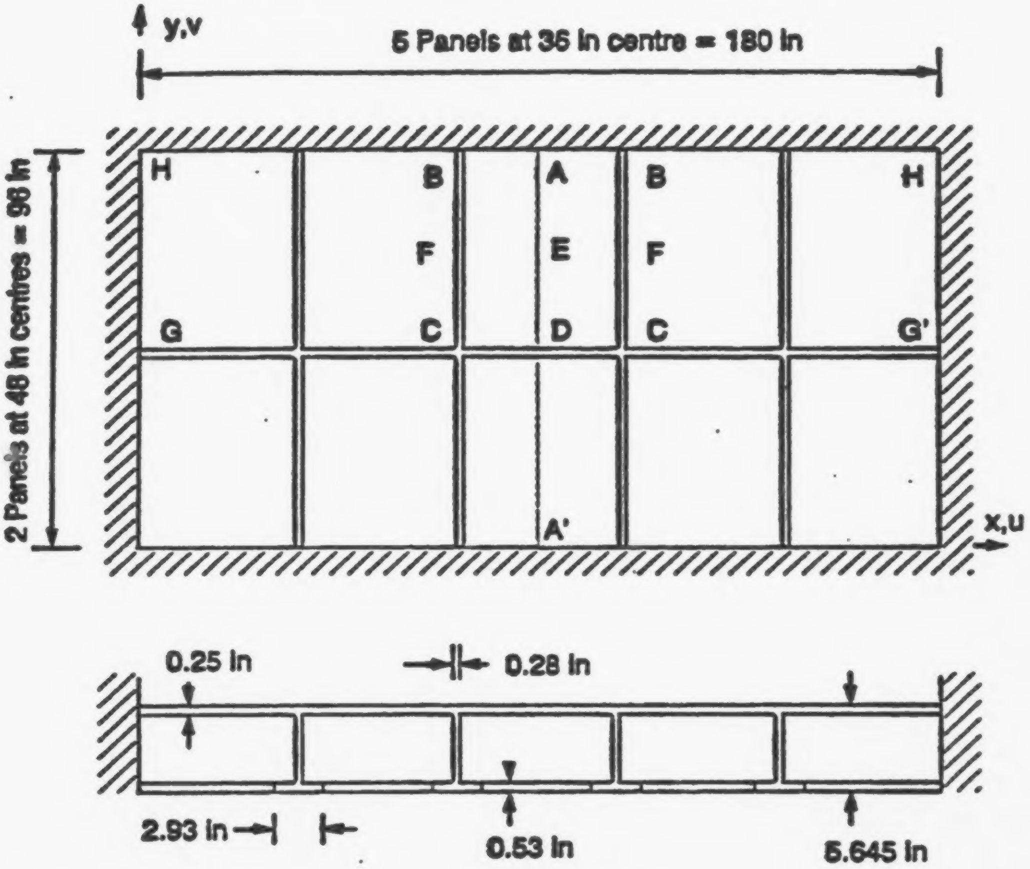
y,v
5 Panels at 36 in centre = 180 in
2 Panels at 48 in centres = 96 in
H
B
A
B
H
F
E
F
G
C
D
C
G'
A'
x,u
0.25 in
0.28 in
2.93 in
0.53 in
5.645 in

Section G-G'

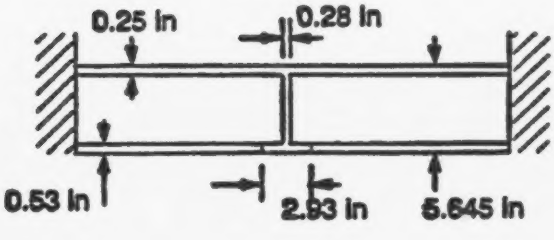
0.25 in
0.28 in
0.53 in
2.93 in
5.645 in

Section A-A'

Fig. 13: Configuration of DRES1B Panel.

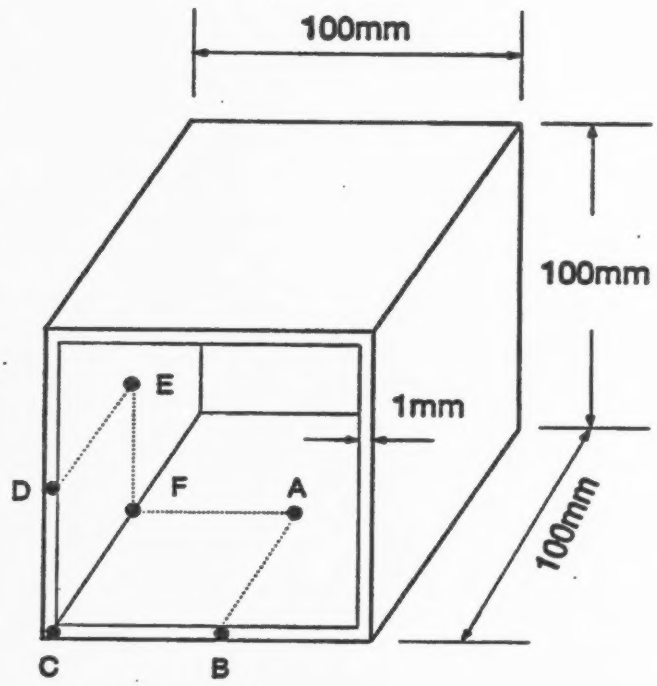
100mm
100mm
1mm
100mm
E
D
F
A
C
B

Fig. 14: Configuration of Unstiffened Cubic Tube.

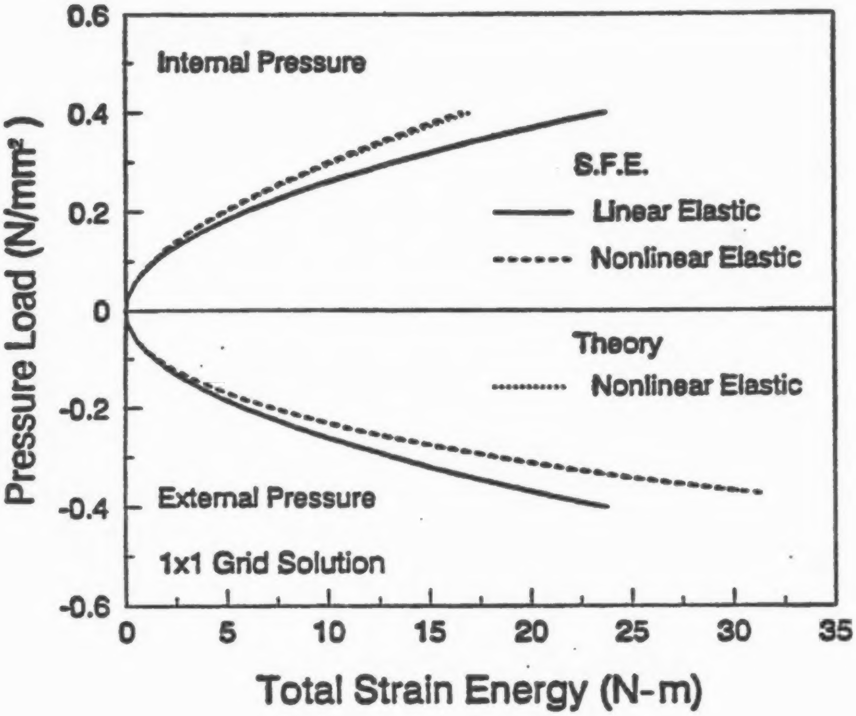

Fig. 15: Comparison of Strain Energies for Unstiffened Cubic Tube Under Internal and External Pressure Load, Respectively.

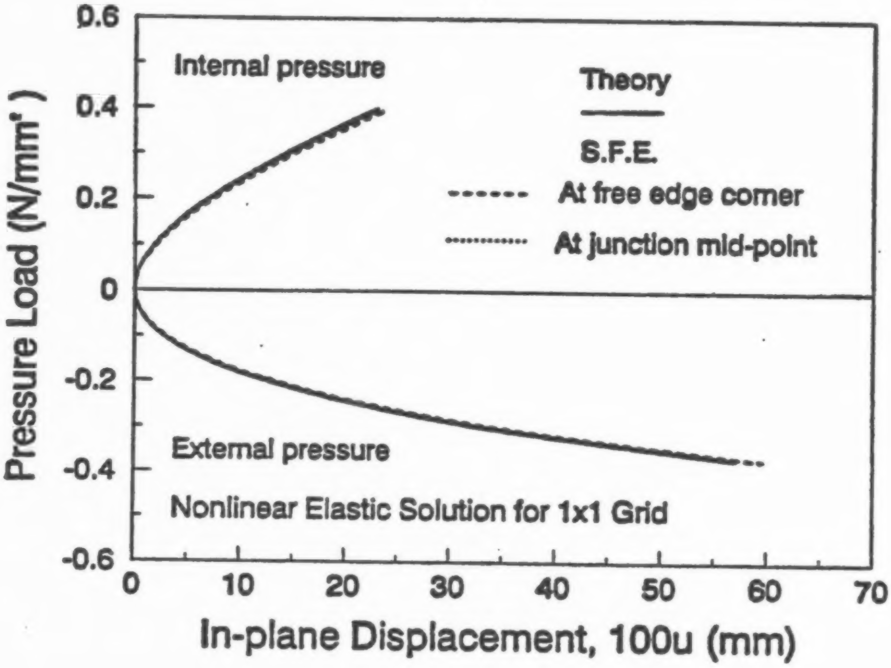

Fig. 16: Comparison of In-Plane Displacements for Unstiffened Cubic Tube Under Internal and External Pressure Load, Respectively.

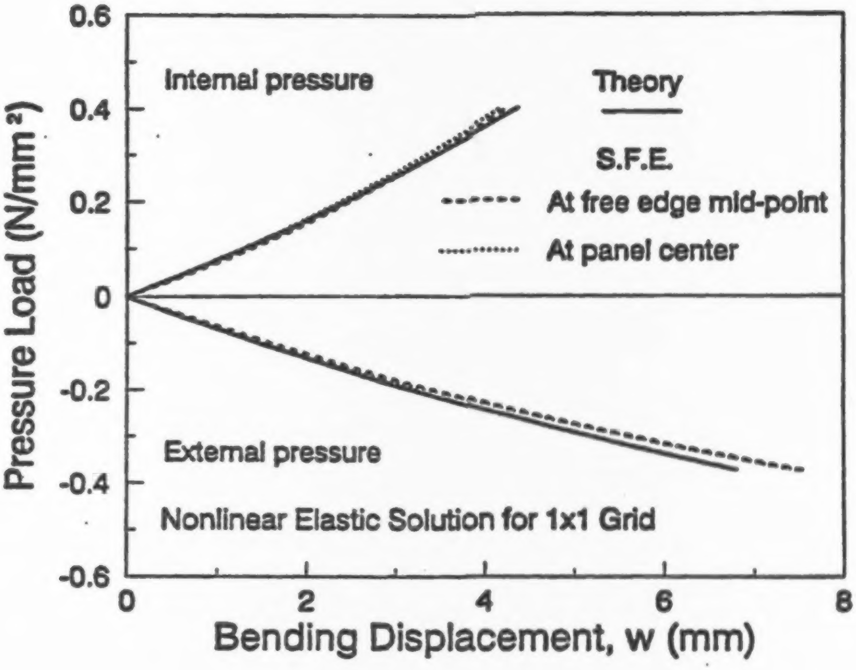

Fig. 17: Comparison of Bending Displacements for Unstiffened Cubic Tube Under Internal and External Pressure Load, Respectively.

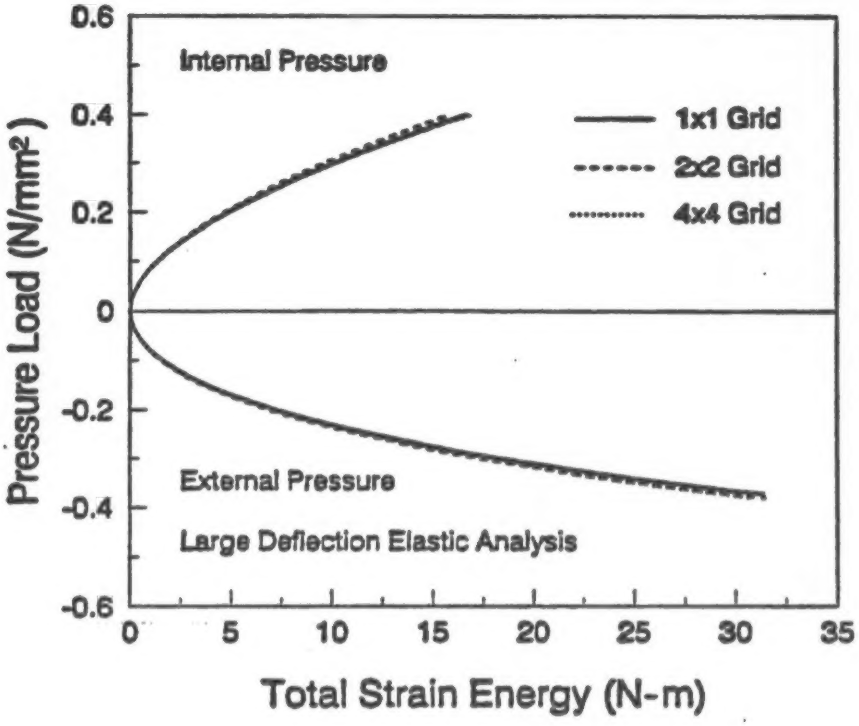

Fig. 18: Comparison of Strain Energies Obtained from Three Grid Discretizations for Unstiffened Cubic Tube.

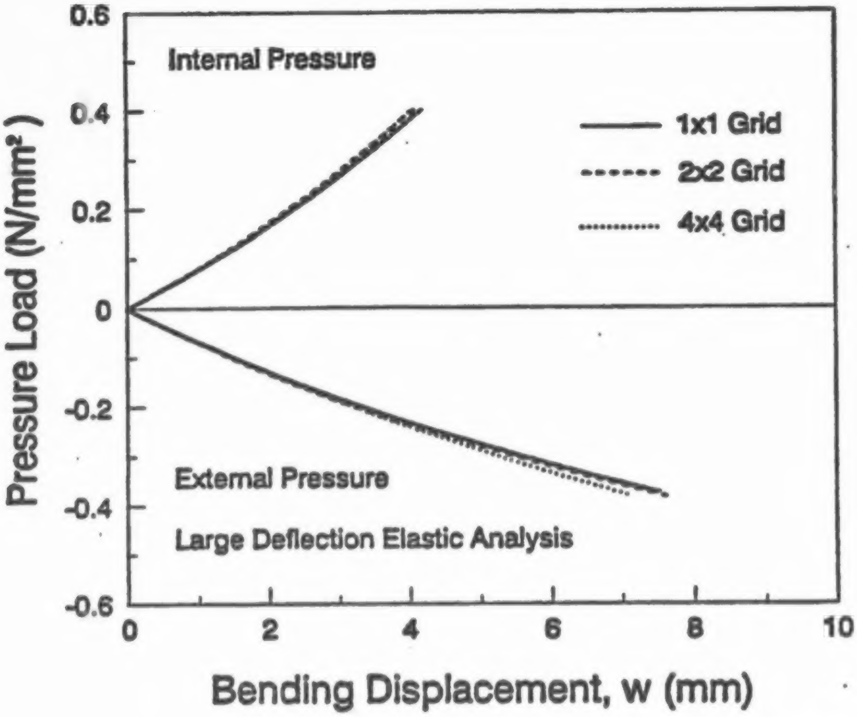

Fig. 19: Comparison of Panel Center Deflections Obtained from Three Grid Discretizations for Unstiffened Cubic Tube.

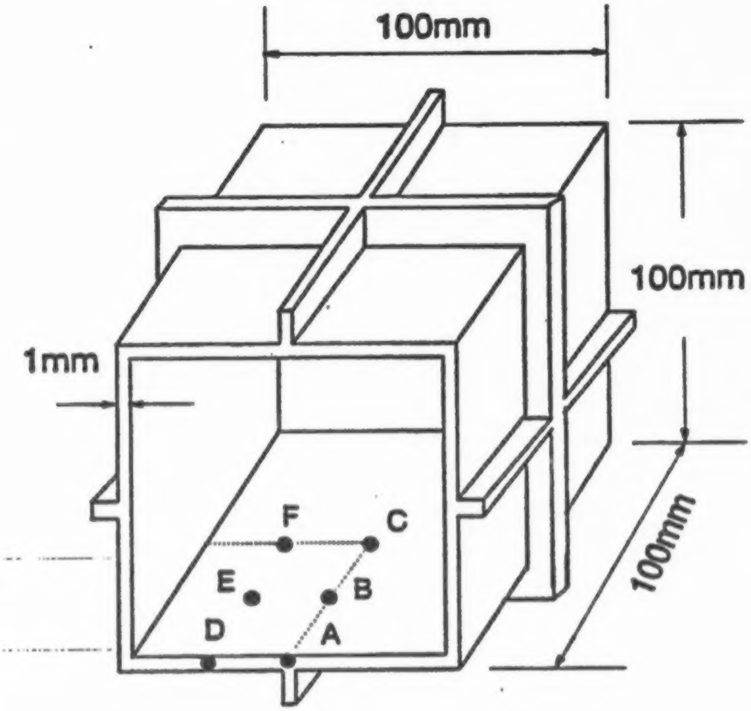
100mm
100mm
100mm
1mm
F
C
E
B
D
A

Fig. 20: Configuration of Stiffened Cubic Tube.

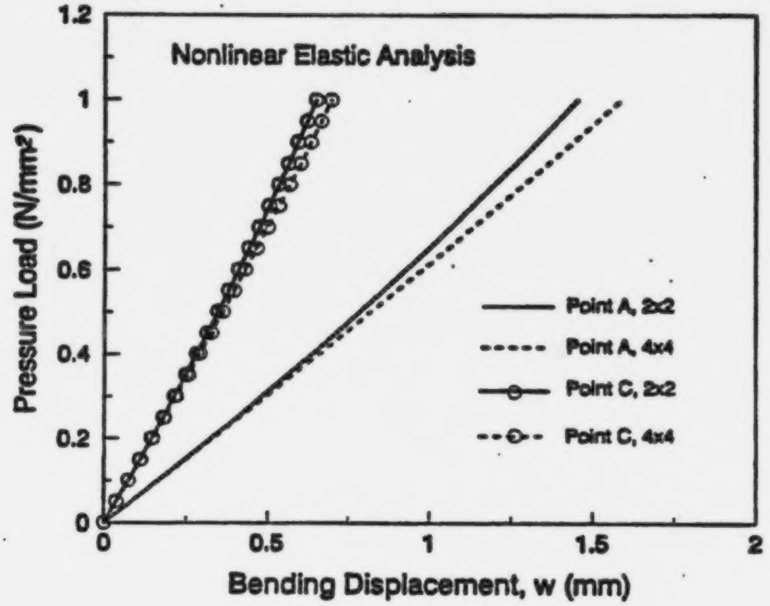

Fig. 21: Bending Displacements at Points A and C of Interior-Beam-Stiffened Cubic Tube Under Internal Pressure Load.

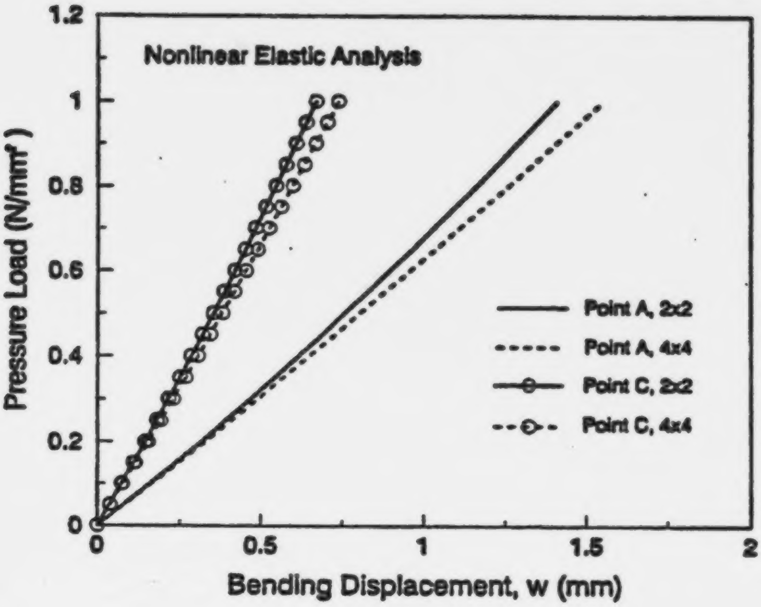

Fig. 22: Bending Displacements at Points A and C of Exterior-Beam-Stiffened Cubic Tube Under Internal Pressure Load.

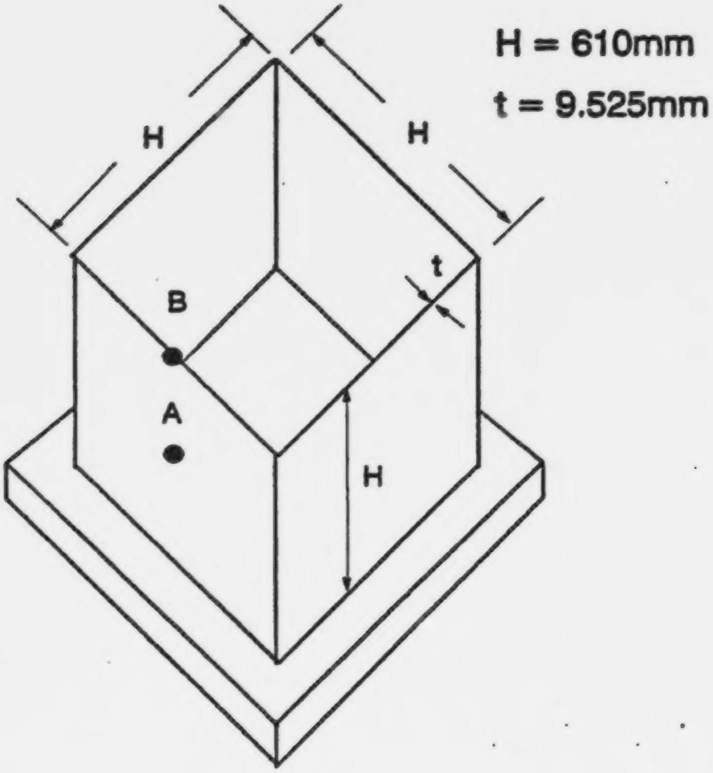
H = 610mm
t = 9.525mm
H
H
t
B
A
H

Fig. 23: Configuration of Cubic Container.

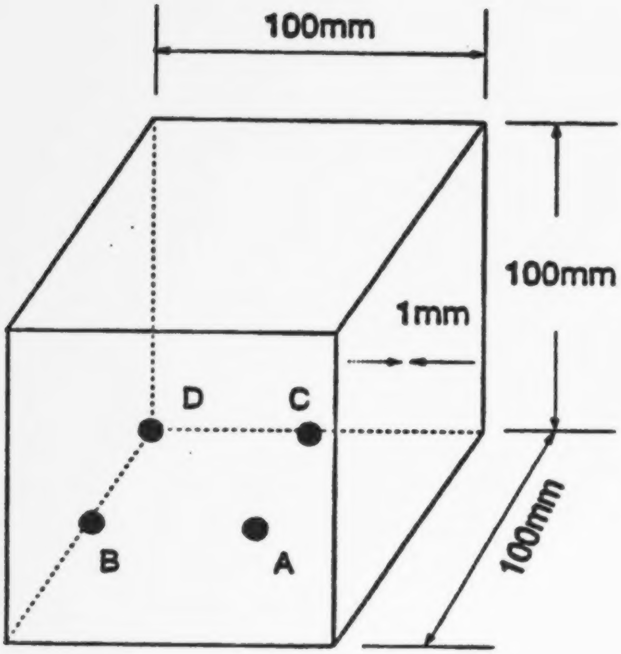
100mm
100mm
1mm
D
C
B
A
100mm

Fig. 24: Configuration of Unstiffened Cubic Box.

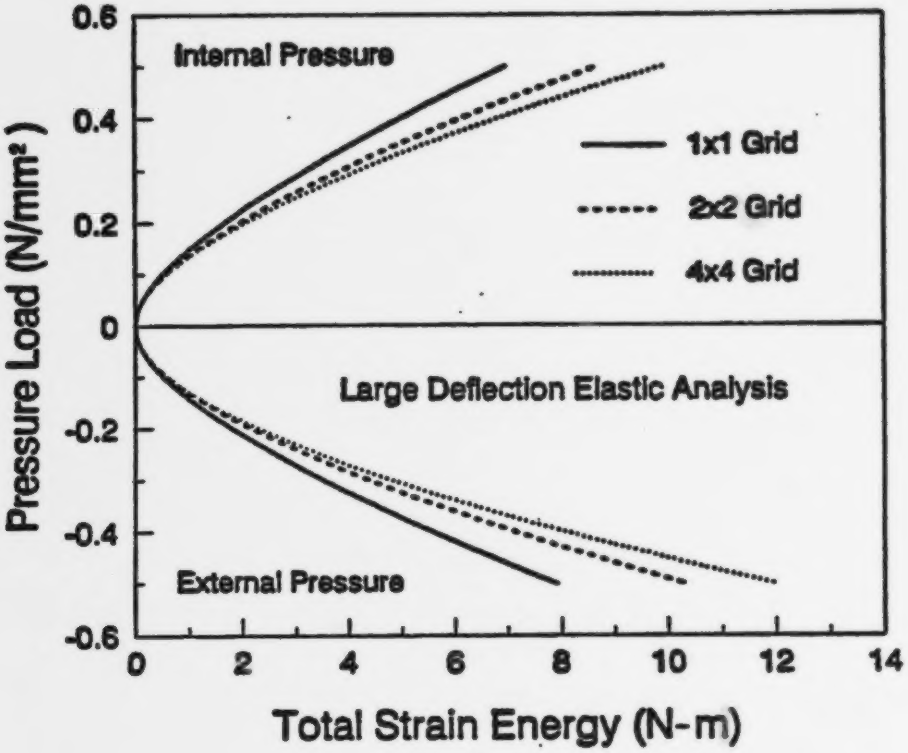

Fig. 25: Comparison of Strain Energies Obtained from Three Grid Discretizations for Unstiffened Cubic Box Under Internal and External Pressure Load, Respectively.

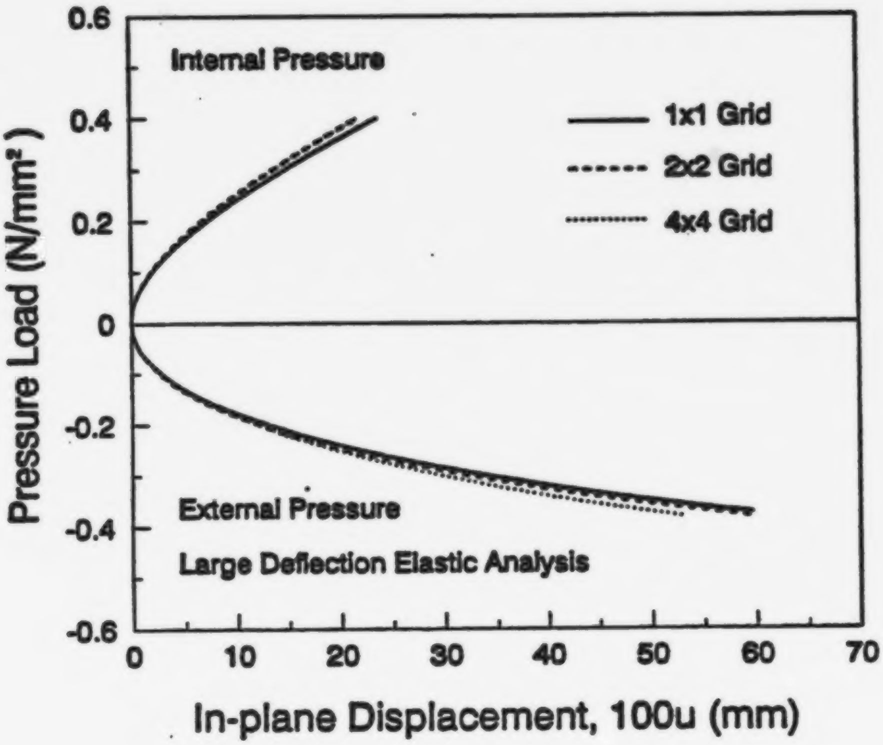

Fig. 26: Comparison of In-Plane Displacements at Junction Mid-Point Obtained from Three Grid Discretizations for Unstiffened Cubic Box Under Internal and External Pressure Load, Respectively.

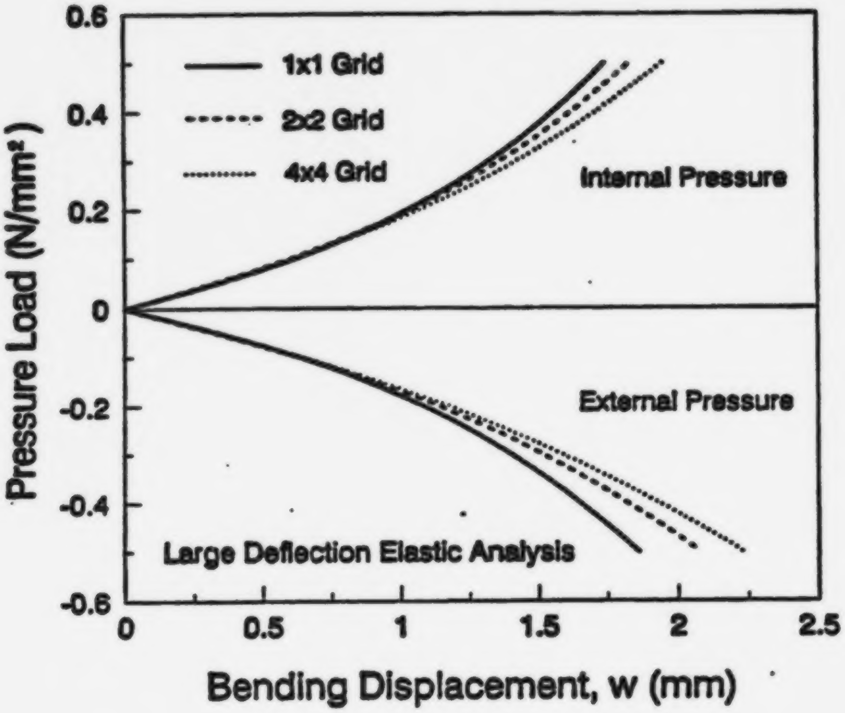

Fig. 27: Comparison of Panel Center Deflections Obtained from Three Grid Discretizations for Unstiffened Cubic Box Under Internal and External Pressure Load, Respectively.

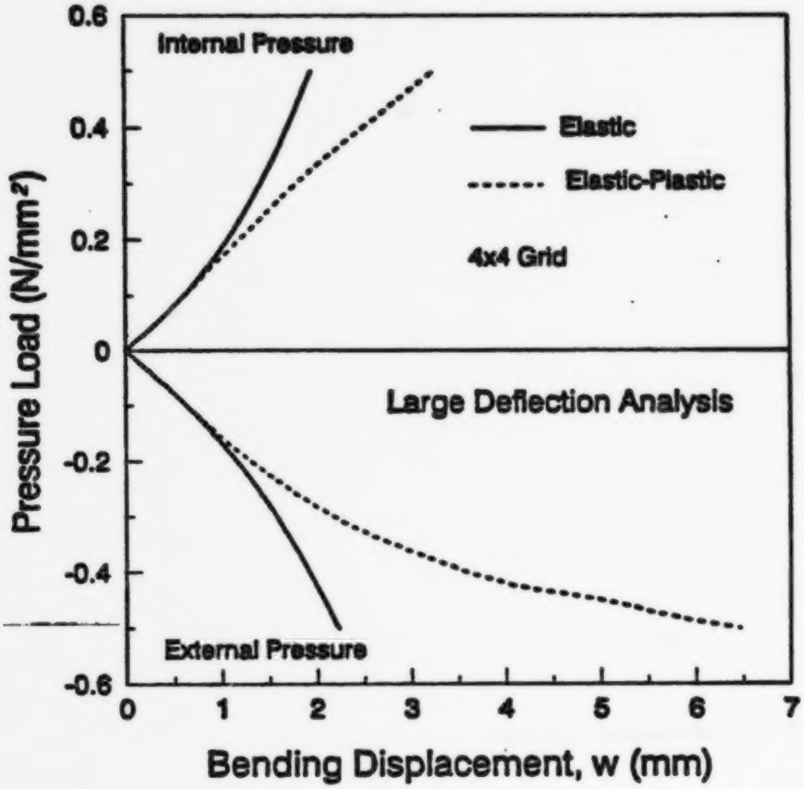

Fig. 28: Nonlinear Panel Center Displacements for Unstiffened Cubic Box Under Internal and External Pressure Load, Respectively.

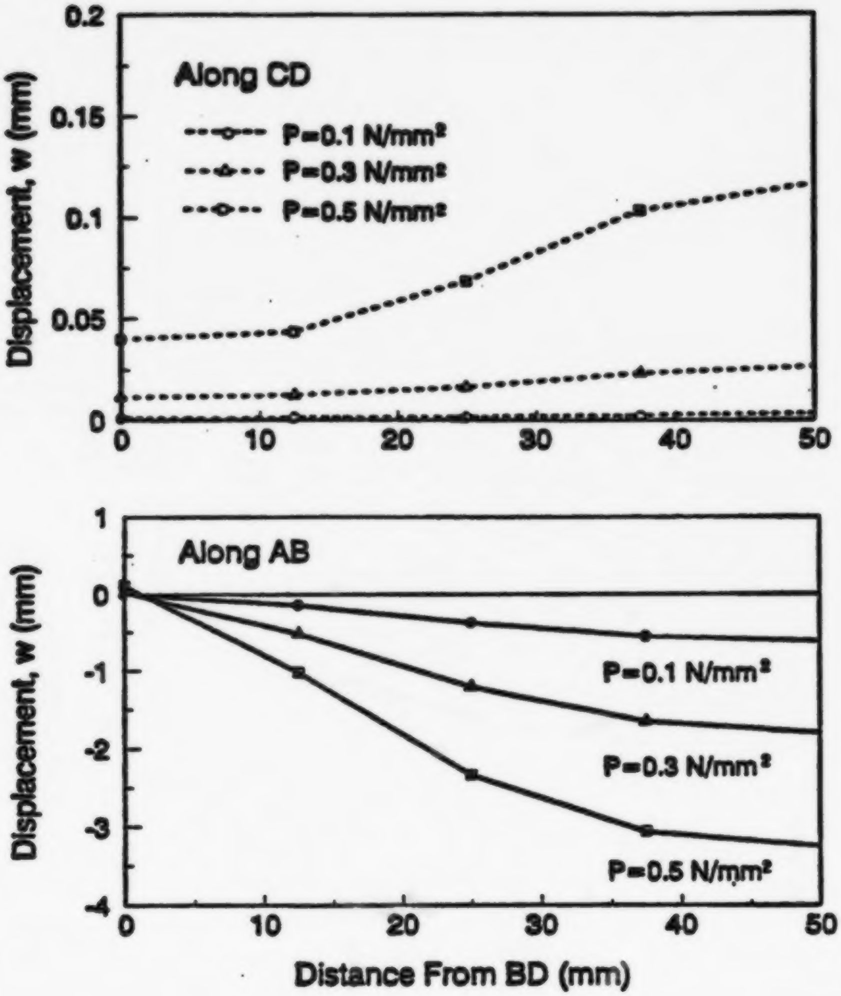

Fig. 29: Large Deflection, Elastic-Plastic Displacement Profiles in Unstiffened Cubic Tube Due to Internal Pressure Load.

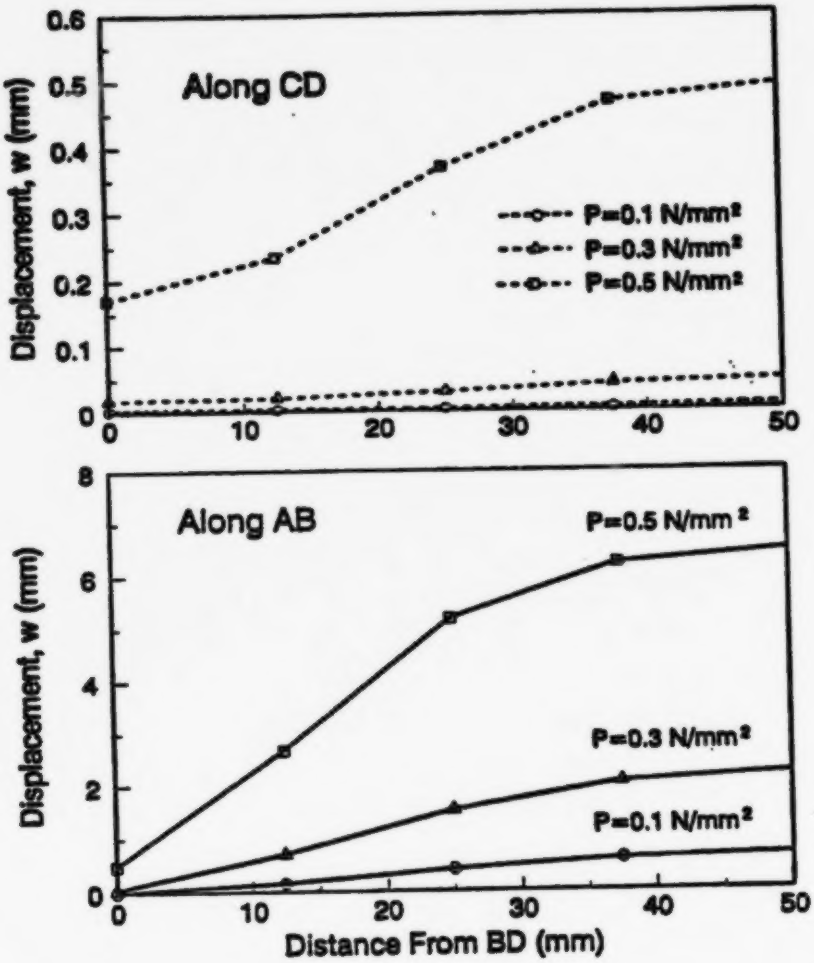

Fig. 30: Large Deflection, Elastic-Plastic Displacement Profiles in Unstiffened Cubic Tube Due to External Pressure Load.

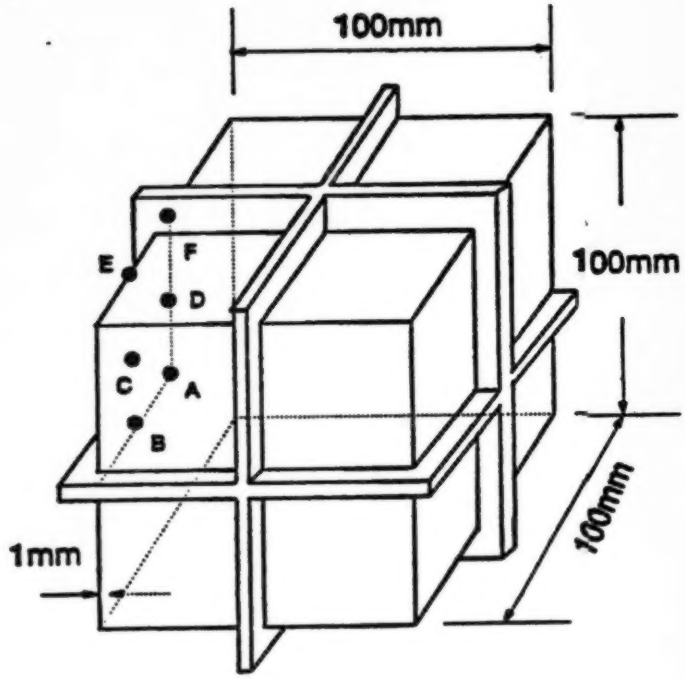
100mm
100mm
100mm
1mm
E
F
D
C
A
B

Fig. 31: Configuration of Stiffened Cubic Box.

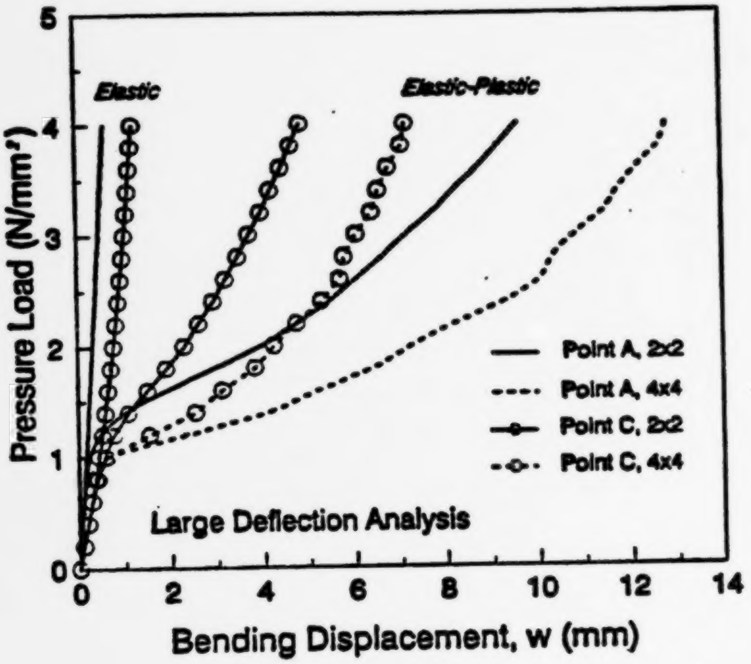

Fig. 32: Bending Displacements at Points A and C in Interior-Beam-Stiffened Cubic Box Due to Internal Pressure Load.

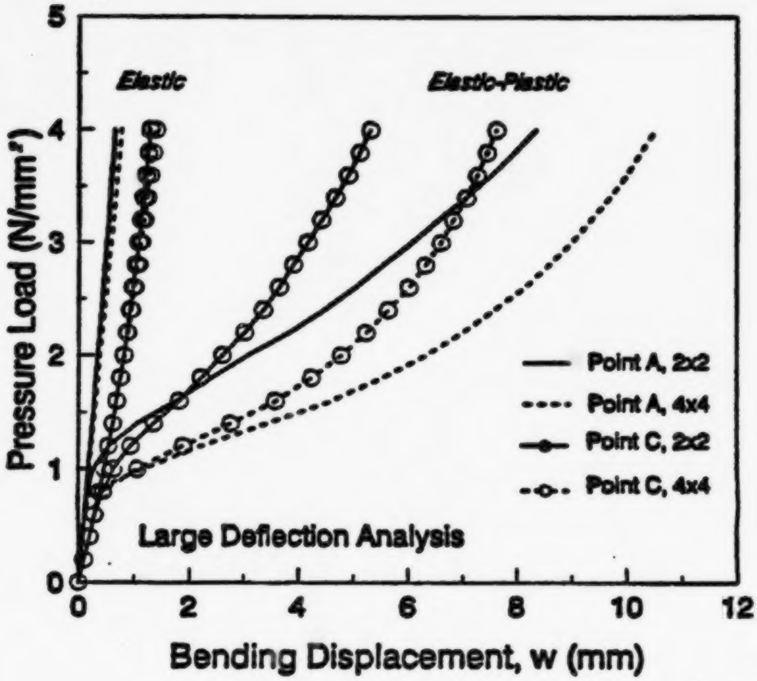

Fig. 33: Bending Displacements at Points A and C in Exterior-Beam-Stiffened Cubic Box Due to Internal Pressure Load.

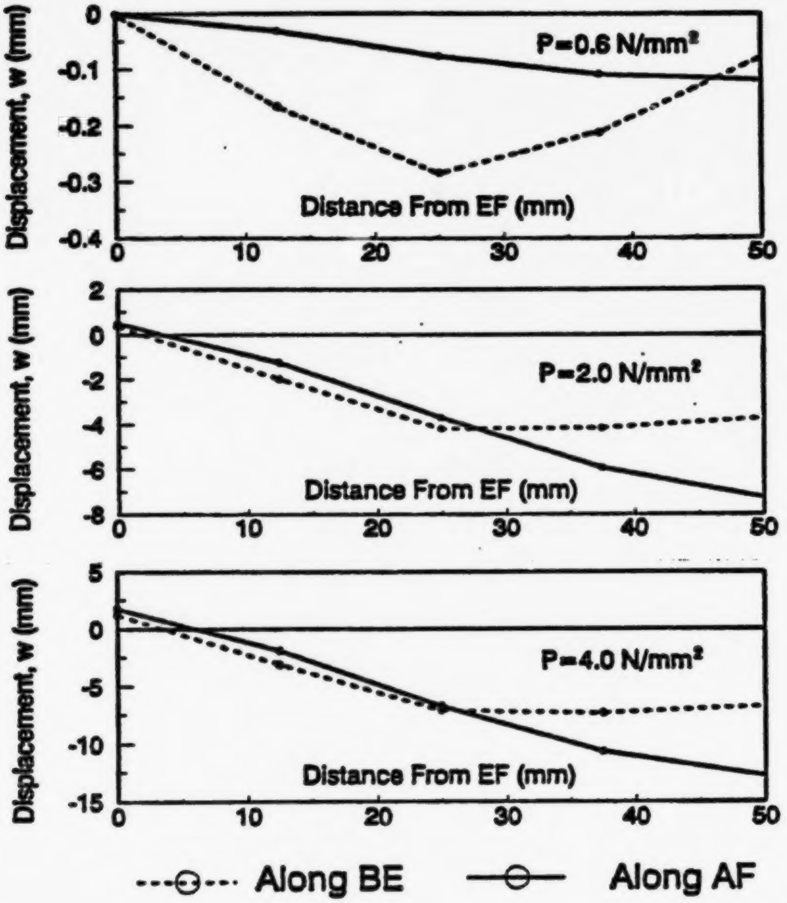

Fig. 34: Large Deflection, Elastic-Plastic Displacement Profiles in Interior-Beam-Stiffened Cubic Box Due to Internal Pressure Load.

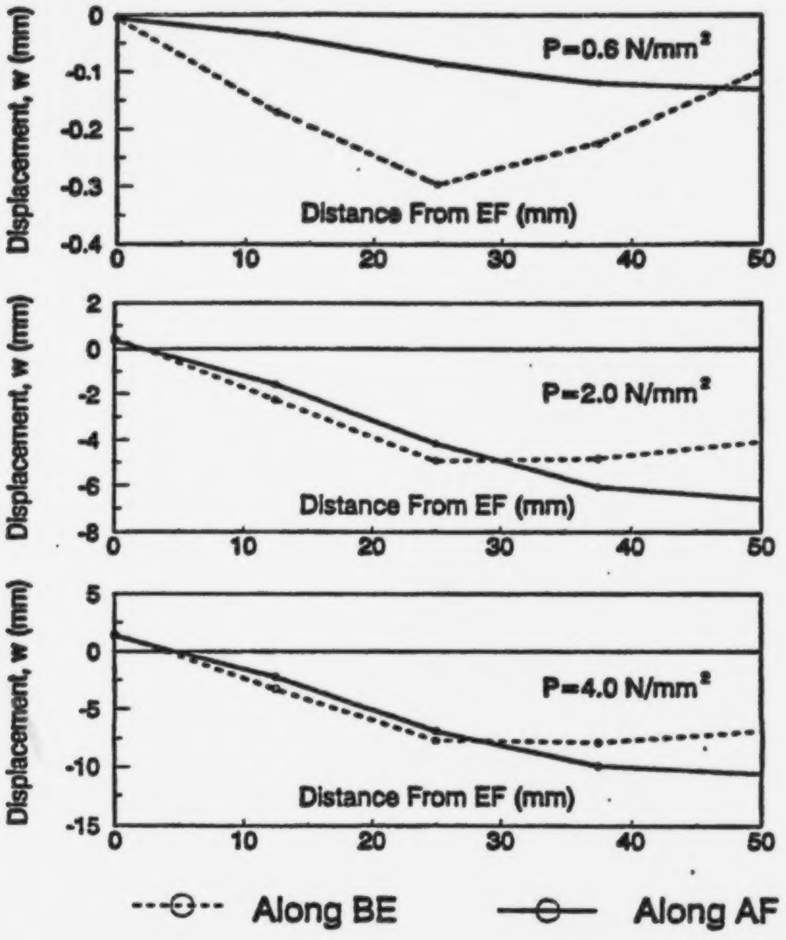

Fig. 35: Large Deflection, Elastic-Plastic Displacement Profiles in Exterior-Beam-Stiffened Cubic Box Due to Internal Pressure Load.

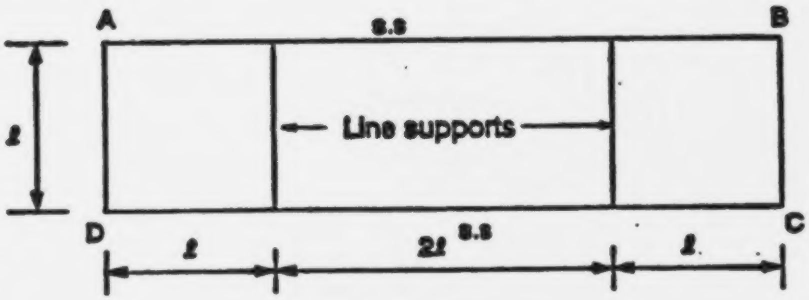
A
B
C
D
S.S
S.S
Line supports
ℓ
ℓ
2ℓ
ℓ

Fig. 36: Configuration of 3-Bay Continuous Plate.

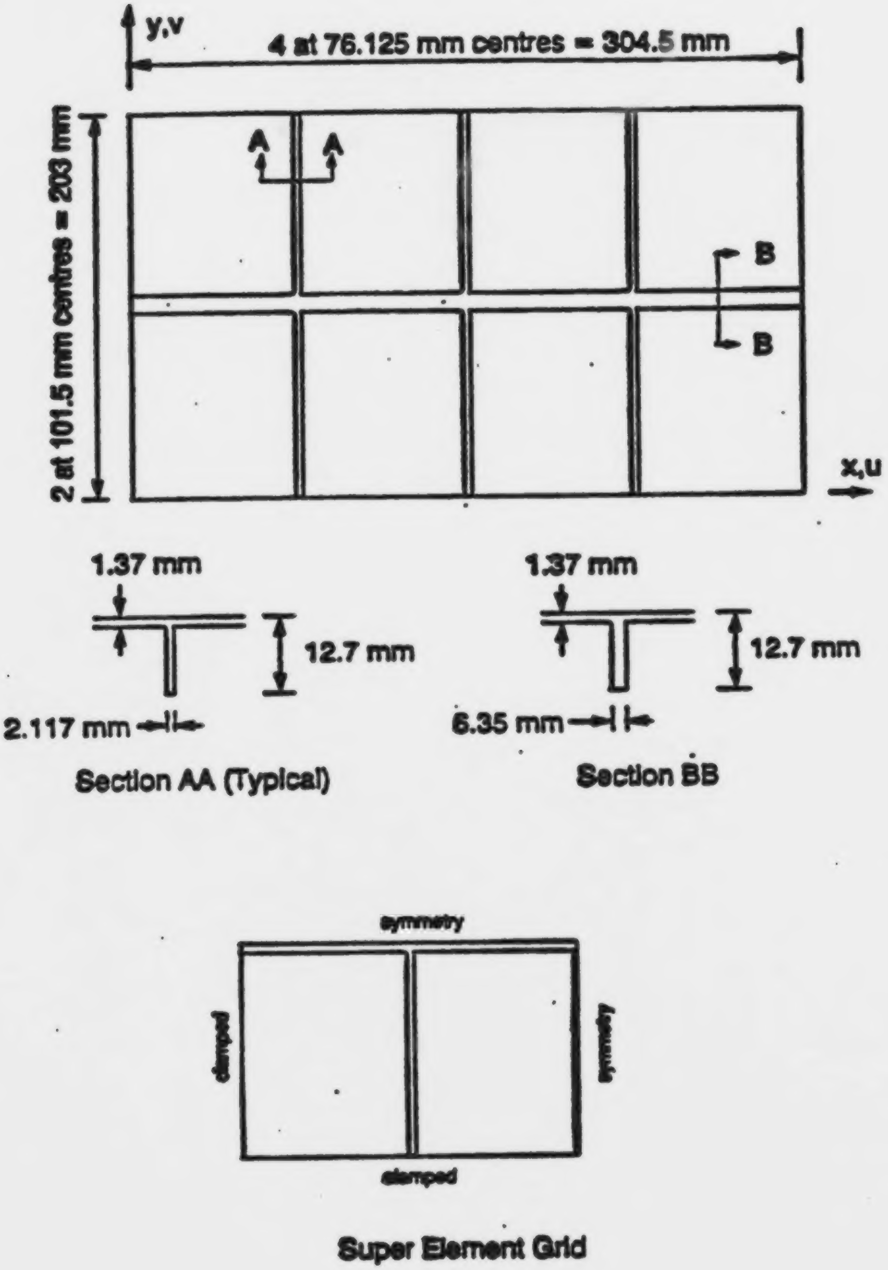
y,v
4 at 76.125 mm centres = 304.5 mm
2 at 101.5 mm centres = 203 mm
A
A
B
B
x,u
1.37 mm
12.7 mm
2.117 mm
Section AA (Typical)
1.37 mm
12.7 mm
6.35 mm
Section BB
symmetry
clamped
symmetry
clamped
Super Element Grid

Fig. 37: Configuration and Discretization of 2x4 Bay Stiffened Plate.

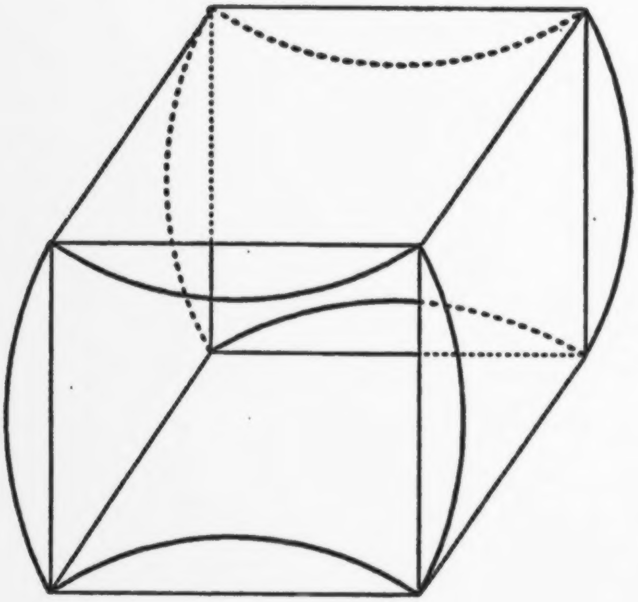

Fig. 38: Fundamental Mode Shape for Unstiffened Cubic Tube.

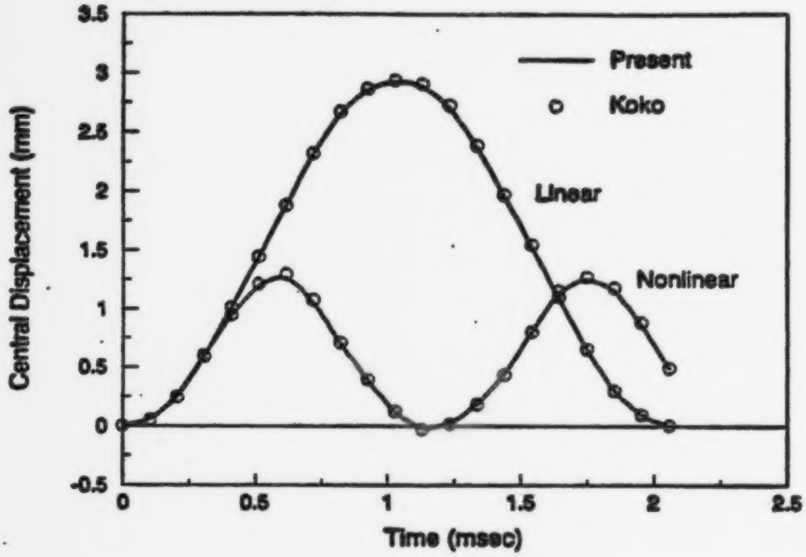

Fig. 39: Transient Elastic Response of Simply Supported Square Plate Under Step Load.

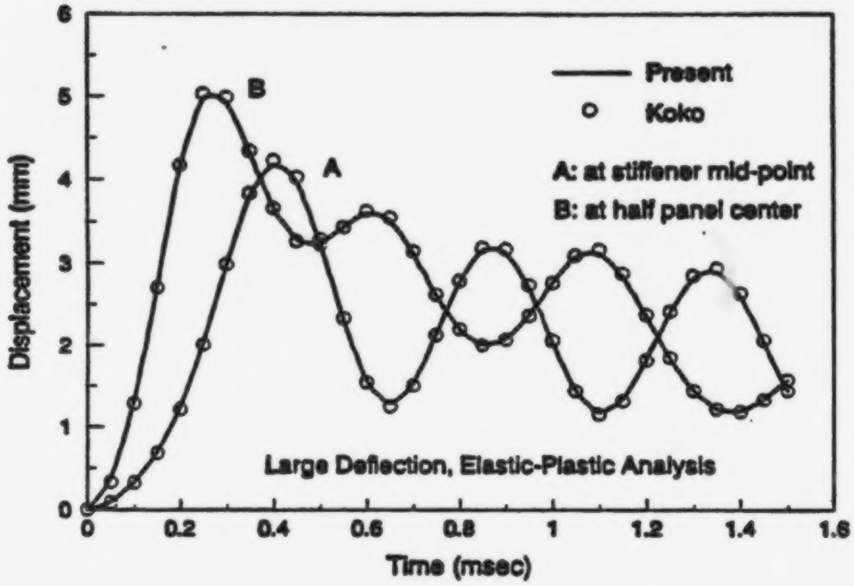

Fig. 40: Nonlinear Transient Elastic-Plastic Response of Clamped 2-Bay Stiffened Plate Under Blast Load.

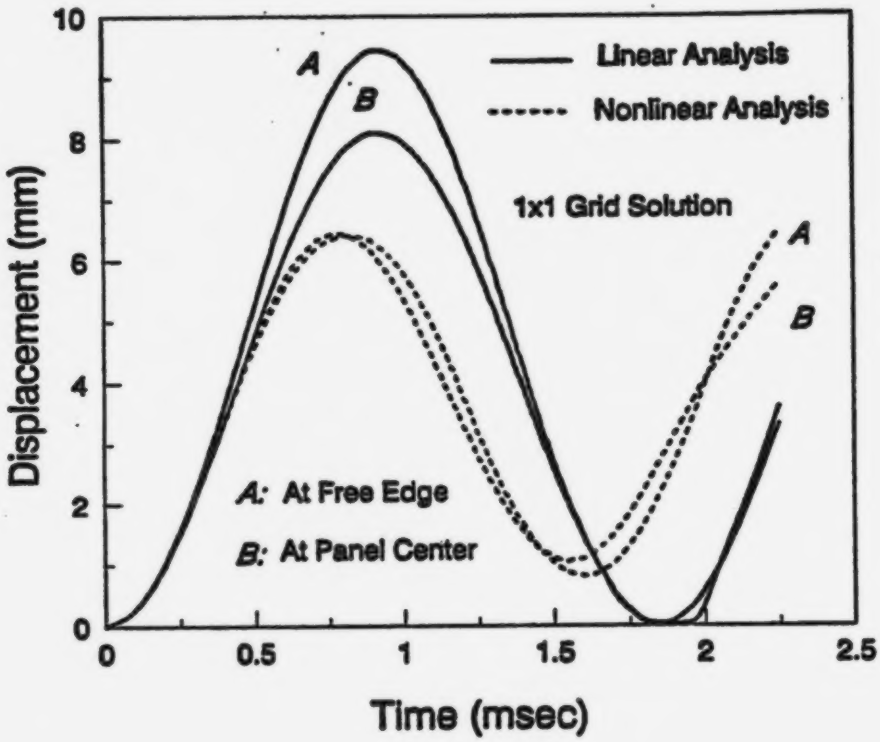

Fig. 41: Transient Elastic Response of Unstiffened Cubic Tube Under Step Internal Pressure Load.

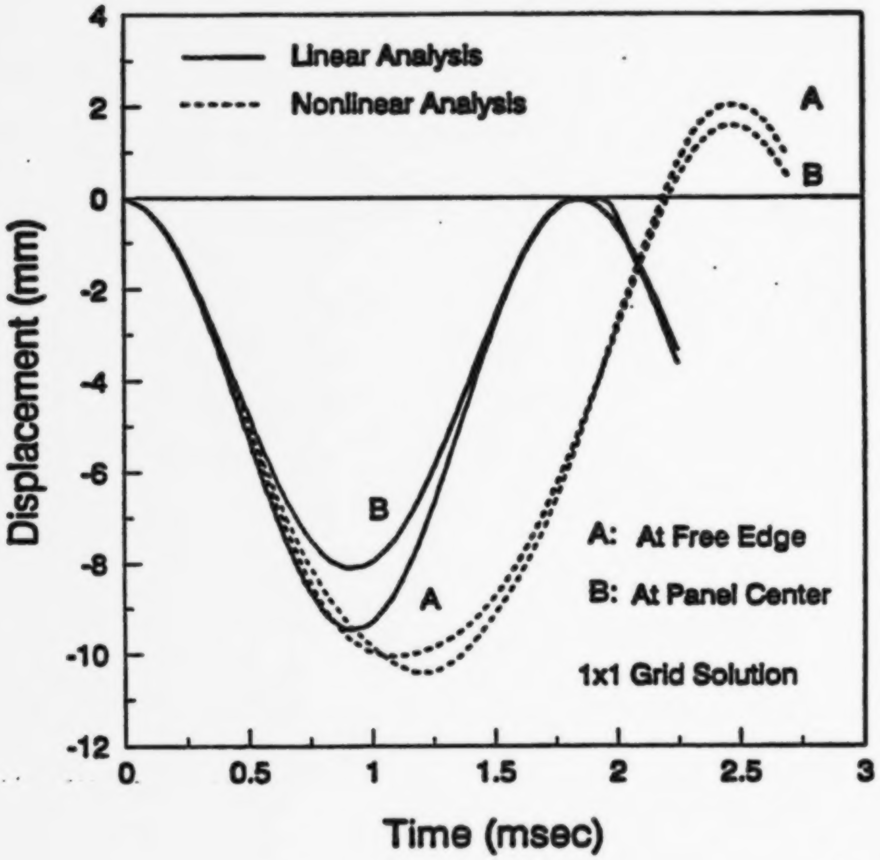

Fig. 42: Transient Elastic Response of Unstiffened Cubic Tube Under Step External Pressure Load.

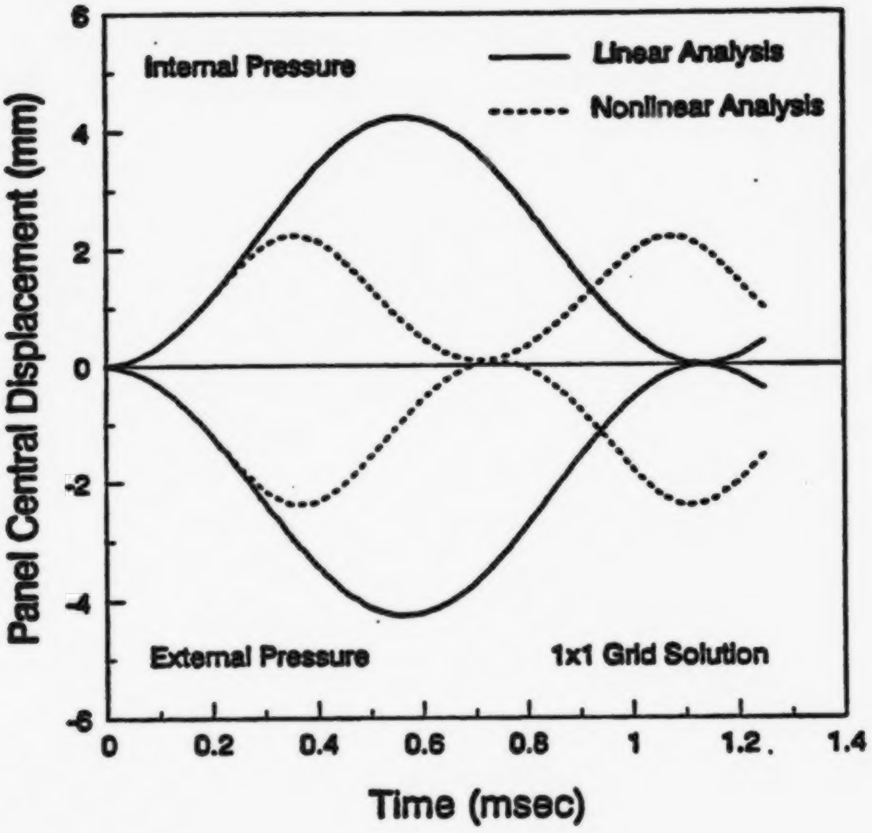

Fig. 43: Transient Elastic Response of Unstiffened Cubic Box Under Step Pressure Loads.

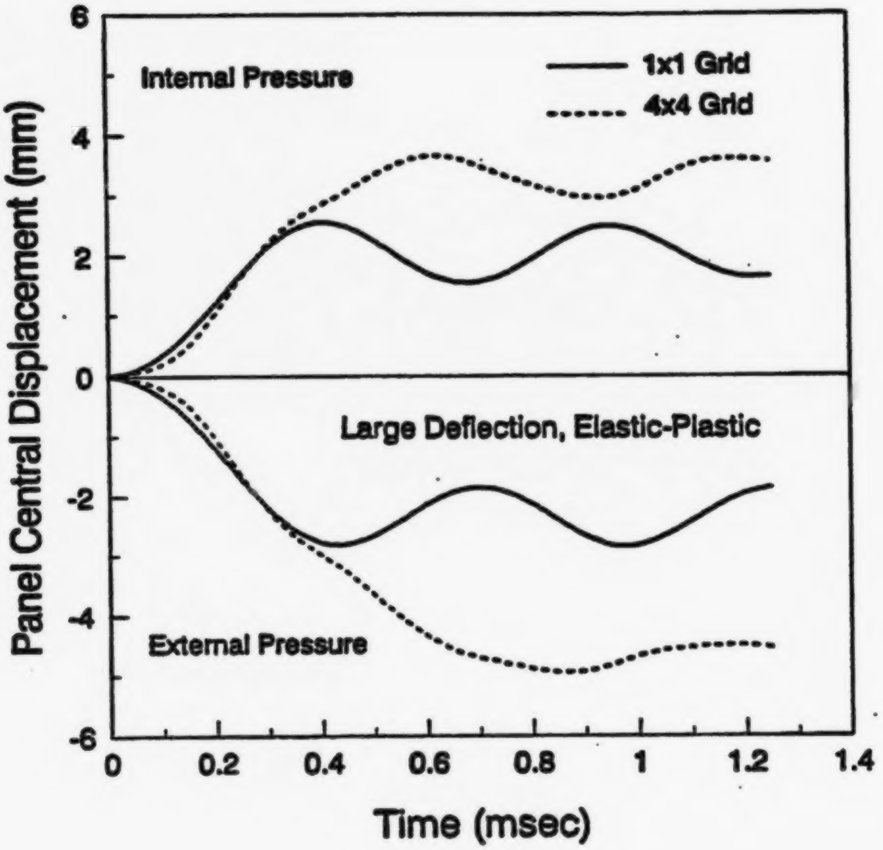

Fig. 44: Nonlinear Transient Elastic-Plastic Response of Unstiffened Cubic Box Under Step Pressure Loads.

Research Reports
Department of Civil Engineering
University of British Columbia

STRUCTURAL RESEARCH SERIES

Report No. 1: "Determination of the Dynamic Properties of a Tower Structure from Ambient Vibrations", S. Cherry and U.A. Topf, September 1970.

Report No. 2: "A Consistent Finite Element Method for Random Response Problems", Mervyn D. Olson, December 1970.

Report No. 3: "Duration of Load Tests for Dry Lumber in Bending", Borg Madsen, October 1971.

Report No. 4: "Duration of Load Tests for Wet Lumber in Bending", Borg Madsen, March 1972.

Report No. 5: "A Variational Finite Element Method for Two-Dimensional Steady Viscous Flows:, Mervyn D. Olson, March 1972.

Report No. 6: "Duration of Load Tests for Dry Lumber Subjected to Shear", Borg Madsen, October 1972.

Report No. 7: "Duration of Load Tests for Wood in Tension Perpendicular to Grain", Borg Madsen, November 1972.

Report No. 8: "An Engineering Approach to Estimating the 5th Percentile Levels for Structural Properties of Wood", Borg Madsen, November 1972.

Report No. 9: "Slow Crack Growth in Wood", Sidney Mindess, December 1974.

Report No. 10: "Structural Wood and 'Limit States Design'", Borg Madsen, January 1975.

Report No. 11: "Moisture Content - Strength Relationship for Lumber Subjected to Bending", Borg Madsen, February 1975.

Report No. 12: "Time-Strength Relationship for Constantly Loaded 2 x 6 Douglas fir Joists", Borg Madsen, February 1975.

Report No. 13: "Time-Strength Relationship for Lumber", Borg Madsen and J.D. Barrett, April 1976.

Report No. 14:	"A Study of Various Finite Element Solution Methods for the Navier-Stokes Equations", S.Y. Tuann and Mervyn D. Olson, June 1976.
Report No. 15:	"In-Grade Testing, Size Investigations on Lumber Subjected to Bending", Borg Madsen and Peter C. Nielsen, October 1976.
Report No. 16:	"Numerical Studies of Flow Over a Circular Cylinder by a Finite Element Method", S.Y. Tuann and Mervyn D. Olson, December 1976.
Report No. 17:	"In-Grade Testing, Degree of Damage Due to Proof Loading of Lumber in Bending", Borg Madsen, October 1976.
Report No. 18:	"In-Grade testing, Problem Analysis", Borg Madsen, January 1977.
Report No. 19:	"Studies of Rectangular Cavity Flow with Reynolds Number by a Finite Element Method", S.Y. Tuann and Mervyn D. Olson, June 1977.
Report No. 20:	"Behaviour of Headed Stud Connections for Precast Concrete Panels under Momotonic and Cycled Shear Loading", Donald S. Neille, October 1977.
Report No. 21:	"In-Grade Testing, Accuracy and Confidence, Computer Simulations", Borg Madsen and Peter C. Nielsen, February 1978.
Report No. 22:	"Comparison Problem No. 1, Recirculating Flow in a Square Cavity", Mervyn D. Olson, May 1979.
Report No. 23:	"In-Grade Testing, Investigation of Test Parameters in Longitudinal Shear", Borg Madsen and Peter C. Nielsen, March 1978.
Report No. 24:	"In-Grade Testing, Investigation of Test Parameters in Parallel-to-Grain Tension", Borg Madsen and Peter C. Nielsen, March 1978, Revised June 1981.
Report No. 25:	"In-Grade Testing, Stiffness Adjustments", Borg Madsen and Peter C. Nielsen, August 1978, Revised June 1981.
Report No. 26:	"In-Grade Testing, Investigation of Test Parameters in Parallel-to-Grain Compression", Borg Madsen and Peter C. Nielsen, August 1979, Revised June 1981.

Report No. 27: "Moisture Effects in Lumber", Borg Madsen, Walter Janzen and Joe Zwaagstra, January 1980.

Report No. 28: "Measurements of Displacement and Strains in Axially Loaded Wooden Specimens by Laser Holography", J. Brdicko, M.D. Olson and B. Madsen, July 1980.

Report No. 29: "A Design Method for Perpendicular to Grain Loads in Wood", Borg Madsen, R.F. Hooley, C.P. Hall, July 1981.

Report No. 30: "Air-Blast Response of Beams and Plates", J. Ari-Gur, D.L. Anderson and M.D. Olson, June 1983.

Report No. 31: "A Report on Experiments on Duration of Load Effects for Wood Subject to Constant Shear Strees", R. Spencer, December 1983.

Report No. 32: "Finite Deflection Dynamic Analysis of Rigid-Plastic Beams", R. Vaziri, May 1985.

Report No. 33: "Large Deflection, Elastic-Plastic Dynamic Response of Air-Blast Loaded Plate Structures by the Finite Strip Method", M.R. Khalil, M.D. Olson and D.L. Anderson, March 1987.

Report No. 34: "Reliability - Based Design of Wood Structures", R.O. Foschi, B.R. Folz, and F.Z. Yao, October 1989.

Report No. 35: "Nonlinear Transient Analysis of Cylindrical Shell Structures by the Finite Strip Method", J. Jiang, M.D. Olson and D.L. Anderson, June 1990.

Report No. 36: "Nonlinear Static and Dynamic Analysis of Stiffened Box Structures Using Super Finite Elements", J. Jiang and M.D. Olson, June 1991.

#105375
92-02508

Defence Research and Development Canada
Recherche et développement pour la défense Canada
Canada

Français Contact Us Help Search Canada Site
Home Defence R&D Canada Defence Site

Browse Indexes

Titles

Authors

Descriptors

Corporate Authors

Corporate Acronyms

Document Numbers

Search Database

Summary

It is recommended you search "Authors" and "Corporate Authors" on their respective "Browse" pages.

Click here if you are having problems displaying text (ie. text is too big, or too small) or page appears to be jumbled.

Top Previous **Document:** 3 of 7 Next Bottom Order Download

TITLE: DEVELOPMENT OF METHODS FOR MODELLING STRUCTURAL RESPONSE AND PREDICTING FAILURE OF STRUCTURES SUBJECTED TO **BLAST LOADING** - PHASE V
PERSONAL AUTHOR: Olson, M.D.
CORPORATE AUTHOR: Defence Research Establishment Suffield, Ralston ALTA (CAN);British Columbia Univ, Vancouver BC (CAN) Dept of Civil Engineering

ABSTRACT: (No abstract)
DESCRIPTORS: Models;Structural members;Blasting;Failure;Performance;Tables (data);Blast loads;Computer programs

REPORT NUMBER: DRES-CR-27-92; Contract Report (Final); See also DSIS 92-02509	**REPORT DATE:** 15 Dec 1991	**NUMBER OF PAGES** : 222
DRDKIM N^o: 92-02508	**CANDIS N^o:** 105375	**Format(s):**Hardcopy;Originator's fiche received by DSIS;Document Image stored on Optical Disk

Date modified: 2005-04-05 Important Notices